Department of Radio Science and Engineering

Multitemporal InSAR in land-cover and vegetation mapping

Marcus Engdahl

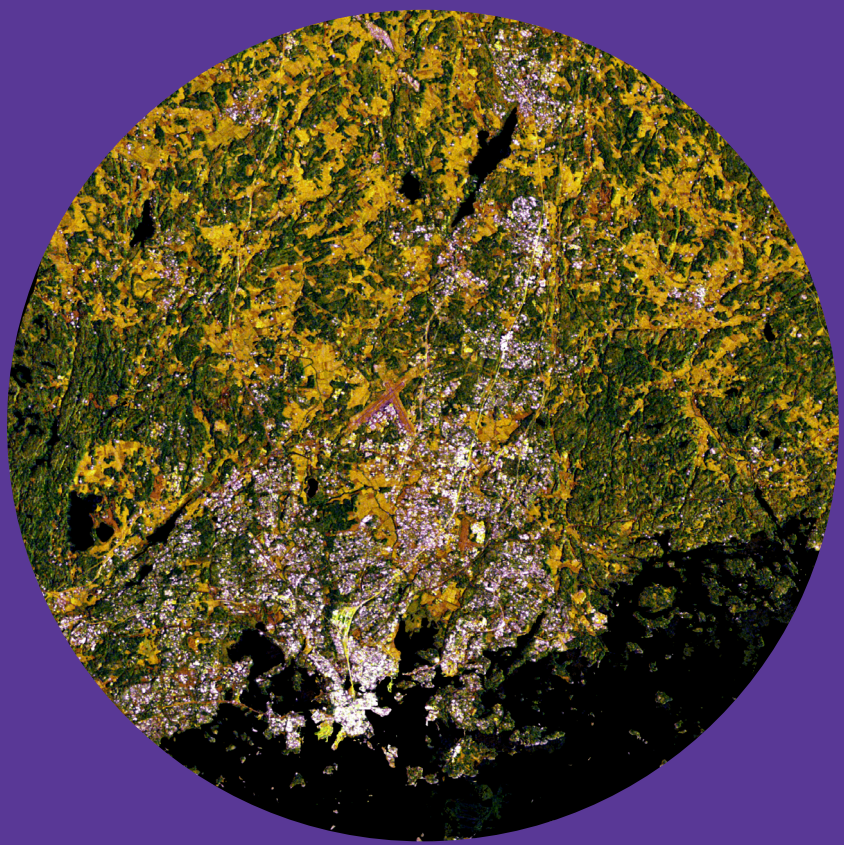

Aalto University

DOCTORAL DISSERTATIONS

Aalto University publication series
DOCTORAL DISSERTATIONS 178/2013

Multitemporal InSAR in land-cover and vegetation mapping

Marcus Engdahl

A doctoral dissertation completed for the degree of Doctor of Science (Technology) to be defended, with the permission of the Aalto University School of Electrical Engineering, at a public examination held at the lecture hall S1 of the school on 15 November 2013 at 12.

Aalto University
School of Electrical Engineering
Department of Radio Science and Engineering
Space Technology

Supervising professor
Prof. Martti Hallikainen

Preliminary examiners
Dr. Josef Kellndorfer
Dr. Yrjö Rauste

Opponent
Prof. Iain H. Woodhouse, The University of Edinburgh, United Kingdom

Aalto University publication series
DOCTORAL DISSERTATIONS 178/2013

ISBN 978-952-60-5415-5
ISBN 978-952-60-5416-2 (pdf)
ISSN-L 1799-4934
ISSN 1799-4934 (printed)
ISSN 1799-4942 (pdf)
http://urn.fi/URN:ISBN:978-952-60-5416-2

Unigrafia Oy
Helsinki 2013

Finland

441 697
Printed matter

Aalto University

Abstract

Aalto University, P.O. Box 11000, FI-00076 Aalto www.aalto.fi

Author
Marcus Engdahl

Name of the doctoral dissertation
Multitemporal InSAR in land-cover and vegetation mapping

Publisher School of Electrical Engineering

Unit Department of Radio Science and Engineering

Series Aalto University publication series DOCTORAL DISSERTATIONS 178/2013

Field of research Space technology and remote sensing

Manuscript submitted 1 February 2013 **Date of the defence** 15 November 2013

Permission to publish granted (date) 21 October 2013 **Language** English

☐ **Monograph** ☒ **Article dissertation (summary + original articles)**

Abstract

Synthetic Aperture Radar (SAR) is an active microwave instrument that has a number of favourable characteristics, one of which is its independence from lighting conditions or cloud cover, which make it an indispensable instrument for earth observation from space. Classification of land cover and vegetation mapping are some of the major uses of SAR in environmental monitoring, and in order to reach the full potential of the SAR instrument, a coherent technique called SAR interferometry (InSAR) should be utilised. The so-called repeat-pass InSAR-techniques are possible only if the satellite is on a repeating orbit with a relatively short repeat-period (up to two weeks at C-band).

This research focuses on multitemporal repeat-pass InSAR datasets from the Tandem-mission of the ERS-1 and ERS-2 satellites, which provided a time-series of InSAR-acquisitions with a 24-hour temporal baseline, a baseline which is very favourable to land-cover and vegetation mapping at C-band. The main research topic for this thesis is the assessment of the information content of a multitemporal InSAR time-series from an applications perspective. The work has concentrated on three application domains - land cover classification, stem volume estimation in boreal forests and the estimation of agricultural crop heights.

This study demonstrates that multitemporal ERS-1/2 Tandem InSAR data is clearly superior to non-interferometric (intensity-only) data, and that the applications-potential of the data is very high for land cover classification, high to very high for boreal forest stem volume estimation and moderate to high for the estimation of agricultural crop heights. During the study novel methods were developed for both land cover classification and boreal forest stem volume estimation, as well as for their combination. An outline for an operational system for land cover classification and vegetation using multitemporal InSAR data is presented. The methods developed in this thesis can be utilised with data from the C-band ESA Sentinel-1 constellation, whose 12- and 6-day repeat InSAR data can be expected to make a large impact in both land cover classification and vegetation mapping.

Keywords remote sensing, earth observation, radar, synthetic aperture radar, SAR, SAR interferometry, InSAR, multitemporal analysis, multitemporal InSAR, land-cover classification, crop height, boreal forest stem volume estimation, vegetation mapping

ISBN (printed) 978-952-60-5415-5 **ISBN (pdf)** 978-952-60-5416-2

ISSN-L 1799-4934 **ISSN (printed)** 1799-4934 **ISSN (pdf)** 1799-4942

Location of publisher Helsinki **Location of printing** Helsinki **Year** 2013

Pages 174 **urn** http://urn.fi/URN:ISBN:978-952-60-5416-2

Tekijä
Marcus Engdahl

Väitöskirjan nimi
Monen ajankohdan SAR-tutkainterferometria maankäytön luokittelussa ja kasvillisuuden kaukokartoituksessa

Julkaisija Sähkötekniikan korkeakoulu

Yksikkö Radiotieteen ja -tekniikan laitos

Sarja Aalto University publication series DOCTORAL DISSERTATIONS 178/2013

Tutkimusala Avaruustekniikka ja kaukokartoitus

Käsikirjoituksen pvm 01.02.2013 **Väitöspäivä** 15.11.2013

Julkaisuluvan myöntämispäivä 21.10.2013 **Kieli** Englanti

☐ **Monografia** ☒ **Yhdistelmäväitöskirja (yhteenveto-osa + erillisartikkelit)**

Tiivistelmä

Synteettisen apertuurin tutka (SAR) on aktiivinen mikroaaltoinstrumentti jolla on useita hyödyllisiä ominaisuuksia, esimerkiksi riippumattomuus valaistusolosuhteista tai pilvipeitteestä. Nämä ominaisuudet tekevät SAR-tutkasta korvaamattoman instrumentin maapallon havainnoinnissa avaruudesta. Maankäytön luokittelu ja kasvillisuuden kartoitus ovat eräitä SAR tutkan pääkäyttökohteita ympäristön kaukokartoituksessa. SAR-tutkan täysi potentiaali tämäntyyppisessä kaukokartoituksessa saavutetaan hyödyntämällä instrumentin koherenttia luonnetta niinkutsutussa SAR-tutkainterferometriassa, joka vaatii että SAR-tutkaa operoidaan toistuvalta radalta niin että radan toistojakso on varsin lyhyt (alle kaksi viikkoa C-taajuusalueen tutkalla).

Tässä tutkimuksessa on keskitytty monen ajankohdan interferometrisiin datasetteihin jotka on kerätty ERS-1 ja ERS-2 satelliittien nk. Tandem-kampanjojen aikana, jolloin radan interfetometrinen toistojakso oli vain 24-tuntia, mikä soveltuu erityisen hyvin maankäytön luokitteluun ja kasvillisuuden kartoittamiseen C-taajuusalueella. Tutkimuksen päätutkimuskohde on monen ajankohdan interferometrisen SAR-aikasarjan informaatiosisällön arviointi sovellusnäkökulmasta. Tutkimustyö on keskittynyt kolmelle sovellusalueelle – maankäytön luokitteluun, metsän runkotilavuuden arviointiin sekä viljelykasvien pituuden arviointiin.

Tämä tutkimus osoittaa että monen ajankohdan interferometrinen ERS-1/2 Tandem aikasarja on hyödynnettävyydessään ylivoimainen ei-interferometriseen (vain intensiteetti) aikasarjaan verrattuna. Tällaisen interferometrisen aikasarjan sovelluspotentiaali on maankäytön luokittelussa erittäin korkea, korkeasta erittäin korkeaan metsän runkotilavuuden arvioinnissa ja keskinkertaisesta korkeaan viljelykasvien pituuden arvioinnissa. Tutkimuksen aikana kehitettiin uusia menetelmiä sekä maankäytön luokitteluun, metsän runkotilavuuden arviointiin, että niiden yhdistelmään. Lisäksi väitöstyössä esitetään menetelmä operatiiviseen maankäytön luokitteluun ja metsän runkotilavuuden arviointiin monen ajankohdan interferometriselta SAR-aikasarjalta. Tässä työssä kehitettyjä menetelmiä voidaan käyttää myös C-taajuudella toimivan Euroopan Avaruusjärjestön Sentinel-1 tutkasatelliitti konstellaation keräämän datan kanssa.

Avainsanat kaukokartoitus, maapallon havainnointi, tutka, synteettisen apertuurin tutka, SAR, SAR interferometria, InSAR, maankäytön luokittelu, viljelykasvien pituus, metsän runkotilavuuden arviointi, kasvillisuuden kaukokartoitus

ISBN (painettu) 978-952-60-5415-5 **ISBN (pdf)** 978-952-60-5416-2

ISSN-L 1799-4934 **ISSN (painettu)** 1799-4934 **ISSN (pdf)** 1799-4942

Julkaisupaikka Helsinki **Painopaikka** Helsinki **Vuosi** 2013

Sivumäärä 174 **urn** http://urn.fi/URN:ISBN:978-952-60-5416-2

Them bats is smart; they use radar.

- David Letterman

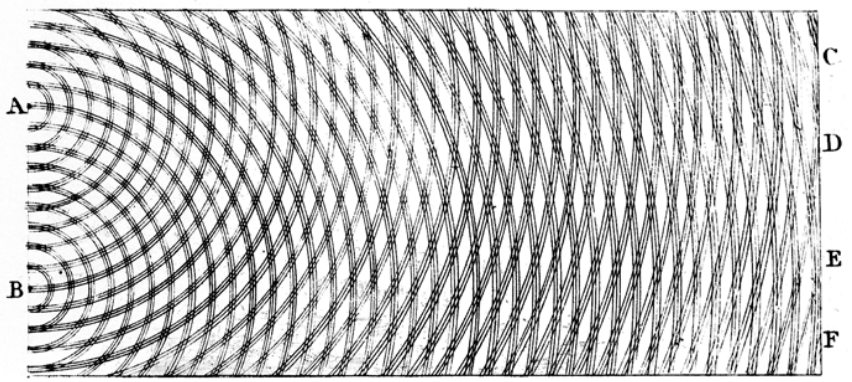

Thomas Young's sketch of two-slit diffraction of light. Narrow slits at A and B act as sources, and waves interfering in various phases are shown at C, D, E, and F. Young presented the results of this experiment to the Royal Society in 1803.

Preface

The research reported in this thesis was mostly done when I was a researcher in the Laboratory of Space Technology in the Helsinki University of Technology (HUT, now Aalto University). First and foremost I would like to thank my supervisor Martti Hallikainen both for employing me in his laboratory in 1996 and supporting my research efforts both during and after my stay in HUT. Part of the data processing and research for this work was performed while I was visiting the ESA-ESTEC in Holland for a year, and I'd like to thank Michael Rast and Maurice Borgeaud for support and advice during my stay. I stopped doing full-time research in 2003 when I joined the ESA-ESRIN in Italy, and I would like to thank my boss Yves-Louis Desnos for supporting my efforts in putting this thesis into writing and pushing me towards the finishing line.

I am grateful towards many people who I've been working with during the years. The scientific discussions I had with both Jouni Pullianen and Juha Hyyppä were invaluable as were the practical advice I received from them. I was lucky to be acquainted with Jarkko Koskinen who introduced me to several new people including Einar-Arne Herland, who became the supervisor of my M. Sc. thesis, and also Juha Hyyppä thanks to whom I applied for a job in the Laboratory of Space Technology in HUT. I really enjoyed working in HUT, around the turn of the millennium the Laboratory of Space Technology was a great place to work in and the funny and weird things that kept happening there on a daily basis could fill a small book.

This work has been supported by personal grants from the Emil Aaltonen Foundation, Finnish Academy of Science and Letters, HPY Research Foundation and Jenny and Antti Wihuri Foundation – I think it's great that such institutions support early-career scientists and I'm very grateful for their support.

Lastly, I want to thank my parents who have been supportive throughout my studies, no matter how long they have lasted.

In Frascati, 10.10.2013

Marcus Engdahl

List of Appended Papers

This dissertation is based on the research in following five papers, hereafter referred to as Papers A-E:

Paper A

M. E. Engdahl, M. Borgeaud and M. Rast, "The use of ERS-1/2 Tandem Interferometric coherence in the estimation of agricultural crop heights", IEEE Transactions on Geoscience and Remote Sensing, 39(8), 1799-1806, 2001 (Engdahl et al. 2001)

Paper B

J. Pulliainen, M. E. Engdahl and M. Hallikainen, "Feasibility of multi-temporal interferometric SAR data for stand-level estimation of boreal forest stem volume", Remote Sensing of Environment, 85(4), 397-409, 2003 (Pulliainen et al. 2003)

Paper C

M. E. Engdahl and J. Hyyppä, "Land-cover classification using multitemporal ERS-1/2 InSAR data", IEEE Transactions on Geoscience and Remote Sensing, 41(6), 1620-1628, 2003 (Engdahl and Hyyppä 2003)

Paper D

M. E. Engdahl, J. Pulliainen and M. Hallikainen, "Boreal forest coherence-based measures of interferometric pair suitability for operational stem volume retrieval", IEEE Geoscience and Remote Sensing Letters, 1(3), 228-231, 2004 (Engdahl et al. 2004)

Paper E

M. E. Engdahl, J. Pulliainen and M. Hallikainen, "Segment-based stem volume retrieval in boreal forests using multitemporal ERS-1/2 InSAR data", Canadian Journal of Remote Sensing, 34(1), 46-55, 2008 (Engdahl et al. 2008)

Paper A deals with the observed relationship between ERS-1/2 Tandem interferometric coherence and observed heights of agricultural crops on the agricultural area of Flevoland in the Netherlands. In this paper I performed InSAR processing, data gathering, data analysis and the writing of the paper while the other authors acted as scientific advisors.

Paper B studies stem volume estimation on boreal forest stands using multitemporal ERS-1/2 Tandem InSAR data on a test-site in Tuusula, Finland. A novel technique for stem volume estimation based on inverting the HUT semi-empirical backscattering-coherence model was developed, and its performance in stem volume estimation was assessed against ground-based reference data. In addition, the effects of environmental conditions on InSAR coherence and stem volume retrieval were studied. In Paper B my responsibility was InSAR processing, data gathering, writing the sections of the paper related to SAR Interferometry and InSAR processing, and contributing to the discussion-section. J. Pulliainen was responsible for the development of the HUT backscattering-coherence model, data analysis and the writing of the rest of the paper, while M. Hallikainen acted as a scientific advisor.

Paper C deals with using multitemporal ERS-1/2 Tandem InSAR data for land-cover classification in the Helsinki metropolitan area in Finland using a novel two-stage unsupervised hybrid classifier. In Paper C my responsibility was InSAR processing, data gathering, development of the hybrid classifier, data analysis and the writing of the paper. J. Hyyppä acted as a scientific advisor.

In ***Paper D*** a novel quality-measure was developed for assessing the suitability of InSAR image pairs for boreal forest stem volume retrieval. The analysis was done over the Tuusula test-site using InSAR data from the ERS-1-2 Tandem mission. In this paper I performed InSAR processing, data gathering, development of the novel quality-measure, data analysis and the writing of most of the paper. J. Pulliainen computed the stem volume estimates by inverting the HUT backscattering-coherence model and was involved in writing the sections about the HUT model and its inversion. M. Hallikainen acted as a scientific advisor.

In ***Paper E*** a segmentation-based method for simultaneous land-cover classification and stem volume estimation was developed, and its performance in stem volume retrieval was assessed against ground-based measurements and estimates from the satellite-based National Forest Inventory (NFI) of Finland. In this paper I was responsible for InSAR processing, data gathering, the segmentation and classification of InSAR data, data analysis and the writing of most of the paper. J. Pulliainen computed the stem volume estimates by inverting the HUT backscattering-coherence model and was involved in writing the sections about the HUT model and its inversion. M. Hallikainen acted as a scientific advisor.

List of Abbreviations

AMI	Active Microwave Instrument
ASAR	Advanced SAR
CEOS	Committee on Earth Observation Satellites
CV	Coefficient of Variation
EM	Electromagnetic
ENL	Equivalent Number of Looks
EO	Earth Observation
ERS	European Remote Sensing Satellite
ESA	European Space Agency
DEM	Digital Elevation Model
DInSAR	Differential InSAR
ESTEC	European Space Research and Technology Centre
FCS	Fuzzy Clustering Segmentation
FM	Frequency Modulated
GCP	Ground Control Point
GIS	Geographic Information System
GSV	Growing Stock Volume
HUT	Helsinki University of Technology
HUTSCAT	Helsinki University of Technology Scatterometer
ICC	Interferometric Coherence-Contrast
InSAR	Interferometric SAR
IWCM	Interferometric Water Cloud Model
LIDAR	Light Detection and Ranging
LOS	Line-Of-Sight
MIMICS	Michigan Microwave Canopy Scattering model
MLC	Maximum Likelihood Classification
MLE	Maximum Likelihood Estimate
MODIS	Moderate-resolution Imaging Spectroradiometer
NASA	National Aeronautics and Space Administration
NBFZ	Northern Boreal Forest Zone
NESZ	Noise-Equivalent-Sigma-Zero
NFI	National Forest Inventory (of Finland)
NN	Nearest Neighbour
OVoG	Oriented Volume over Ground
PC	Principal Component
PCT	Principal Components Transformation
PDF	Probability Density Function
POLSAR	Polarimetric SAR
Pol-InSAR	Polarimetric SAR Interferometry

PRF	Pulse Repetition Frequency
PS	Persistent Scatterer
PSF	Point Spread Function
RADAR	Radio Detection and Ranging
RAR	Real Aperture Radar
RCS	Radar Cross Section
RMS	Root Mean Square
RMSE	Root Mean Square Error
RMSE%	Root Mean Square Error percentage
RS	Remote Sensing
RT	Radiative Transfer
RVoG	Random Volume over Ground
SAR	Synthetic Aperture Radar
SLAR	Side-Looking Airborne Radar
SLC	Single-Look Complex
SNR	Signal-to-Noise-Ratio
SRTM	Shuttle Radar Topography Mission
S-1	Sentinel-1
TanDEM-X	TerraSAR-X add-on for Digital Elevation Measurement
TS	Threshold Scheme
UTM	Universal Transverse Mercator
WCM	Water Cloud Model

List of Symbols

α	Local slope angle
β_o	Brightness estimate
Γ	Gamma-function
δ_{az}	Azimuth-resolution
δ_g	Ground-range - resolution
δ_r	Range-resolution
Δ_r	Variance of the Gaussian random motion component in range
Δ_z	Variance of the Gaussian random motion component in height
$\bar{\gamma}$	Complex InSAR correlation
ϕ	Phase
ϕ_{int}	Interferometric phase
λ	Wavelength
θ	Look-angle
θ_I	Incidence angle
$\theta_{I,local}$	Local incidence angle
ω	Angular frequency
σ	Radar Cross-Section (RCS)
σ^o	Backscattering coefficient
σ^0_{dB}	Backscattering coefficient in decibel scale
τ	Pulse duration
a	Azimuth-coordinate in a SAR image
A_{ill}	Illuminated surface area
A	Amplitude
B_{int}	Interferometric baseline
B_{perp}	Perpendicular component of the interferometric baseline
B^{crit}_{perp}	Critical baseline in the perpendicular direction
BW_r	Range bandwidth
c	Speed of light in vacuum
f	Frequency
G	Ground-range distance
G_{ant}	Antenna gain
G_{grat}	Period of a grating
h_A	Altitude of ambiguity
H	Altitude of radar platform
I	Intensity (power)
I_N	N-look intensity image

L_{phys}	Length of the physical antenna in the azimuth-direction
L_{SA}	Length of synthetic aperture
n	Speckle noise intensity
N	Number of independent samples
P_r	Received power
P_t	Transmitted power
r	Range-coordinate of a SAR image
$\bar{r}$	Location vector
R	Slant-range distance
v	Velocity of radar platform
W_{beam}	Width of the radar beam on the ground
$\overline{Z}$	Complex SAR image

1. Introduction

1.1. Earth Observation with Remote Sensing Satellites

Earth Observation (EO) satellites give us the irreplaceable capability of observing the surface of our whole planet both regularly and frequently. According to the Committee on Earth Observation Satellites (CEOS) the CEOS member agencies are during the next 15 years (from 2008 onwards) operating or planning around 240 EO satellite-missions carrying over 385 different instruments (S. Ward 2008). These *Remote Sensing* (RS) satellites and instruments gather information that is vital both for environmental monitoring and the management of natural resources. According to Lillesand et al. 2007, remote sensing is defined as the science and art of obtaining useful information about an object, area or phenomenon through the analysis of data acquired by a device that is not in physical contact with the object, area, or phenomenon under investigation. In other words, RS is based on measuring, from afar, the physical influence of the studied object, area or phenomenon on its surroundings. In practise this is achieved by observing radiation from afar, in most cases utilizing *electromagnetic* (EM) waves.

Broadly speaking, RS-instruments/sensors can be divided into two categories, *active* and *passive*. In active RS the sensor illuminates the target with radiation and information about it is inferred from the radiation reflected back by the target. Examples of active RS instruments include, for example, altimeters, LIDARs, limb sounders, most radars and scatterometers. In passive RS the target is not illuminated by the RS-system, but instead the system relies either on radiation emitted by the target itself, or on reflected radiation emitted by an external source like the Sun. Examples of passive RS instruments include cameras (at visible & infrared wavelengths), radiometers, spectrometers and *parasitic radars*. EO using EM-waves is only possible at wavelengths where the atmosphere is transparent and allows the radiation to travel between the satellite, and the Earth. There are three main *atmospheric windows*: the *optical window* (~0.3 - 1.1μm) spanning from ultraviolet to near-infrared, the *infrared window* (~8 - 14μm) at mid-infrared, and the *radio window* (~1cm – 11m) spanning the wavelengths from microwaves into radio waves.

1.2. Synthetic Aperture Radar (SAR)

SAR is a side-looking active microwave instrument that produces high-resolution images of the reflectivity of the ground at microwave wavelengths (spanning from centimetres to metres depending on the sensor). The resolution of SAR imagery varies between few tens of centimeters and a few hundred meters with image swath-widths ranging from a few kilometres up to over 500 km. Since SAR is an active instrument that illuminates the target with microwave pulses and constructs the image from the received echoes, it is not dependent on external light/energy sources like sunlight for image formation. As microwaves penetrate cloud-cover and weather-phenomena very well (somewhat depending on the wavelength used), a SAR can in principle be used in imaging during both day and night and in all weather conditions. Unlike passive optical instruments which are frequently hampered by cloud cover, an orbital SAR can in principle guarantee the imaging of virtually any point on the surface of the Earth within a couple of days, depending on latitude, the satellite orbit and the steerability of the radar beam. An important property of SAR is that it is a *coherent* imaging system, meaning that the phases of the radar pulses used to illuminate the target are tightly controlled. The coherent nature of SAR causes the interference effects evident on SAR images and enables Interferometric SAR (InSAR) observations. SAR is discussed on a more technical level in Chapter 2.

SAR-data have a multitude of applications in many fields of EO, for example over land it is used in agricultural monitoring, forestry, geology, hydrology, land-cover classification and mapping, and the remote sensing of ice (glaciers and ice sheets) and snow. In addition it is possible to combine suitable SAR acquisitions into InSAR observations, which have their own set of applications that are discussed in the next section. Over the sea, SAR-data is used for example in sea-ice mapping, ship and iceberg detection, the mapping of surface winds and waves, detection of oil-slicks, tracking of ocean-swell systems, and radial surface-current mapping.

1.3. Interferometric SAR (InSAR)

Interferometric SAR (InSAR) is based on the coherent combination of two or more SAR images. This dissertation deals with spaceborne repeat-pass across-track InSAR, which is the most common form of spaceborne SAR interferometry today. This type of InSAR is based on cross-correlating (or *interfering*) two SAR images of the target acquired at different times from the same or slightly different orbit position in space. Another type of across-track InSAR is the so-called *single-pass interferometry,* where the images to be interfered are acquired at the same time – in practise this is accomplished either with a two-satellite constellation flying in formation like in the TanDEM-X case, or placing the other antenna at the end of a long boom as with the Shuttle Radar Topography Mission (SRTM). The so-

called *interferometric phase*, an InSAR observable, carries information about the geometry of the target at the scale of the radar wavelength. With InSAR it is possible to generate Digital Elevation Models (DEMs) of the target area and to detect very small changes in target geometry taking place between the image acquisitions. These small geometric changes can be used to infer target properties that are complementary to the information in individual SAR images. InSAR is discussed on a more technical level in chapter 3.

In addition to topographic mapping InSAR-data has been successfully utilised in numerous EO-applications including, for example, agricultural monitoring, studies of atmospheric phenomena, studies of earthquakes and ground motion, change detection, forestry, monitoring of glaciers and ice sheets, land-cover classification, and volcanology, to name a few.

1.3.1. The ERS-1/2 Tandem Mission

This dissertation studies data from the main ERS-1/2 Tandem campaign in 1995-1996. During the Tandem-campaigns the ERS-1 and ERS-2 satellites were flown in the same orbital plane and the orbits were phased in such a way that the ground-track of ERS-2 coincided with that of ERS-1 24 hours earlier. The Tandem-dataset was unique in the sense that it was the first set of regular (every 35 days) spaceborne InSAR observations with a short temporal baseline of 24 hours. The great benefit of using such a short temporal baseline is that most natural targets (agricultural fields, boreal forests etc.) retain at least some coherence over the one-day interval, which enables retrieving information about their properties via InSAR observations. Unfortunately ERS-1/2 Tandem data was only gathered on a campaign-basis with the vast majority of the data gathered between during 1995-1996. The density-map of the ERS-1/2 Tandem coverage in the ESA archives is presented in Figure 1.

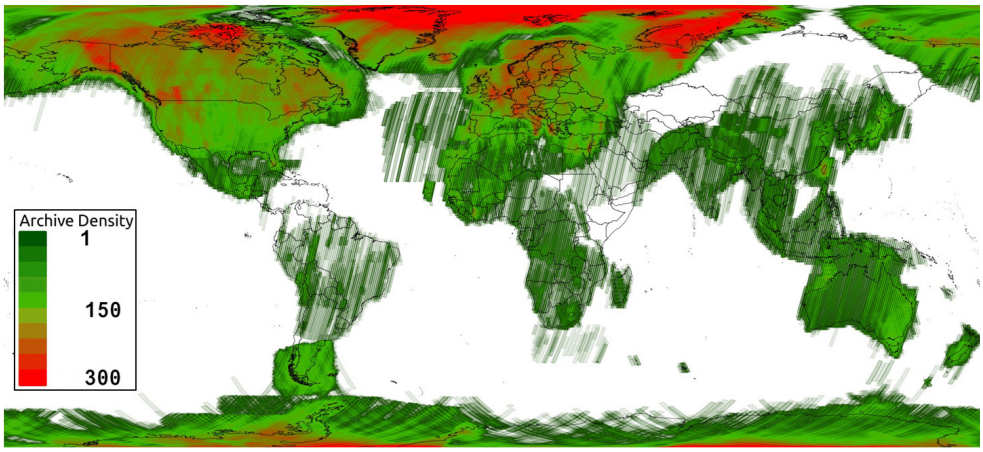

Figure 1. The density of the ERS-1/2 acqusitions in the ESA archive during the main Tandem campaign (1995-1996). Density of 1 equals one acquired scene.

1.4. Motivation and Structure of the Dissertation

The subject of this dissertation is "*Multitemporal ERS-1/2 Tandem InSAR in Land-Cover and Vegetation Mapping*". The motivation for this work has been the uniqueness of the ERS-1/2 Tandem dataset, which already at first glance appears to contain a wealth of information related to land-cover and vegetation parameters. However, even though the Tandem dataset clearly contains relevant information about land-cover and vegetation, it is also evident that weather conditions during and immediately before the Tandem observation have a strong influence on the Tandem InSAR observations. Therefore, the work presented in this dissertation is an empirical study into the potential of multitemporal ERS-1/2 Tandem InSAR data in land-cover and vegetation mapping. More specifically, the study seeks answers to the following central question:

> *What is the real potential and information content of ERS-1/2 Tandem InSAR time-series for land-cover and vegetation mapping?*

This main question gives rise to the following sub-questions:

a) *What is the contribution of the Tandem coherence time-series in land-cover classification compared with intensity-only time-series?*
b) *Can the Tandem InSAR coherence be related to the heights of agricultural crops?*
c) *How well does the Tandem time-series suit stem-volume retrieval in Boreal forest and how do weather conditions and seasonality affect the results?*
d) *How can the most suitable Tandem-observations for stem-volume retrieval be picked from a time-series of InSAR observations?*

The answers to the questions above pertain not only to the multitemporal ERS-1/2 Tandem InSAR dataset studied in this work, but also to any similar future dataset consisting of a multitemporal time-series of C-band InSAR observations with short temporal baselines.

The following methods for land-cover classification and vegetation mapping have been developed in this dissertation:

- A novel two-stage hybrid land-cover classifier for multitemporal InSAR data.
- Improvements to the semi-empirical HUT backscattering-coherence model for stem-volume retrieval.
- A method for identifying the most suitable InSAR observations for stem volume retrieval.
- A segmentation-based method for the combined land-cover classification and stem-volume retrieval from multitemporal InSAR data.

It should be noted that even though segmentation and the HUT model are used in the study, the main emphasis of this work is on studying the information content of short temporal baseline multitemporal C-band InSAR data, and not on the development of segmentation methods, or the HUT model.

The structure of this dissertation is as follows: The research-section is documented in the five published articles that are appended to this dissertation; Chapter 1 consists of the introduction to this work; Chapter 2 covers the fundamentals of SAR imaging and SAR images; Chapter 3 covers the fundamentals of SAR Interferometry; Chapter 4 consists of the introduction to multitemporal InSAR observations of terrain; Chapter 5 presents the advances made in this work and how they relate to research done elsewhere and Chapter 6 contains the conclusions and outlook.

2. Fundamentals of SAR and SAR Images

This chapter covers, in basic and simplified terms, the theory and concepts necessary for understanding the operating principles of *Synthetic Aperture Radar* (SAR) and the properties of SAR images. For a more general technical treatment of SAR and SAR imaging see Henderson and Lewis 1998, Oliver and Quegan 1998 or Bamler and Hartl 1998.

2.1. Radars

Radars are active RS instruments that illuminate targets or target areas by sending out electromagnetic (EM) waves through an antenna. Some of these EM-waves are scattered back toward the radar by the targets and the received echoes are used to infer the location and some properties of the targets. Radars underwent rapid development during the Second World War when they were used to detect enemy vessels and aircraft; the acronym RADAR was coined at that time and it stands for ***RA***dio ***D***etection ***A***nd ***R***anging. Radars are active instruments so they illuminate the targets by themselves. Therefore, unlike with passive RS instruments, the functioning of radars is not dependent on other sources of electromagnetic waves like the sunlight, or radiation emitted by the target itself. The active operating principle and the used microwave-wavelengths makes most radars largely independent on lighting and weather conditions, enabling day-and-night all-weather operations.

There are many different types of radars for different application domains like *detection and search radars* for detecting and tracking aircrafts, missiles and ships, *marine radars* used for navigation at sea, *weather radars* for tracking precipitation in the atmosphere and *side looking radars* that are used in remote sensing and mapping to form radar images of the target or target area. Search, marine and weather radars utilise a spinning antenna to project a beam of electromagnetic waves into the observation space. While they can be mounted on a moving platform, their operation is not based on the movement of the radar platform with respect to the target. Side-looking radars like SAR, on the other hand, do depend on the relative movement between the target and the radar.

2.2. Side-Looking Radars

Side-looking radars belong to a sub-class of radars that produce images of the target area by utilising a side-looking antenna that is mounted on a moving platform (usually *airborne* or *spaceborne*). Side-Looking Airborne Radars (SLAR) and Synthetic Aperture Radars (SAR) are the two main side-looking radar types. The EM-waves emitted by the radar are scattered in the target, and the backscattered echoes that are received by the antenna are used in the construction of the *radar image*. In the so-called *monostatic* case the same antenna is used for both transmitting and receiving while in the *bistatic* case the transmitting and receiving antennas are at different locations. *Single-polarisation* radars send and receive pulses in a single polarisation state (for example both transmitting and receiving in vertical polarisation). *Dual-polarisation* radars also send out pulses in a single polarisation state, but in addition to receiving in the same polarisation state they also receive in another, usually orthogonal polarisation state (for example transmitting in vertical and receiving both in vertical and horizontal). The polarisation states used during transmit and receive are designated with two letters, for example VV for Vertical transmit and Vertical receive, and VH for Vertical transmit and Horizontal receive. *Fully-polarimetric (quad-pol)* radars both send and receive in two orthogonal polarisation states (for example vertical and horizontal). For a more comprehensive description of SAR imaging, see for example Henderson and Lewis 1998 or Oliver and Quegan 1998.

This dissertation uses data from spaceborne monostatic single-polarisation SARs and unless stated otherwise, the discussion is implicitly referring to such SARs.

2.2.1. Imaging Geometry

This section discusses the imaging geometry of side-looking radars. To illustrate the principles we present an idealised case in which the radar platform flies in a straight line over flat terrain. A rigorous treatment of the imaging geometry in real-world cases would require the taking into account of several additional effects. These effects include, for example, pointing-errors of the radar antenna and motion-compensation in the airborne radar platform case. In the spaceborne case rigorous treatment would require taking into account effects caused, for example, by the curvature and rotation of the Earth and the curvature of the orbital path of the radar.

Figure 2 depicts the imaging geometry of a monostatic side-looking radar flying in a straight line over flat terrain at altitude H. Radar is essentially a ranging instrument that measures range (distance) to targets residing within the *beam footprint*. The radar platform moves along the *platform track* with velocity v, and the radar sends out electromagnetic waves as a stream of *pulses* towards the ground through a side-looking *radar antenna*. The direction along the platform track is called the *along-track* or *azimuth*-direction and the direction of the radar Line-Of-Sight

(LOS) is called the *across-track* or *range*-direction. The antenna projects a *beam* in the across-track direction towards the target making an angle θ - also called the *look angle* - with the vertical direction. Vectors pointing from the radar towards the nadir and towards the centre of the beam footprint span the so-called *range-plane*. Targets within the beam footprint are illuminated by the pulses sent out by the radar, and some of them will *scatter* part of the incident EM energy back towards the radar antenna. In the monostatic case in which the same antenna is used for both transmit and receive, scattering back towards the antenna is called *backscattering* and the objects/targets causing the backscattering are called *scatterers*. The distance *R* from radar to a scatterer (within the range-plane) is called the *slant range* and the distance *G* from the scatterer to the radar nadir point is called the *ground range*. Movement of the radar platform along its track causes the beam footprint to sweep a *swath* on the ground. The part of the swath closer to the radar is called *near-range* and the part farther away is denoted *far-range*.

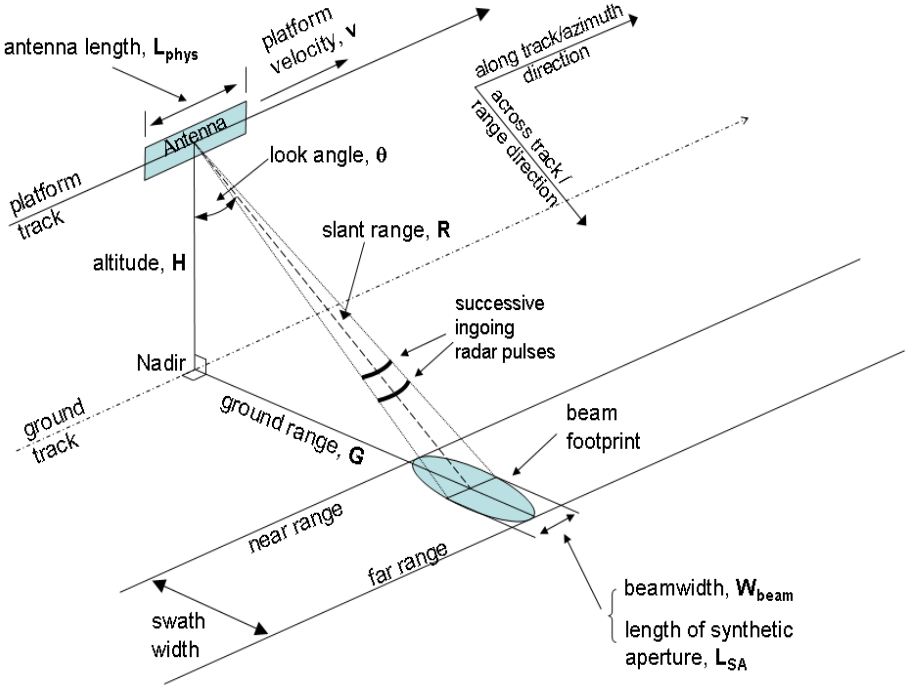

Figure 2. Imaging geometry of side-looking imaging radars flying over flat terrain in a straight line.

2.2.2. Resolution

For side-looking radars *resolution* is loosely defined as the minimum distance at which the radar can discriminate between two closely spaced scatterers with responses of approximately equal strength. The *Point Spread Function* (PSF) describes the radar response to an ideal point like target and resolution is often defined using the width of this function. For any radar-system, the fundamental rule is that the available resolution is equal to one over the system *bandwidth* (Henderson and Lewis 1998; Oliver and Quegan 1998). For side-looking radars the resolution is defined in two perpendicular dimensions; in the along-track or azimuth direction and in the across-track or range direction. Resolution in the along-track direction is denoted *azimuth resolution* and resolution in the range direction is called *range resolution*.

2.2.2.1. Range Resolution

Side-looking radars are essentially ranging devices that measure distance in the range-direction/plane by measuring the time-delay of the backscattered pulse echoes. Due to this basic operating principle, side-looking radars map the location of scatterers in the across-track direction based on their slant-range distance from the radar. This causes certain inherent geometric distortions in SAR images that are discussed in section 2.3.5. A consequence of this distance-based imaging in range is that side-looking radars cannot distinguish between objects that are equidistant from the radar within the range-plane (see (Figure 3)). Equidistant scatterers will be mapped into the same resolution cell, even if the distance between them is large. In effect imaging in the range-plane is a mapping/projection from the 2-D range-plane onto a 1-D line (see Bamler and Hartl 1998).

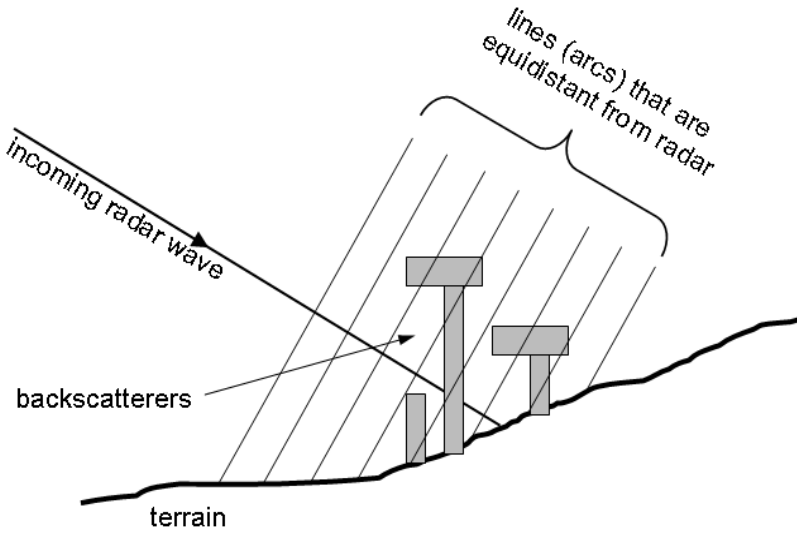

Figure 3. Illustration of equidistant arcs from the radar in the range-plane. In the spaceborne case where the radar is far away from target the incoming waves are approximately planar and the arcs can be approximated with lines.

For side-looking radars the resolution in the range-direction is dictated by the length of the radar pulse; in order to achieve high resolution, the pulse has to be made as short as possible. For a simple rectangular pulse the range bandwidth BW_r of the pulse is:

$$BW_r = \frac{1}{\tau} \tag{1}$$

where τ is the duration of the pulse. Since the pulse-length in space is the product of the pulse duration and the speed of light c, the range resolution δ_r is:

$$\delta_r = \frac{c\tau}{2} = \frac{c}{2BW_r} \tag{2}$$

where the factor two is due to the round-trip of the radar pulse to the targets and back. In practise the radar pulses cannot be made arbitrarily short because there are practical limits on peak transmitter power and sufficient EM energy needs to be delivered to illuminate the target in order to reach the required *Signal-to-Noise-Ratio* (SNR). Therefore the peak transmitter power and required SNR dictate the length of the pulse. Fortunately, it is possible to utilise pulse-forms which provide more bandwidth than a simple rectangular pulse of the same duration. Modern side-looking radars send out relatively long *phase-modulated* pulses - so-

called Frequency Modulated (FM) 'chirps' that can be "compressed" into short impulse-like pulses using matched filtering during SAR processing. In practise the matched filtering step consists of convolving the received pulse with a replica of the transmitted pulse. This technique is called *pulse compression, range compression* or *range focusing* (see for example Henderson and Lewis 1998 or Bamler and Hartl 1998). The ratio of the duration of the uncompressed pulse to the compressed pulse is called the *pulse-compression ratio.*

2.2.2.2. Azimuth Resolution

Early side-looking radars functioned as Real Aperture Radars (RARs), and were called Side-Looking Airborne Radars or SLARs. RARs were more common in the early days of radar because both the construction of the radar and the necessary data processing are considerably simpler than in SARs. RAR and SAR have similar range-resolutions, but SAR achieves finer azimuth-resolution thanks to the construction of a *synthetic aperture* during SAR processing.

For a RAR the azimuth resolution is diffraction-limited and dictated by the along-track length L_{phys} of the radar antenna (see Figure 2). A longer antenna produces a narrower beam and therefore a better azimuth resolution is achievable. The azimuth resolution $\delta_{az,RAR}$ for RAR is therefore equal to the beamwidth W_{beam} on the ground and is given by the product of the distance to the target and the angular resolution of a diffraction-limited antenna:

$$\delta_{az,RAR} = W_{beam} = R\frac{\lambda}{L_{phys}} \tag{3}$$

According to (3) the azimuth resolution of a RAR depends on the range R to the target. Practical limits on the length of the physical radar antenna are a limiting factor for the azimuth resolution of a RAR – acceptable azimuth resolution can be realised in the airborne case but from orbit the highest achievable azimuth resolution will be in the order of kilometres.

SAR achieves high resolution in the azimuth-direction by effectively creating a much longer antenna with a technique called *aperture synthesis* during *SAR processing*. The length of the synthetic aperture L_{SA} is limited by the amount of time the target spends within the beam footprint on the ground - also called the *integration time* or *dwell time*. The length of the synthetic aperture is therefore approximately equal to the beam width, which is determined by the length of the physical antenna:

$$L_{SA} \approx R\frac{\lambda}{L_{phys}} \tag{4}$$

This is illustrated in Figure 4. As the moving radar passes the target, it emits pulses at the *Pulse Repetition Frequency* (PRF) and each successive

pulse is emitted from a different position along the platform track. The echo of each transmitted pulse contains the coherent sum of the backscattering from all the scatterers within the radar beam. Due to the movement of the radar the contributions of the individual scatterers are Doppler-shifted depending on their azimuth location within the radar beam (they all have zero Doppler-shift when they pass the middle of the beam). In other words, the train of radar echoes contains the coherently summed *phase-histories* of all the scatterers in the scene as they are illuminated at different azimuth positions within the beam footprint by successive radar pulses. A SAR system is able to utilise these phase-histories and create a long synthetic aperture during SAR processing, which drastically improves the azimuth resolution compared with RARs. This is achieved by matched filtering in SAR-processing step called *azimuth focusing* or *azimuth compression*. In practise this step is performed by convolving the range-focused data with a reference function that reconstructs the phase-history for each slant-range position (the Doppler-history of a target depends on its range-distance from the radar).

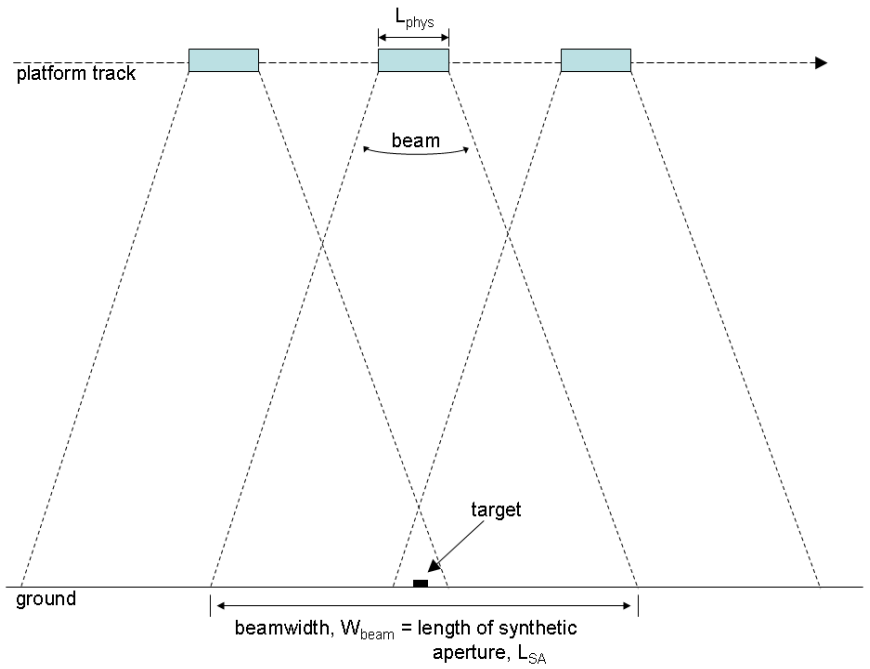

Figure 4. The synthetic aperture. As the radar moves along its track and images the target from successive positions, a synthetic aperture much longer than the physical size of the antenna can be created.

For a physical antenna of length L_{phys} the beam width on the ground is given by equation (3). The antenna pattern of a physical antenna is formed by the phase shifts due to the one-way path difference between the elements of the antenna and the ground. However, the effective antenna pattern of a synthetic antenna is formed by the two-way path difference between the antenna and the ground, so the effective beam width is halved and the azimuth resolution of a fully focused SAR is given by:

$$\delta_{az,SAR} = R\frac{\lambda}{2L_{SA}} \approx \frac{L_{phys}}{2} \tag{5}$$

Thus remarkably the azimuth resolution of a SAR does not depend on imaging distance or wavelength but only on the length of the physical antenna. A shorter antenna produces a wider beam and a longer synthetic aperture, and therefore higher azimuth resolution, provided that the used PRF is high enough.

2.2.3. Radar Backscattering

As discussed earlier, side-looking radars form images of the complex radar reflectivity of the target area. If the parameters of the used radar are known it is possible to infer the strength of the radar backscatter from the backscattered power received by the radar.

2.2.3.1. Point-like and Distributed Scatterers

If a single strong scatterer is dominating the return from a resolution cell, the type of scattering is called *point scattering* and the type of scatterer is called a *point scatterer* or a point-like scatterer. Good examples of artificial point scatterers are three- and two-sided *corner reflectors*, also called *trihedral* and *dihedral* scatterers. Corner reflectors with a known radar response are essential in *calibration* of radar images. Typically, however, the radar return from a resolution cell consists of the combined backscatter of many individual elemental scatterers. This type of scattering is called *distributed scattering* and the type of scatterer is called a *distributed scatterer*.

The return from a single point-like target is essentially stable in amplitude, which changes only slowly with changing wavelength or incidence angle. This is not the case with distributed scatterers where the responses from the individual elemental scatterers interfere with one another. Consequently the radar response of a distributed scatterer is a random variable with some probability distribution, and the reflectivity estimate obtained in a radar measurement must be understood to be a sample from this distribution (see section 2.3 for discussion of the properties of SAR images).

2.2.3.2. *The Radar Equation*

As discussed, radars make observations by illuminating the target with EM-energy and measuring the returns that are scattered by the target. The *radar equation* describes the relation between transmitted power, received power, and scattering by the target. In the monostatic single-pulse case, the power received by the antenna due to backscattering from a pointlike target at range R is given by (Ulaby and Dobson 1989; Henderson and Lewis 1998):

$$P_R = P_T \left(\frac{G_{ant}^2 \lambda^2}{(4\pi)^3 R^4} \right) \sigma \tag{6}$$

where P_R and P_T are the received and transmitted powers, G_{ant} is the gain of the radar antenna and σ is the *Radar Cross Section* (RCS) of the target. Equation (6) can be extended to distributed targets by integrating the backscattered power over the illuminated surface area A_{ill}:

$$P_R = P_T \int_{A_{ill}} \left(\frac{G_{ant}^2 \lambda^2}{(4\pi)^3 R^4} \right) \sigma^0 dA \tag{7}$$

where σ^0 is the unitless *backscattering coefficient* that represents the backscattered return per unit surface area. When the properties of the radar system and the imaging geometry are known, the radar equation can be used to estimate the power backscattered by the target.

2.2.3.3. *Radar Cross Section*

The RCS (σ) has the units of area (m^2) and it describes the strength of the backscattered radar return from a pointlike target through the radar equation (see equation (6)). For historical reasons the RCS is normalised so that it describes the projected area of a metal sphere (an isotropic scatterer) that, if substituted for the target, would backscatter the same amount of power back to the radar. It needs to be kept in mind that the area expressed by the RCS is only very loosely connected to the size of the scatterer in the real world as the RCS depends heavily on the directivity of the backscattering caused by the shape of the object. In general, the RCS depends on the shape of the target, its dielectric constant, viewing geometry (orientation of the scatterer), and the used wavelength. For example at X-band the RCS of a human being is of the order of $1m^2$, whereas the RCS of a trihedral corner reflector with 1m long sides at their intersection is roughly 4500m2 (Henderson and Lewis 1998).

2.2.3.4. Backscattering coefficient

Similarly to the RCS, the backscattering coefficient σ^o describes the amount of backscattered power compared with the power incident on the scene for distributed scatterers (see equation (7)). It is unitless because it has been normalized by the illuminated surface area. Often the normalisation is done using the incidence angle θ_i, i.e. a flat terrain is assumed:

$$\sigma^0 = \frac{\beta_0}{\sin\theta_i} \tag{8}$$

where β_o is the *brightness estimate* obtained by the radar. β_o is the estimated backscattered power detected by the radar in slant-range geometry that is independent from the incidence angle and local topography (Raney et al. 1994). If the local topography of the terrain is known, local incidence angle $\theta_{i,local}$ should be used in equation (8) to properly normalize the backscattered power. It has been recommended in the literature that σ^o is only used in conjunction with calibrated radar systems (Henderson and Lewis 1998). The backscattering coefficient is often expressed in *decibels*, i.e.:

$$\sigma^0_{dB} = 10\log_{10}(\sigma^0) \tag{9}$$

Due to the normalisation of RCS and σ^o the backscattering coefficient in decibels σ^0_{dB} conveniently describes the directivity of the scattering: 0 dB corresponds to isotropic scattering, positive values to scattering that focuses energy towards the radar and negative values to scattering that focuses energy away from the radar.

2.2.4. Properties of the ERS-1/2 SAR

The European Remote-Sensing (ERS) satellites 1 and 2 are two EO satellites of the European Space Agency (ESA) with a SAR as their primary instrument. The identical SAR-instruments on-board the ERS 1 & 2 are called the Active Microwave Instrument (AMI). The properties of the ERS-missions and the AMI are listed in Table 1.

Table 1. Properties of the identical ERS-1 & 2 missions and their on-board SAR.

Centre Frequency f	5.3 GHz (C-band)
Wavelength λ	5.66 cm
Polarisation	Linear, VV
Incidence Angle	23° at mid-swath
Swath Width	100 km
Orbital velocity v	~7.5 km/s
Peak Power	4.8 kW
Pulse Repetition Frequency	~1700 Hz (variable)
Uncompressed pulse duration τ	37.1 μs
Uncompressed pulse length $c\,\tau$	11.13 km
Pulse-compression ratio	579.7
Compressed pulse duration	64 ns
Compressed pulse length $c\,\tau$	19.19 m
Antenna Size	10 m x 1 m (az x height)
Pixel Spacing (SLC)	7.9 m x 4 m (slant rg x az)

It is instructive to review the properties of the ERS AMI in the light of the discussion in the previous sections. The AMI has a PRF of about 1700 Hz and the platform orbital velocity is ~7.5 km/s, so a pulse is emitted roughly every 4.4 meters of platform movement during imaging and successive pulses sent towards ground are separated by about 175 kilometres in slant range during their propagation through space. The length of the uncompressed pulse is 11.1 km in slant-range, which gives a slant-range resolution of roughly 5.5 km (see equation (2)). The pulse-compression ratio is ~580, which yields a compressed pulse-length of ~19 meters and a slant-range resolution of ~9.6 meters. Ignoring the curvature of the Earth the 782 km platform altitude together with the 23° incidence-angle translates to ~850 km slant-range distance to mid-swath. Equation (3) then gives us a beamwidth of ~4.8 km on the ground, which would also be the azimuth resolution in the RAR-case and which is the length of the synthetic aperture in the SAR-case. Azimuth-resolution in the SAR-case is ~5 m, which equates to half of the azimuth length of the SAR antenna, as stated in equation (5). Compared with RAR-operation the use of SAR imaging has increased the azimuth resolution by a factor of almost one thousand.

2.3. Properties of SAR images

2.3.1. SAR as a Coherent Imaging System

The illuminating electromagnetic field produced by SAR is a coherent and essentially *monochromatic* field that has non-random phase fronts. This coherent nature of SAR enables the cross-correlation of two SAR observations in SAR interferometry, and gives rise to the interference effects seen on SAR images. These effects are not present in non-coherent imaging that relies on incoherent radiation with random phase fronts for scene illumination. For example passive optical remote sensing is based on utilising the wide-spectrum incoherent radiation from the Sun.

2.3.2. Phase and Speckle

SAR images have a characteristic grainy and noise-like "salt and pepper" appearance that complicates image analysis. This is caused by the so-called *speckle-effect* that results from the coherent nature of SAR. All imaging systems capture some information of scene-elements that are smaller than the resolution cell. In non-coherent imaging systems - like optical imaging using a camera – signals from individual scene elements do not interfere and their combined signal can therefore be computed by adding them together *in power*. In coherent imaging systems like SAR the reflections from individual scatterers interfere with one another and the signal from a resolution cell is the *vector sum* of the contributions of all the sub-resolution scene-elements. In other words, speckle in coherent systems is caused by the *interference* of the coherent returns from the individual scene elements. This is illustrated in Figure 5 and equation (10).

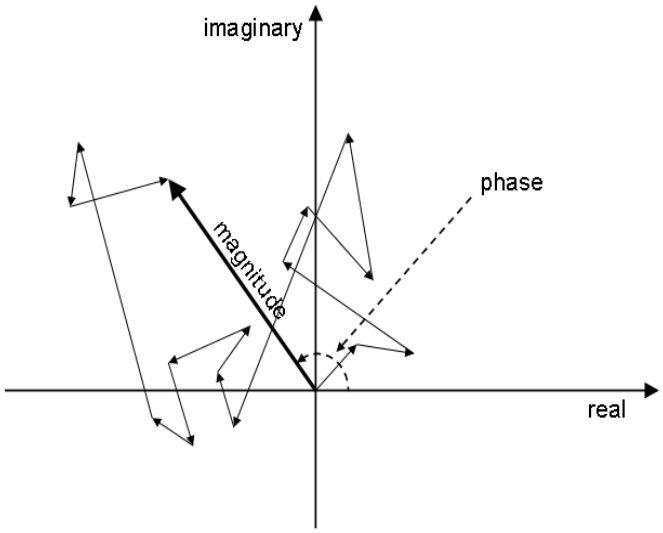

Figure 5. Diagram illustrating how for coherent systems like SAR, the observed complex reflectivity is a vector sum of the contributions of individual scatterers.

Distributed targets can be modelled to consist of a large number of discrete and independent "elementary" scatterers (the first-order Born approximation), and the total return from each resolution cell is calculated as the vector sum of their contributions:

$$Ae^{i\phi} = \sum_{k=1}^{N} A_k e^{i\phi_k} \tag{10}$$

where the summation is over the N elementary scatterers, each of which contributes to the total complex backscatter with amplitude A_k and phase ϕ_k. The phases and amplitudes of the elementary scatterers are not directly observable by the radar because their size is much smaller than the resolution of the radar; only their vector sum $Ae^{i\phi}$ can be observed. The phase of the radar return from an individual scatterer depends on its distance R_k from the radar as well as its internal structure:

$$\phi_k = \frac{4\pi}{\lambda} R_k + \phi_k^{scat.} \tag{11}$$

where $\phi_k^{scat.}$ is the phase-change due to the internal structure of the scatterer. For natural distributed scatterers one can safely assume that the positions of the independent scatterers within the resolution cell are random, which implies that their phases ϕ_k are randomly distributed on the interval [0,2π). Only artificial targets like gratings and fences can be assumed to have non-random (correlated) positions. It follows from equations (10) and (11) that the observable complex radar reflectivity $Ae^{i\phi}$

varies from resolution cell to resolution cell even over areas that are statistically homogenous. This complicates estimating the underlying radar reflectivity of a scene because the noise-like speckle-effect makes estimates based on one or a small number of resolution cells inherently unreliable. Therefore it is necessary to distinguish between the measured value at each pixel, and the underlying radar reflectivity σ. One also has to note that even though speckle is random and appears noise-like, it is deterministic and a real feature of the scene in the sense that repeated identical (same geometry) radar observations of the scene will detect the same speckle-pattern. Another notable issue is that the phase ϕ only gives an ambiguous estimate of the distance to the scatterers in the target (see section 3.3.1). Since the complex exponential function is periodic and the phase in bounded to the interval $[0,2\pi)$ there are numerous radar-target distances that give rise to the same observed phase. For example, changing the distance between the radar and the target by multiples of half of the used wavelength would not change the observed phase at all.

2.3.3. SAR Image Types

As discussed, a SAR image is essentially a measurement of the complex radar reflectivity of the imaged scene. This section introduces the concepts of *complex* and *detected* SAR images as well as the concept of SAR *looks*.

2.3.3.1. Complex Images

A complex SAR image $\overline{Z}$ can be expressed in its amplitude- and phase parts in the following way:

$$\overline{Z}(r,a) = A(r,a)e^{i\phi(r,a)} \tag{12}$$

where r and a are image coordinates (in range and azimuth), A is the *amplitude* image and ϕ is the *phase* image. Focused complex SAR images usually have a single look and they are usually presented in slant-range geometry (see sections 2.3.3.3 and 2.3.5.1). Images of this kind are customarily called *Single-Look Complex* (SLC) images. Complex SAR images are needed for example in SAR interferometry (see Chapter 3), which is based on exploiting the phase-information in SAR images.

2.3.3.2. Detected Images

SAR images intended for human viewing or non-InSAR applications are usually delivered in detected form where the phase-information has been removed from the images. In practise this is done in a processing-stage called detection that determines the strength of the radar signal at each pixel, and the resulting images are called detected images. A common detection-process is *square-law detection*, where the complex SAR image $\overline{Z}$ is multiplied by its complex-conjugate $\overline{Z}^*$ so that an *intensity* image

$I=A^2$ is formed. Intensity images are directly proportional to the energy (power) backscattered from each pixel.

2.3.3.3. Single-Look and Multilooked Images

So-called *single-look* SAR images utilise the whole available synthetic aperture to achieve the highest azimuth resolution realizable with the SAR system. Single-look images have high spatial resolution, but due to the speckle-effect the radar reflectivity estimates in single-look images are noisy, and their radiometric accuracy/resolution is poor.

Multilooking is an operation where the radiometric accuracy/resolution of SAR data is improved at the expense of spatial resolution. This can be achieved during SAR processing by dividing the synthetic aperture into N parts and producing *N* lower resolution images - also called looks - from the single SAR data take, and averaging them together incoherently. The underlying assumption is that the separate looks are imaging the same underlying radar reflectivity σ, which is not always true in practise. Another approach to multilooking is to take an incoherent spatial average of a single-look SAR image. Here the underlying assumption is that the radar reflectivity is constant over some neighbourhood surrounding the pixel of interest, which is also not always true in practise. Both of these approaches are statistically equivalent and produce an *N-look* SAR image with reduced spatial resolution and increased radiometric resolution (reduced speckle).

2.3.4. Spatial Resolution and Pixel Size

Spatial resolution is loosely defined as the minimum distance at which the radar can discriminate between two closely spaced scatterers that have responses of approximately equal strength. Note that resolution differs from *pixel size*, which is related to how densely the scene reflectivity has been *sampled*. This difference between resolution and pixel size is illustrated in Figure 6. In properly sampled SAR images the pixel size is smaller than resolution which implies that adjacent pixels are correlated with one another.

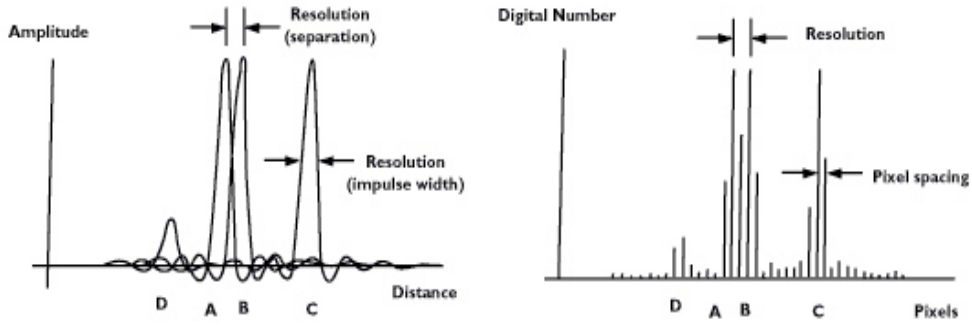

Figure 6. Illustration of the difference between resolution and pixel spacing (image courtesy ESA).

2.3.5. Geometric Properties of SAR Images

Side-looking radars are essentially ranging devices that map scatterers in the across-track direction based on their slant-range distance from the radar, which causes inherent distortions in the resulting imagery. If the terrain is completely flat, a simple slant- to ground-range projection corrects for the distortion. In the presence of terrain relief the situation is more complicated as it gives rise to effects like *foreshortening*, *layover* and *shadowing* in SAR imagery.

2.3.5.1. Slant- and Ground Range

SAR maps the position of scatterers in the across-track direction based on their slant-range distance R from the radar and produce an image that is said to lie in *slant-range* geometry. The end-users of SAR data often prefer images that have been projected into *ground-range*, where scatterer positions are based on their ground-range distance *G* from the radar nadir (assuming flat terrain). Slant-range distances are converted into ground-range distances in the following way:

$$G = R\sin(\theta) \tag{13}$$

where θ is the look angle that is varying over the imaged swath. Even though the range resolution of radars is constant in slant-range, it follows from equation (13) and the changing look angle over a scene that in ground-range geometry the image resolution is better in far-range than in near-range. The differences between ground- and slant-range projected images are illustrated in Figure 7.

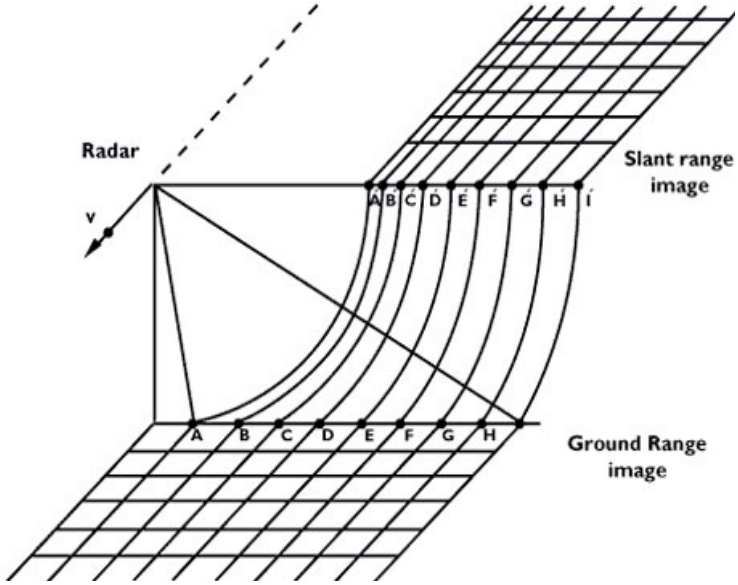

Figure 7. Illustration of slant-range and ground-range images. Points that are equidistant in ground-range are not equidistant in slant-range (image courtesy ESA).

2.3.5.2. Local Geometry

Figure 8 depicts the local imaging geometry inside the radar beam footprint within the range plane. The angle between the propagation-vector of the radar wave and the vertical is called the *incidence angle* θ_i. This is practically identical to the look angle in the airborne case, but for spaceborne radars the curvature of the planet makes the incidence angle larger than the look angle. *Local incidence angle* $\theta_{i,local}$ is the angle between the surface normal and the propagation vector of the radar wave and the *local slope angle* α is the angle between the surface tangent and the horizontal.

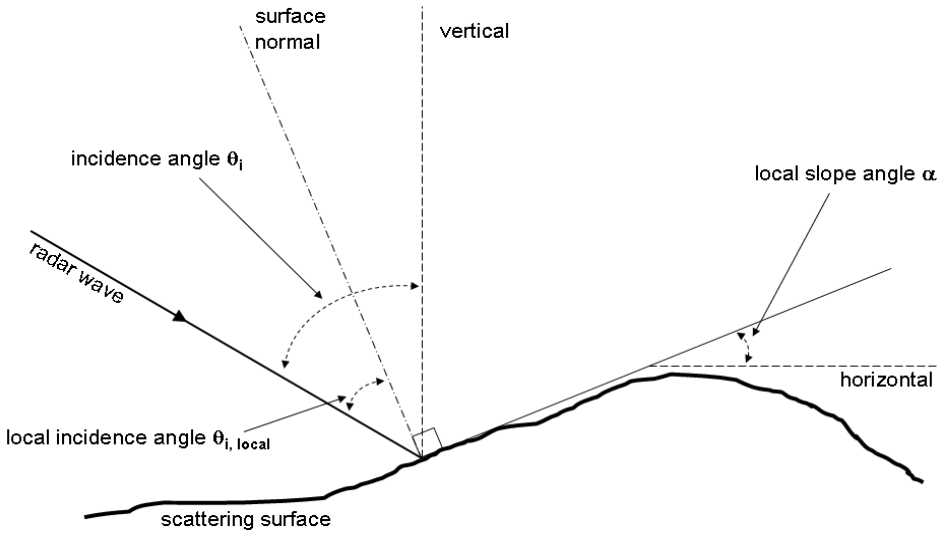

Figure 8. Local imaging geometry at the scattering surface inside the beam footprint. All vectors are in the range-plane.

2.3.5.3. Foreshortening, Layover and Shadowing

Terrain relief causes geometric effects in SAR images because the elevation of a scatterer affects the slant-range distance between it and the radar, and therefore also the range position of the image of that scatterer. Therefore, terrain relief affects the location, and even ordering of scene features on SAR images. In some cases the presence of terrain relief masks other areas so that they cannot be imaged by the SAR at all. These geometric effects caused by terrain relief are called *foreshortening*, *layover* and *shadowing*.

Foreshortening

Foreshortening is the apparent compression in topographic features in the scene and it makes radar-facing fore-slopes of mountains to appear to "lean" towards the radar. Maximum foreshortening takes place when a steep slope is orthogonal to the radar beam, so that the top and bottom of the slope are imaged onto the same position in slant-range.

Layover

If the slope facing the radar is so steep that the top of the slope is closer to the radar than the bottom, it will be imaged before it in the slant-range image. This effect is called the layover, because the top of a mountain is "laying over" the foot of the mountain. Layover images targets that are physically far away from each other into the same image pixel, and the signals from these two targets are irreversibly mixed.

Shadowing

When terrain-relief is blocking the line-of-sight between the radar and an area in the scene, radar pulses are not able to interact with the terrain at all and the area passes into radar shadow. The shadowed areas on SAR images do not carry any information about the reflectivity of the terrain but only contain instrument noise.

2.3.5.4. Effect of Incidence Angle

The incidence angle has a strong effect on the overall geometric appearance of SAR images. At steep incidence angles there is more foreshortening and there are also more problems with layover. On the other hand, the use of shallow incidence angles diminishes foreshortening and layover, but at the same time more of the terrain will be left in the radar shadow.

2.3.5.5. Geocoding

The effects of the inherent geometric distortions in SAR imaging can be mitigated in a process called *geocoding*, where precise information about the imaging geometry and terrain relief in the form of a *Digital Elevation Model* (DEM) are used to project the data into a chosen map-projection where each imaged terrain feature is located at its correct map-coordinates.

2.3.6. Statistical Properties of SAR Images

The statistical properties of SAR images depend on the type of target being imaged, the format of the image (amplitude, intensity etc.) and the number of looks.

2.3.6.1. Fully Developed Speckle

Speckle is said to be "fully developed" when the following assumptions hold (Henderson and Lewis 1998):

1. There are a large number of scatterers contributing to the signal at each observation opportunity (N is large).
2. None of the scatterers is so strong that it tends to dominate the total reflected signal (a distributed scatterer is being observed).
3. The contributing scatterers are statistically independent of each other.
4. The phases of the contributing scatterers are uniformly distributed over $[0,2\pi)$ (placement is random within the resolution cell).

The first three assumptions are the basis of the *central limit theorem*, from which it follows that the real and imaginary parts of the observed complex radar reflectivity $Ae^{i\phi}$ are statistically independent Gaussian random variables. The fourth assumption assures that the real and imaginary parts of $Ae^{i\phi}$ have equal variances and that it obeys circular

complex Gaussian statistics. For medium resolution (tens of metres) spaceborne remote sensing SARs these assumptions hold for most natural scatterers such as forests, agricultural fields, rough water, soil or rock surfaces (Bamler and Hartl 1998). The assumptions can be violated for example in urban scenes where there may be only a few dominant scatterers in a resolution cell or when resolution is extremely high.

2.3.6.2. The Multiplicative Noise Model for Speckle

Fully developed speckle is often modelled as a multiplicative random noise process that is statistically independent of the scene. The intensity *I* observed by the radar can be modelled as the product of the underlying radar reflectivity σ and speckle noise intensity *n*:

$$I = \sigma n \tag{14}$$

The *Probability Density Function* (PDF) of the noise intensity is a negative exponential function (Oliver and Quegan 1998):

$$pdf(n) = e^{-n}, n \geq 0 \tag{15}$$

with mean and variance of unity. Therefore, in the multiplicative noise model the observed radar intensity I may be regarded as the result of multiplying a deterministic underlying radar reflectivity by negative exponentially distributed speckle noise.

2.3.6.3. Statistics of Single-Look SAR Images

Measurements taken by a SAR-system must be understood as being samples of a random variable. Single-channel and single-look SAR images exhibiting fully developed speckle obey the following statistical distributions (from Oliver and Quegan 1998):

1. The real- and imaginary parts of the observed complex radar reflectivity, $z_r = A\cos\phi$ and $z_i = A\sin\phi$, are statistically independent Gaussian random variables with mean of zero and variance of $\sigma/2$. Their joint PDF is:

$$pdf(z_r, z_i) = \frac{1}{\pi\sigma} e^{\left(-\frac{z_r^2 + z_i^2}{\sigma}\right)} \tag{16}$$

2. The observed phase ϕ is uniformly distributed over [0,2π).

3. The amplitude A obeys the Rayleigh distribution:

$$pdf(A) = \frac{2A}{\sigma} e^{\left(-\frac{A^2}{\sigma}\right)}, A \geq 0 \quad (17)$$

The distribution has a mean value of $\sqrt{\pi\sigma}/2$ and standard deviation of $\sqrt{(1-\pi/4)\sigma}$. The *Coefficient of Variation* (CV), defined as the standard deviation divided by the mean, is $\sqrt{4/\pi - 1} \cong 0.523$ for amplitude data.

4. The intensity $I = A^2$ has a negative exponential distribution:

$$pdf(I) = \frac{1}{\sigma} e^{\left(-\frac{I}{\sigma}\right)}, I \geq 0 \quad (18)$$

For this distribution both the mean value and the standard deviation are σ, with CV = 1.

The preceding distributions apply for each scene pixel. Note that because the phase is uniformly distributed, it does not carry any useful information of the (distributed) target. Therefore the phase of a single single-channel SAR image is practically useless and detected image types where the phase-information has been discarded are usually preferred. It should be noted that even though the phase is random, it is a deterministic and repeatable measurement of the random internal structure within a pixel. The phase is needed in SAR interferometry where the phases of two or more SAR images are coherently combined.

Except for the phase ϕ all the distributions are completely characterized by the parameter σ which carries all the available information about the target. σ corresponds to the *average backscattered intensity* (power), as the mean of distribution (18) reveals.

2.3.6.4. Statistics of Multilooked Intensity Images

The multilooked *N-look* average intensity I_N is defined as:

$$I_N = \frac{1}{N}\sum_{k=1}^{N} I_k \tag{19}$$

where I_k are independent samples from the exponentially distributed intensity PDF with mean σ (see equation (18)). The PDF of the N-look intensity obeys the Gamma-distribution with order parameter σ:

$$pdf(I_N) = \frac{1}{\Gamma(N)}\left(\frac{N}{\sigma}\right)^N (I_N)^{N-1} e^{-\frac{NI_N}{\sigma}}, I_N \geq 0 \tag{20}$$

where Γ is the Gamma-function. This distribution has the mean value of σ and standard deviation of $\sigma/\sqrt{N}$ giving it a CV of $1/\sqrt{N}$. Compared with single-look intensity multilooking therefore reduces the standard deviation by a factor of $1/\sqrt{N}$. Due to these properties of the distribution in equation (20) it is possible to estimate the number of actual independent samples that have been averaged to produce a multilooked image by estimating the so-called *Equivalent Number of Looks* (ENL):

$$ENL = \frac{(mean)^2}{\mathrm{var}\, iance} \tag{21}$$

where the mean and variance are estimated in intensity over a statistically homogenous target. ENL is often used to estimate the smoothing effects of image processing operations like resampling or speckle filtering.

3. Fundamentals of SAR Interferometry

This chapter covers, in basic and simplified terms, the theory and concepts necessary for understanding SAR Interferometry (InSAR), or more specifically across-track InSAR. General reviews of SAR interferometry, its techniques and applications can be found in Gens and Van Genderen 1996, Massonnet and Feigl 1998 and Ferretti et al. 2007. For a technical review of SAR interferometry from a signal theoretical perspective, see Bamler and Hartl 1998.

3.1. SAR Interferometry

SAR interferometry (also called Interferometric SAR or InSAR) is based on the coherent combination of complex SAR images. As discussed in the preceding chapter, the phase of a single SAR image is essentially random and therefore does not convey any useful information about the target. However, the coherent combination of the phases of two or more SAR images does carry useful target information, and the exploitation of these phases forms the basis of SAR interferometry.

There are several ways of forming a *SAR interferometer*. The used SAR images must differ from one another in some aspect in order for this combination to be useful - usually they differ in their imaging geometry, imaging time, or both. With differing imaging geometries it is meant that the images are acquired with antennas in slightly differing positions in space. In *along-track interferometry* the antennas are separated in the along-track direction of the SAR, and in *across-track interferometry* in the direction perpendicular to both the radar beam and the direction of the movement of the radar platform (platform track). In *repeat-pass interferometry* the interfering images are acquired at different times and in *single-pass interferometry* simultaneously using two or more antennas.

Across-track InSAR was introduced in the public domain in the 1970s originally for DEM generation in topographic mapping (Graham 1974), even though the InSAR concept was already known in military circles a decade earlier (Henderson and Lewis 1998). DEM generation is still one of the main application domains of SAR interferometry. InSAR also has the capability to detect and track sub-wavelength scatterer movement and it has been applied very successfully in the fields of tectonics, glaciology, volcanology and mapping of ground subsidence, for example. In addition,

InSAR has found many applications in land-cover mapping and retrieving biophysical parameters from natural targets like vegetation canopies (see for example Gens and Van Genderen 1996 or Massonnet and Feigl 1998).

This dissertation deals with spaceborne repeat-pass across-track InSAR, which is the most common form of spaceborne SAR interferometry today.

3.2. Repeat-Pass Across-Track InSAR

Repeat-pass across-track InSAR is based on cross-correlating (or *interfering*) two SAR images of the target acquired at different times from the same or slightly different position in space. The spatial separation of the antennas (platform tracks) at the time of the two imagings is called the *interferometric baseline* and the time separation between the acquisitions is called the *temporal baseline*.

The two cross-correlated images are said to form an *interferometric pair* and their cross-correlation forms a *SAR interferogram*. The phase of a SAR interferogram is called the *interferometric phase*. Another key parameter measured by InSAR is the *interferometric coherence*, which is a measure of the noisiness of the interferometric phase.

3.2.1. Imaging Geometry

Imaging geometry of across-track InSAR is illustrated in (Figure 9). The figure depicts the range plane and shows the distance between the orbit tracks of the SAR sensors at the time of the respective acquisitions. One of the acquisitions is denoted the *master* and marked with *"SAR 1"* and the *slave* is marked with *"SAR 2"*. R and θ denote the range and look angles. The distance between the platform tracks in the range plane is the interferometric baseline B_{int}, and its component perpendicular to the looking direction is called the *perpendicular/effective* baseline B_{perp}. It should be noted that the interferometric baseline may change in the azimuth-direction as the two platform-tracks are not necessarily fully parallel.

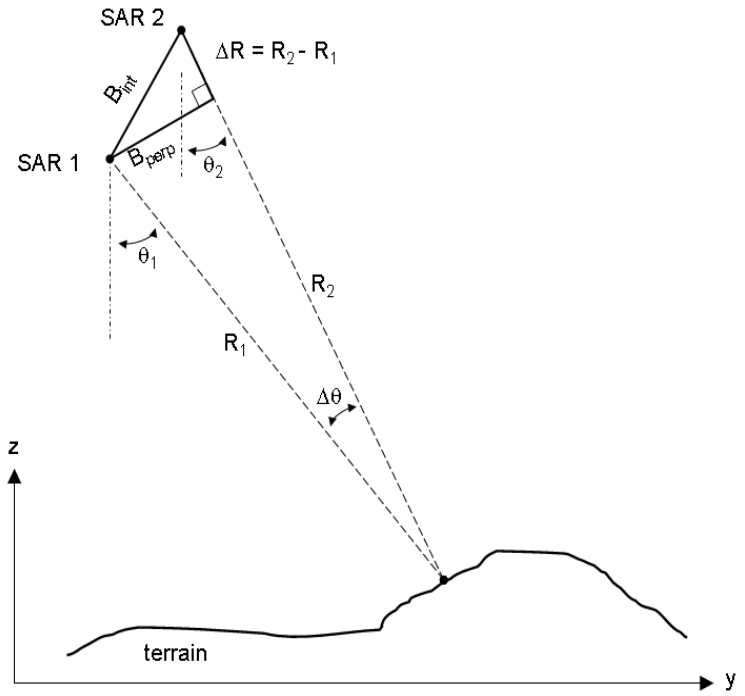

Figure 9. Imaging geometry of across-track InSAR. The image is in the range-plane.

3.2.1.1. The Spectral Shift Principle

In order to understand certain effects caused by the InSAR imaging geometry, it is necessary to interpret the backscattered signal as containing components of the spatial reflectivity spectrum of the ground. Since SAR can be assumed to be a linear measurement system (Henderson and Lewis 1998), any extended scatterer can be considered a superposition of sinusoidal gratings, and point scatterers (Bamler and Hartl 1998; Ferretti et al. 2007). The backscattered return from pointlike targets is very stable in amplitude, and is essentially unaffected by a slight change in viewing angle. However, for gratings the change of viewing angle changes the frequency observed by the radar due to Bragg-scattering effects (Henderson and Lewis 1998). In order for the grating to be visible, the radar returns from its scattering elements should reach the radar in-phase. If the period of the grating is defined to be $G_{grat}/2$, constructive interference happens when the Bragg-scattering condition is fulfilled (Ferretti et al. 2007):

$$\frac{c}{2f_{\max}\sin\theta} \le G_{grat} \le \frac{c}{2f_{\min}\sin\theta} \tag{22}$$

where f refers to the radar frequency and $f_{max}=f_{min}+BW_r$, where BW_r is the range-bandwidth (see equation (2)) of the radar (15.6MHz in the case of ERS-1&2). A grating that is tuned to the radar central frequency and fills a

whole range resolution-cell becomes invisible to the radar if the radar frequency changes from f to $f \pm BW_r/2$ (the edges of the available frequency band). Another way of looking at this effect is to note that if the two-way range-difference between the backscattered returns from the ends of the grating reaches half of the wavelength, the return from the whole grating is cancelled out (see also Figure 10).

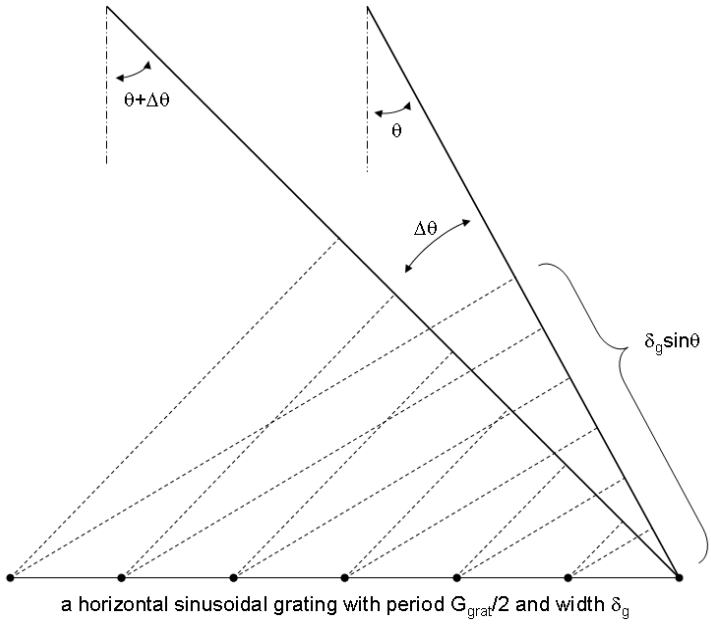

Figure 10. Illustration of the spectral-shift principle. A change in viewing angle changes the mapping from a spatial ground frequency to frequency observed by the radar.

A slight change in the viewing angle causes a shift in the imaged reflectivity spectrum of the ground. This frequency shift that depends on incidence angle is called the spectral shift and is illustrated in Figure 10. It can be shown that a small change in looking angle $\Delta\theta$ corresponds to a frequency shift Δf of (Gatelli et al. 1994):

$$\Delta f = \frac{-f_0 \Delta\theta}{\tan\theta} = \frac{-f_0 B_{perp}}{R \tan\theta} \tag{23}$$

where f_o is the centre frequency of the radar. This does not imply that changing the looking angle shifts the bandwidth of the radar, but it simply means that the observed reflectivity spectrum of the ground is shifted according to equation (23). A consequence of this is that the same part of the ground frequency spectrum can be imaged using radars with differing

centre frequencies, provided that the interferometric baseline is adjusted accordingly. This is the basis of the so-called cross-interferometry between ERS-2 and Envisat, in which a ~2km baseline is used to compensate for the 31Mhz difference in their centre frequencies (see Colesanti et al. 2003, Perissin et al. 2006, Santoro et al. 2007).

3.2.1.2. The Critical Baseline

All sinusoidal gratings become invisible due to destructive interference when the look-angle changes so that the two-way travel path difference between the nearest and farthest elementary scatterer is equal to the used wavelength λ. This happens when (see Figure 10):

$$2\delta_g \sin(\theta + \Delta\theta_{crit}) - 2\delta_g \sin\theta = \lambda \tag{24}$$

where $\delta_g = \delta_r / \sin(\theta)$ is the resolution in ground range. Because $\Delta\theta$ is small, it follows that:

$$\Delta\theta_{crit} = \frac{\lambda}{2\delta_g \cos\theta} = \frac{\lambda \sin\theta}{2\delta_r \cos\theta} = \frac{BW_r}{f} \tan\theta \tag{25}$$

, where the resolution in slant range is defined by the range bandwidth $\delta_r = c/2 \cdot BW_r$ (see equation (2)). This critical change of viewing-angle that makes all gratings disappear is reached when the satellite orbit shifts an amount that is equal to the so called *critical baseline*:

$$B_{perp}^{crit} = \frac{H\Delta\theta_{crit}}{\cos\theta} = \frac{H \cdot BW_r}{f} \frac{\sin\theta}{\cos^2\theta} \tag{26}$$

where H is the satellite altitude. In other words, when the difference in viewing angle is too large, the induced spectral shift is so big that the imaged ground spectra do not overlap anymore, and interferometry is no longer possible. According to equation (26) and the parameters of the ERS mission (see Table 1), the critical baseline for ERS interferometry is ~1060m. If the baseline is larger than this, interferometry will only be possible for point-like targets.

3.2.1.3. Common-Band Filtering

Only the overlapping parts of the range-spectra of the interfering images contribute to the coherent signal, while the non-overlapping parts contain only uncorrelated noise. Therefore the quality of interferograms can be improved by so-called *common-band filtering* in which the non-overlapping parts of the two range-spectrums are filtered out thereby reducing interferogram noise. In the absence of volumetric effects common-

band filtering removes the uncorrelated noise and increases the interferometric coherence (Gatelli et al. 1994.).

Analogically to the spectral shift in range caused by the baseline length, the differences in the pointing of the radar antenna (squint angle) cause shifts in the observed azimuth-spectra of the two images. Common-band filtering in the azimuth-direction is used to reduce interferogram noise in a similar fashion.

3.3. The Interferogram and the Interferometric Phase

A *SAR interferogram* is formed by acquiring two complex SAR images of the target, co-registering them accurately so that the imaged targets match on both images, and then *interfering* them by multiplying one pixel-by-pixel with the complex conjugate of the other (see equation (12)):

$$\overline{Z}_{\text{int}} = \overline{Z}_1 \overline{Z}_2^{\,*} = A_1 A_2 e^{i(\phi_1 - \phi_2)} = I_{\text{int}} e^{i\phi_{\text{int}}} \tag{27}$$

where $\overline{Z}_{\text{int}}$ is the complex interferogram, $\phi_{\text{int}} = \phi_1 - \phi_2$ is the interferometric phase and $I_{int}=A_1A_2$ is the interferogram magnitude. Note that there exists also another notation where the complex correlation $\bar{\gamma}$ is called the interferogram with its magnitude being the interferometric coherence $|\bar{\gamma}|$ and its phase $\angle\bar{\gamma}$ the interferometric phase (see equation (30)).

3.3.1. Interferogram Fringes and the "Wrapping" of the InSAR Phase

The interferometric phase is only measured modulo 2π, i.e. the phase is "wrapped" onto the interval $[0,2\pi]$. This wrapping causes the characteristic *fringe* pattern, or distinct iso-phase contours on the phase of SAR interferograms. For InSAR applications like DEM-generation where the unambiguous *absolute phase* is needed, the phase needs to be *unwrapped* first in a process called *phase unwrapping*.

3.3.2. Geometric Factors Contributing to the InSAR Phase

If we assume that the scattering phase of the target itself is the same on both acquisitions (see equation (11)) and ignore effects caused by possible ionospheric and atmospheric delays, the interferometric phase is given by (see Figure 9):

$$\phi_{\text{int}} = \frac{4\pi}{\lambda}(R_1 - R_2) = \frac{4\pi}{\lambda}\Delta R \tag{28}$$

which shows that the interferometric phase is very sensitive to changes in the distance between the scatterer and the radar during the time-period between the repeat-pass acquisitions. The interferometric phase is very sensitive to ΔR as a range-difference of just half the used wavelength causes a 2π phase-change, i.e. one fringe on the interferogram. The range-difference can be caused by either the movement of the scatterer(s) between the acquisitions in repeat-pass interferometry, which is the basis of *Differential InSAR* (DInSAR), or by the difference in viewpoint caused by the topography and the interferometric baseline itself. The general phase-trend in range is caused by the changing viewpoint in the range direction due to the increasing distance from the radar. Once this phase-trend has been removed from the interferogram during the so-called *flat-earth correction* step, the remaining fringe-pattern already closely resembles height-contours on a terrain-map. The height-sensitivity of the InSAR-phase to terrain elevation is usually gauged by the altitude of ambiguity h_a, i.e. the terrain height difference causing a 2π phase-change, i.e. a single fringe (Ferretti et al. 2007):

$$h_a = \frac{\lambda}{2} \frac{R_2 \sin \theta_1}{B_{perp}} \tag{29}$$

For example for the ERS-1/2 missions (see Table 1) a 150m perpendicular baseline translates to an altitude of ambiguity of around 63 metres (when ignoring the curvature of the Earth).

3.3.3. Basic InSAR Processing Steps

Dedicated software packages are normally used for InSAR processing, i.e. for coherently combining suitable complex SAR images in order to produce InSAR-derived products like the interferometric phase and the interferometric coherence. The main processing steps for interferogram and coherence-image generation are:

- Sub-pixel accuracy co-registration of the two images and resampling the slave acquisition into the geometry of the master.
- Common-band filtering of the images in range and azimuth in order to include only the common part of the image spectra in subsequent InSAR processing.
- Interferogram generation by interfering the two co-registered and common-band filtered images; possible complex-multilooking for phase noise reduction.
- Flat-earth correction for the interferometric phase
- Interferometric coherence estimation.

After these basic processing-steps the user can continue further depending on his/her needs to produce InSAR-derived digital elevation

models, differential interferograms for detecting movement of the ground etc.

3.4. Interferometric Coherence

So far in our discussion we have not addressed noise in the interferometric phase and the sources of such phase noise. The *complex interferometric coherence* is an estimate of the amount of phase noise in an interferogram and it is defined as the complex correlation coefficient between the two interfering SAR images:

$$\bar{\gamma} = \frac{E\left[\bar{Z}_1 \bar{Z}_2^*\right]}{\sqrt{E\left[\left|\bar{Z}_1\right|^2\right] E\left[\left|\bar{Z}_2\right|^2\right]}} \tag{30}$$

where $\bar{\gamma}$ is the complex interferometric coherence and *E[]* denotes the expectation-value operator. The absolute value of $\bar{\gamma}$ is called either the magnitude of coherence, interferometric coherence or simply "coherence". The phase of the complex coherence $\angle\bar{\gamma}$ gives the expected value of the interferometric phase ϕ_{int} of the pixel under study. As coherence is based on expectation values it cannot be determined over a single pixel and it is therefore of inherently lower resolution than the interferogram and the interfering SAR images.

The interferometric coherence $\left|\bar{\gamma}\right|$ is a key observable as it carries valuable information about the target at the scale of the radar wavelength. Due to the scaling by the denominator in equation (30) the values of $\left|\bar{\gamma}\right|$ vary between 0 (incoherence) and 1 (perfect coherence). Any noise in the observed interferometric phase will make $\left|\bar{\gamma}\right| < 1$. The coherence is high when the two interfering images represent the same or nearly the same interaction with a scatterer or a set of scatterers so that both images are observing a similar speckle pattern (Zebker and Villasenor 1992). Coherence is directly related to the signal-to-noise ratio (SNR) of the interferogram in the following way:

$$SNR = \frac{\left|\bar{\gamma}\right|}{1 - \left|\bar{\gamma}\right|} \tag{31}$$

Here the "signal" refers to the fringe pattern and "noise" to the phase noise superimposed on it. Sources of phase noise are discussed later in this chapter.

3.4.1. Coherence Estimation and Statistics

In practise the magnitude of coherence is usually estimated in the local neighbourhood using the following standard estimator and a sliding estimator window:

$$|\hat{\gamma}| = \frac{\left|\sum_{k=1}^{N} \overline{Z}_{1k} \overline{Z}_{2k}^{*}\right|}{\sqrt{\sum_{k=1}^{N} \left|\overline{Z}_{1k}\right|^2 \sum_{k=1}^{N} \left|\overline{Z}_{2k}\right|^2}} \tag{32}$$

where $|\hat{\gamma}|$ is the estimate on the coherence magnitude and the summations are over *N* samples in the local neighbourhood. This estimate is also the *Maximum Likelihood Estimate* (MLE) for the coherence magnitude - closed-form expressions for its PDF and moments are rather complex and have been presented in Touzi and Lopes 1996 and Touzi et al. 1999. Unfortunately, the coherence estimate of equation (30) is biased at low coherence magnitudes, especially when N is small (Joughin et al. 1994; Touzi et al. 1999). In these situations the estimator gives values that are higher than the "true" coherence magnitude. The estimator becomes asymptotically unbiased when the number of samples *N* becomes large. This needs to be kept in mind when estimating coherence over low-coherence areas like forests – too small window-sizes will lead to biased coherence estimates. Since the moments of equation (30) are rather tedious to evaluate in practise the variance of coherence is often estimated using the Cramer-Rao lower bound, even though it is only valid for *unbiased* estimators (Touzi et al. 1999):

$$\mathrm{var}(|\hat{\gamma}|)_{CR} = \frac{(1-|\overline{\gamma}|^2)^2}{2N} \tag{33}$$

This expression is valid for estimating the variance of coherence magnitude estimates when the coherence magnitude is high and the number of independent samples *N* is large, in other cases it overestimates the variance of coherence magnitude estimates.

3.4.2. Sources of Coherence Degradation

There are several sources of interferometric phase noise that cause decorrelation and lower the magnitude of coherence in repeat-pass SAR interferometry. The observed coherence is an estimate of the total decorrelation in the interferogram and if the total decorrelation is divided into its component terms, it is possible to isolate the terms that depend on the properties of the target (Zebker and Villasenor 1992). The total

observed coherence can be divided into its component terms for example as:

$$|\bar{\gamma}| = |\bar{\gamma}|_{thermal} \cdot |\bar{\gamma}|_{processor} \cdot |\bar{\gamma}|_{baseline} \cdot |\bar{\gamma}|_{volume} \cdot |\bar{\gamma}|_{azimuth} \cdot |\bar{\gamma}|_{temporal} \quad (34)$$

Here the first two terms are scene-independent; the next three depend on the interaction between imaging geometry and the target characteristics while the last term depends mainly on target properties. The components of equation (34) are now discussed separately.

3.4.2.1. Thermal Decorrelation

Thermal noise in the radar receiver causes decorrelation in an interferogram. In practise this effect is negligible except when dealing with areas where the radar backscatter is so low that it is close to the noise-floor of the radar (the *Noise-Equivalent-Sigma-Zero* or NESZ). This can happen over sufficiently calm water surfaces when most of the transmitted energy is scattered away from the radar. Therefore we can assume that over land $|\bar{\gamma}|_{thermal} = 1$.

3.4.2.2. Processor Decorrelation

Incorrect SAR or InSAR processing can cause decorrelation in an interferogram. Modern SARs and SAR-processors are *phase-preserving* and cause only negligible decorrelation in normal circumstances (i.e. no missing data lines etc.). Similarly modern InSAR processors cause negligible decorrelation unless the operator commits an error during the processing for example by allowing for too imprecise a co-registration. Assuming correct processing and no problems with the SAR data, processor decorrelation is negligible, i.e. $|\bar{\gamma}|_{processor} = 1$.

3.4.2.3. Baseline and Volume Decorrelation

Baseline decorrelation and volume decorrelation are both caused by the slight difference in the looking angle caused by the non-zero length of the interferometric baseline (longer baseline leads to larger decorrelation). Due to this effect the two interfering images are imaging different slices of the range frequency spectra of the ground. Only the overlapping parts of the imaged ground spectra can be correlated, and the non-overlapping parts contain only uncorrelated noise. Often the part of the decorrelation coming from the contribution of surface scatterers (thickness of scattering volume is zero) is counted into baseline decorrelation and the contribution from volume scattering into volume decorrelation.

Baseline and volume decorrelation differ in the sense that baseline decorrelation can be removed with common-band filtering in range so that $|\bar{\gamma}|_{baseline} = 1$. However, volume decorrelation cannot be compensated for and it carries useful information about the thickness of the scattering volume (large scatterer thickness leads to large volume decorrelation).

3.4.2.4. Azimuth Decorrelation

As with baseline decorrelation, differing squint-angles in the interfering images mean that different slices of the ground azimuth frequency spectra will be imaged. In the absence of volume scattering azimuth decorrelation can be removed with common-band filtering in azimuth so that $|\bar{\gamma}|_{azimuth} = 1$.

3.4.2.5. Temporal Decorrelation

Temporal decorrelation is caused by physical changes in the target between the two SAR acquisitions. In single-pass interferometry the temporal decorrelation is zero and $|\bar{\gamma}|_{temporal} = 1$. In repeat-pass InSAR estimates of temporal decorrelation can be used to deduce properties of the target, this is especially valuable for natural targets that decorrelate over varying timescales depending on target properties and environmental conditions.

3.4.2.6. Decorrelation Summary

Since thermal decorrelation and processor decorrelation are negligible and baseline decorrelation and azimuth decorrelation can be compensated for, equation (34) is reduced into:

$$|\bar{\gamma}| = |\bar{\gamma}|_{volume} \cdot |\bar{\gamma}|_{temporal} \tag{35}$$

In effect, the observed coherence is based on *target properties* and its interaction with the interferometric baseline length, i.e. the *observation geometry*. Note that these two remaining components of decorrelation are also addressed in sections 4.4.1 and 4.4.2.

4. Multitemporal InSAR Observations of Terrain

This chapter gives a review of the parameters that are observable with multitemporal InSAR, and how they are affected by target properties.

4.1. The InSAR Time-Series

Multitemporal InSAR observations are basically a time-series of measurements of the backscattered radar intensity and interferometric coherence. This multitemporal set of observations can be considered to be a time-series of single SAR acquisitions, from which appropriate InSAR image pairings are picked for InSAR-processing into interferograms and coherence images. Different targets exhibit different levels of coherence as well as different rates of coherence-loss with time and therefore the selection of suitable image-pairs for InSAR-processing depends on the application at hand. Typically InSAR-processing is performed at least for the image pairs with the shortest possible temporal baselines in the dataset. These interferograms will have the lowest possible amount of temporal decorrelation in the time-series. In addition, InSAR-processing of image pairs with longer temporal baselines may be performed as appropriate.

The InSAR time-series studied in this dissertation are multitemporal ERS-1/2 Tandem time-series. Time-series of this type were only acquired during the ERS-1/2 Tandem campaigns (the main one was conducted in 17.8.1995-1.6.1996). During this campaign the orbits of ERS-1 and ERS-2 were controlled in such a way that they imaged the same swath on the ground successively from nearly the same orbit ground track with a temporal baseline of 24 hours. During the Tandem campaigns a repeat-observation (with a 24-hour temporal baseline) was possible every 35 days giving rise to the possibility of forming InSAR-pairs with temporal baselines of multiples of 35 days. The interferometric baselines were deliberately kept short during the campaigns – in 94% of the Tandem-pairs the perpendicular baseline is less than 300m (Duchossois et al. 1996).

The ERS-1/2 Tandem-dataset is unique in the sense that it is the first set of regular (every 35 days) spaceborne InSAR observations with a short temporal baseline (one day). The great benefit of using a temporal baseline of just one day is that most natural targets (agricultural fields, boreal forests etc.) retain at least some coherence over the one-day interval. As different natural targets decorrelate at different rates, short temporal-baseline InSAR observations can be exploited in the study of such targets. Time-

series of these kinds of observations have a high potential in all InSAR-applications that suffer from high levels of decorrelation when using longer temporal baseline InSAR observations. Examples of such applications include, for example, agricultural monitoring, change-detection, forestry, glaciology, land-cover classification, and topographic mapping of vegetated areas.

While the ERS-1/2 Tandem dataset has amply demonstrated its high value in land-cover classification and vegetation mapping, it was still basically a campaign-based mission with no continuity into the future. The loss of ERS-1 in 2001 ended the possibility of conducting additional Tandem-campaigns. This lack of continuity diminished the interest of the research community to further study the gathered Tandem datasets and to discover the full potential of this type of data for land-cover and vegetation mapping.

4.2. Post-Processing of InSAR Time-Series

It is advisable to do some post-processing on the intensity and coherence images in the InSAR time-series in order to reduce the effects of noise. When working with single images spatial filtering needs to be used in noise reduction, which results in resolution loss. The situation is better when a time-series is available as then it is possible to utilise the temporal information and to use *multitemporal filtering* in order to achieve noise reduction with smaller losses in spatial resolution.

4.2.1. Spatial Filtering of Intensity Images for Speckle Reduction

As mentioned earlier, SAR images are measurements of the complex radar reflectivity of the target and the backscattered intensity I corresponds to the energy backscattered back towards the radar. Since the speckle effect (see section *2.3.2*) makes the estimates of the underlying radar reflectivity σ^0 inherently unreliable when a small number of samples/pixels are used, it is necessary to combine independent observations until the desired level of *radiometric resolution/accuracy* is reached. When N independent observations of the underlying radar backscatter are combined, the standard deviation (speckle) of the estimate is reduced by a factor of $1/\sqrt{N}$ (see equation (20)) compared with the 1-look estimate (see equation (18)). Typically the desired ENL is around 100 (Quegan and Jiong Jiong 2001) providing a factor-of-ten reduction in the standard deviation of intensity.

Quasi-simultaneous independent SAR observations are rarely available – usually only one SAR image is available and increasing *N* is only possible by trading spatial resolution for better radiometric resolution. The simplest type of spatial speckle filtering is spatial averaging, which is usually implemented with a sliding filter window. While this approach works as desired over homogeneous areas, it strongly blurs small image features like

edges or strong scatterers. A large number of more sophisticated speckle filters based on various models for speckle and the underlying radar reflectivity have been developed. These filters aim to obtain unbiased estimates of the underlying radar reflectivity, to reduce speckle as much as possible over homogeneous areas, and to preserve image features like edges. Popular spatial speckle filters include the Frost-, Kuan-, Lee- and Gamma MAP filters, among others (see for example Touzi 2002 for a review). Many of these filters achieve very high ENL over homogeneous areas which can also be realised by simple multilooking, but they preserve scene features like edges much better. For an in-depth discussion of speckle filtering, see for example Touzi 2002 or Oliver and Quegan 1998.

4.2.2. Multitemporal Filtering of Time-Series for Noise Reduction

As discussed above, a downside of using spatial-only filters in noise/speckle reduction is that these filters degrade the spatial resolution of the data. When multiple co-registered images are available over an area, an attractive way to reduce noise is to linearly combine the temporal series of images so that noise in the individual images is reduced while the spatial resolution is more or less preserved (Quegan et al. 2000; Quegan and Jiong Jiong 2001). Multitemporal filtering is an effective solution for noise reduction as it allows filtering in both the temporal- and spatial dimensions in order to achieve the desired amount of noise reduction. The following "simple" temporal filter has been proposed in Quegan et al. 2000 and Quegan and Jiong Jiong 2001:

$$I_k(x,y) = \frac{E[I_k]}{N} \sum_{i=1}^{N} \frac{I_i(x,y)}{E[I_i]}, 1 \le k \le N \tag{36}$$

where I_i are the original images, I_k are the temporally filtered images, x and y are image coordinates, N is the number of available images and $E[]$ is the expectation-value operator. Since the expectation-values are in practice estimated with spatial averaging, some loss of image resolution is unavoidable. However, the resolution-loss is clearly smaller than when using spatial-only filtering and aiming for the same amount of noise-reduction. The filter in equation (36) achieves the highest amount of noise reduction when the temporally filtered images are uncorrelated with one another. When correlated images are used the amount of noise reduction is reduced because there is less independent information available. This simple multitemporal filter is suitable for the filtering of both intensity- and coherence time-series. It should be noted that this multitemporal filter works optimally only if the underlying scene is stationary in the sense that discrete image features do not change between the images used in the temporal filter. If, for example, a land-cover change alters features in the image, the multitemporal filter produces suboptimal results in preserving spatial resolution around the changed features.

4.3. Target Properties Contributing to Observed Intensity

As discussed earlier, backscattered intensity images are maps of the radar reflectivity of the target. There are four main factors that contribute to this reflectivity and thus the backscattered intensity observed by the radar. These factors are:

- Surface Roughness
- Local incidence angle
- Dielectric constant
- Geometric properties of the target (surface/volume scattering)

4.3.1. Surface Roughness

A smooth flat surface reflects the incident radar wave specularly and unless the surface is facing towards the radar, no energy is scattered back towards the radar. Most natural surfaces are not completely smooth and therefore they scatter the incident wave diffusely in many directions, including back towards the radar. The so-called Rayleigh-criterion for surface smoothness states, somewhat arbitrarily that the surface is "smooth" if (Henderson and Lewis 1998):

$$\Delta h < \frac{\lambda}{8\cos(\theta_{i,local})} \tag{37}$$

where Δh is the height variation of the surface, λ is the wavelength and θ_i is the incidence angle. According to this criterion for ERS-1/2 a flat horizontal surface is smooth if the surface height variations are smaller than 0.77cm. Since both wavelength and the local incidence angle are included in equation (37) the same surface can appear both smooth and rough depending on the used wavelength and local incidence angle. As an approximation and within limits, increasing roughness leads to increasing backscattered intensity.

4.3.2. Local Incidence Angle

Local incidence angle has a large effect on radar backscatter. This is the effect that makes terrain-relief clearly visible on SAR imagery, unless this effect is compensated for during post-processing. Consider for example a rough surface for which the backscattering is relatively independent from the incidence angle. In this case local incidence angle affects the length of the rough surface that is enclosed within a range resolution-cell due to foreshortening (see section 2.3.5.3). As energy is backscattered from the rough surface back towards the radar, the more surface falls in a resolution-cell, the larger the backscattered intensity becomes.

4.3.3. Dielectric Constant

The dielectric constant of a material describes how the material influences the propagation of electromagnetic waves. In the microwave region the dielectric constant of most natural materials ranges between 3 and 8 when the material is dry. Liquid water, on the other hand, has a dielectric constant around 80 (Henderson and Lewis 1998). Therefore, the amount of liquid water in the target in any form (soil moisture, vegetation water content etc.) influences radar backscattering very strongly. Increasing liquid water content increases the dielectric constant and reduces the penetration of the radar wave into the target. High dielectric constant implies higher radar reflectivity and usually higher backscattered intensity. Low dielectric constant implies lower radar reflectivity, as well as deeper penetration into the target. A change in the amount of liquid water in the target caused by environmental conditions is readily visible in SAR images and their multitemporal or interferometric combinations.

4.3.4. Surface- and Volume Scattering

As discussed above, roughness, local incidence angle and the dielectric constant influence the way the radar wave interacts with the target. These parameters and the configuration of scatterers in the target determine whether backscattering happens mostly at the surface of the target (*surface scattering*), or also from inside the target (*volume scattering*). Surface scattering is the dominating scattering-type with targets into which the radar wave penetrates only a little or not at all. Examples of these kinds of targets are rock, water and most artificial targets like roads, metal roofs and buildings made from stone etc. Volume scattering takes place when the radar wave is able to penetrate into the target and scatter back from its internal structure. This is common in vegetation canopies where backscattering from multiple scatterers within the canopy, for example from stalks, branches, trunks etc. takes place. Inhomogeneities in soil properties and moisture may also cause volume scattering in soils.

Most natural targets can be modelled as an ensemble of *scattering centres* randomly positioned over the imaged surface or volume. A simple model to characterise surface scattering is the *random facet model* that approximates the surface as a series of small planar facets that are tangential to the actual scatterers (Ulaby and Dobson 1989). The backscattered signal observed by the radar is then the complex sum of the reflections from the individual facets. Similarly, scattering in vegetation can often be characterised using the water-cloud model that models the canopy as a random volume consisting of randomly positioned identical water droplets (Attema and Ulaby 1978, see also section 5.3.2.3).

4.4. Target Properties Contributing to Observed Coherence

As discussed in section 3.4.2, the observed repeat-pass interferometric coherence depends primarily on the amount of volume decorrelation and temporal decorrelation in the target.

4.4.1. Volume Decorrelation

In the presence of volume scattering the slight change in look-angle caused by the interferometric baseline causes volume decorrelation in an interferogram because the radar returns from the elementary scatterers in the volume will combine differently (with different phases) in the two interfering images. Assuming that volume scattering happens in a random volume with stable elementary scatterers distributed uniformly, the volume decorrelation for small values of Δz is (Ferretti et al. 2007):

$$\left|\gamma\right|_{volume} = 1 - \frac{\pi^2}{6}\left(\frac{\Delta z}{h_a}\right)^2 \tag{38}$$

where Δz is the thickness of the volume and h_a is the altitude of ambiguity (see equation (29)). For ERS-1/2 a 150m interferometric baseline and volume-thicknesses of 10m and 20m translate into $\left|\gamma\right|_{volume} = 0.96$ and $\left|\gamma\right|_{volume} = 0.83$, respectively. According to this model coherence-loss due to volume scattering is negligible for agricultural crops, and coherence degradation starts to get important in tall boreal forests.

4.4.2. Temporal Decorrelation

Temporal decorrelation is caused by physical changes in the target between the two interfering SAR acquisitions. The physical changes are caused either by the movement or creation/destruction of some of the elemental scatterers, or changes in the dielectric constant of the target caused for example by freezing, thawing, rain, change in soil or canopy/trunk water content etc. Movement of the elemental scatterers causes water-surfaces to decorrelate in a fraction of a second while dry rock surfaces in a desert or some artificial targets can stay coherent for years. Vegetation canopies fall between these two extremes; wind-induced movement of tree branches in the top of the canopy in a boreal forest can cause decorrelation within a matter of seconds while the more stable trunks can remain coherent for longer periods. Decorrelation caused by scatterer displacement can be modelled by displacing the elementary scatterers according to a Gaussian probability distribution (Zebker and Villasenor 1992):

$$|\gamma|_{temporal} = e^{-\frac{1}{2}\left(\frac{4\pi}{\lambda}\right)^2\left(\Delta_r^2 \sin^2\theta + \Delta_z^2 \cos^2\theta\right)} \quad (39)$$

where Δ_r^2 and Δ_z^2 are the variances of the Gaussian random motion components in range-and height directions, respectively. At the 23° look-angle of ERS-1/2 the temporal coherence is more sensitive to the vertical movement of the scatterers - just 2-3 cm of RMS motion is enough to completely decorrelate the signal at C-band. This implies that in forests even a slight wind completely decorrelates the signal from the treetops and the small branches. Therefore the observed greater-than-zero coherence of forests results from scattering from more stable parts of the forest like thicker branches, trunks or the forest floor.

4.5. Review of SAR data, InSAR-Processing, Geocoding and Post-Processing in Papers A-E

This section gives a short overview of the data processing steps performed to generate the multitemporal InSAR observations in Papers A-E.

4.5.1. Paper A

The SAR data used in this paper consisted of four ERS-1/2 Tandem image pairs acquired between late-April and mid-June in 1996 over the Flevoland agricultural area in the Netherlands. Two of the pairs were acquired from ascending and two from descending orbits.

InSAR-processing was performed with a commercial software package by Gamma Remote Sensing Research and Consulting AG. 5-look intensity images and 5-look interferograms were generated from the Tandem pairs. Common-band filtering was performed before interferogram generation to reduce baseline-decorrelation. The InSAR coherence of all the Tandem pairs was estimated using an adaptive coherence estimator that adjusted the window size between 3x3 and 9x9 pixels depending on the local coherence.

After InSAR-processing the image data acquired from ascending and descending orbit was co-registered into a single common geometry using tie-points. The Flevoland area is almost completely flat making the co-registration process straightforward. The average final co-registration error between the ascending and descending images was less than 0.5 five-look pixels.

4.5.2. Papers B-E

These four papers all use the same SAR dataset from the ERS-1/2 Tandem mission, which consist of 14 ERS-1/2 Tandem image pairs acquired between July 1995 and July 1996 over the Helsinki metropolitan area and its surroundings in Finland. All 14 image pairs were acquired from two descending orbit tracks with eight pairs acquired from the first track and six pairs from the second.

InSAR-processing was performed with a commercial software package by Gamma Remote Sensing Research and Consulting AG. InSAR processing was performed on all the Tandem pairs, and in addition 5-look interferograms and coherence images were generated from two image combinations with a longer temporal baseline (36 and 246 days). Common-band filtering was performed before interferogram generation to reduce baseline-decorrelation. Radiometrically calibrated 5-look intensity images as well as 5-look interferograms were produced from the dataset. Interferometric coherence images were computed using square and Gaussian estimator windows of different sizes (5x5, 7x7 and 9x9 pixels).

Image data acquired from the two different orbit tracks were co-registered into a common geometry using an InSAR-generated DEM. The final DEM was generated by averaging two InSAR DEMs generated from two high-coherence Tandem pairs acquired during wintertime in early 1996. A simulated SAR image derived from the DEM was used to co-register data from the two orbit tracks into a common geometry. Judging visually, data from the two different orbit tracks coincide perfectly, which shows that sub-pixel accuracy was achieved. This accurate co-registration of data from different orbit-tracks enables the use the techniques of temporal averaging over the whole set of images. After co-registration the images were orthorectified using the same DEM and final geocoding to map coordinates (UTM) was done using Ground Control Points (GCP). The final mean RMS registration error of the GCPs to map coordinates is approximately one pixel, i.e. 20 meters. The final accuracy in geocoding can be considered very good, the small geocoding errors left in the data are caused by small errors in the produced InSAR DEM.

5. Advances in Multitemporal InSAR in Land-Cover and Vegetation Mapping

This chapter reviews the published literature on the use of multitemporal InSAR for land-cover and vegetation mapping, and describes how the research in this dissertation has contributed to the field. The research has been documented in the appended papers A-E, which are also briefly summarised in this chapter. The chapter is grouped into sections, the first section covering the early research into the potential of multitemporal InSAR in land-cover and vegetation mapping, and the following sections giving a review of the land-cover classification and vegetation mapping using multitemporal InSAR data.

5.1. Early Research into Multitemporal InSAR for Land-Cover and Vegetation Mapping

The potential of C-band multitemporal InSAR for land-cover and vegetation mapping became evident soon after the launch of ERS-1 in 1991. ERS-1 acquired data from a relatively short 3-day repeat orbit (very suitable to InSAR) during mission phases A (*25.7.1991-27.12.1991*), B (*28.12.1991-01.04.1992*) and D (*23.12.1993-09.04.1994*).

The paper by Rignot and Van Zyl was one of the first to report on actual ERS-1 InSAR observations and their application to change-detection (Rignot and Van Zyl 1993). They discovered that backscattered intensity and coherence contained complementary information about changes, and that in some cases the backscatter can change by several decibels while coherence remains high (a coherent change in intensity).

Wegmüller and Werner studied the application of ERS-1 InSAR observations with 3-day, 6-day and 15-day temporal baselines for land-cover and forest mapping (Wegmüller and Werner 1995). The InSAR coherence of forest with a *closed canopy* was found to be significantly lower than that of agricultural land, urban areas and open canopies. This allowed for the separation of the dense forest class from the other land-cover classes at least up to the 15-day temporal baseline, while short temporal baselines worked the best. Winter was found to be the best period for forest-mapping. For agricultural land it was found that mechanical cultivation of the fields could be detected by the very low InSAR coherence caused by the physical disturbance of the scatterers. This paper demonstrated the potential of spaceborne C-band InSAR for land-cover and vegetation mapping, and the

authors noted that backscattered intensity and InSAR coherence are relatively independent quantities containing complementary thematic information. In addition, it was discovered that the dependence of the InSAR coherence on topography was much less pronounced than for the backscattered intensity.

Hagberg et al. studied ERS-1 InSAR observations with 3-, 6-, 9-, and 12-day temporal baselines over forested terrain and found that temporal decorrelation is in many cases the dominating factor in repeat-pass InSAR (Hagberg et al. 1995). Dense forest was found to have a lower coherence than open land for all of the studied temporal baselines. Environmental conditions (wind, temperature, rain, and snow) were found to have an effect on coherence. The authors postulated that wind is an important cause of decorrelation over forest due to wind-induced movements of the tree branches, while over agricultural land the dominant scatterers are more stable and changes in soil moisture and temperature are the main decorrelation factors.

In a later study Wegmüller and Werner studied ERS-1 InSAR observations for land-cover classification and the retrieval of vegetation parameters (Wegmüller and Werner 1997). Land-cover mapping into eight classes (including layover and shadow) was performed on one 3-day InSAR observation and a classification accuracy of around 91% was achieved in forest/non-forest classification. In a second experiment the authors studied farmland monitoring using InSAR observations with temporal baselines between 6- and 21-days. The authors noted that with the studied temporal baselines low correlation is observed over dense crops where vegetation is dominating the scattering. In addition a strong correlation was found between the InSAR coherence and the soil cover fraction for young rape seed crops. The authors postulated that ERS-1/2 Tandem InSAR observations with a 1-day temporal baseline should be “ideal” for land-cover classification.

5.2. Multitemporal InSAR in Land-Cover Classification

Land-cover classification using remote sensing imagery belongs, as a problem, in the domain of *statistical pattern recognition* (Jain et al. 2000). Land-cover classification methods can broadly be divided into *supervised* and *unsupervised* ones. The supervised methods require identification of training areas for each of the desired classes in order to train the classifier. On the other hand, unsupervised methods search for "natural" clusters in the data without the need for pre-defined training areas.

Within the context of using multitemporal InSAR data in land-cover classification the issues to be considered when setting up the classifying system include the following:

- How to combine the set of available SAR images into InSAR observations?
- What kind of post-processing should be done to the time series in order to improve classification accuracy?
- What features to select/extract from the time series?
- What classification- or segmentation-method to use?

These issues are discussed below in the light of relevant studies in land-cover classification using multitemporal InSAR. For an extensive general review of classification methods see, for example, Jain et al. 2000.

5.2.1. Combining SAR Images into InSAR Observations

In land-cover classification using multitemporal InSAR the first decision to be made is the definition of the *InSAR observations*, i.e. how the available SAR images are combined into InSAR image pairs. The orbit tracks and orbit repeat periods of the involved SAR satellites define all the potential InSAR observations over the study area, while the availability of SAR images (what was actually acquired) defines what InSAR observations are actually possible. The major limiting factor in land-cover classification with multitemporal InSAR data has so far been the lack of InSAR data with suitably short temporal baselines. This situation will improve when both of the ESA Sentinel-1 C-band SAR satellites have been launched – this two-satellite constellation is capable of multitemporal InSAR-observations with a 6-day temporal baseline.

5.2.1.1. Temporal Baseline

In practise the InSAR observations with the shortest temporal baselines made possible by the available SAR data are always generated, since these observations will have the highest InSAR coherences in the dataset. With ERS-1/2 Tandem InSAR data this implies forming Tandem InSAR pairs with a one-day temporal baseline and generating the corresponding *Tandem interferograms* and *Tandem coherence images*. ERS-1/2 Tandem

InSAR data has been used in several land-cover classification studies (for example Dammert et al. 1999; Dutra 1999; Castel et al. 2000; Strozzi et al. 2000; Weydahl 2001; Matikainen et al. 2006) including the research forming a part of this thesis (*Paper C; Paper E*). The 3-day temporal baseline ERS-1 data (from mission phases A and B) has also been used in land-cover classification studies (see Hagberg et al. 1995; Wegmüller and Werner 1995; Wegmüller and Werner 1997). This 3-day repeat data enables forming additional InSAR combinations with temporal baselines consisting of multiples of three days. Some studies have systematically produced InSAR pairs with temporal baselines from three days and upwards (Hagberg et al. 1995; Wegmüller and Werner 1995; Strozzi et al. 2000). Shorter temporal baselines generally work better in land-cover classification in the sense that the number of reliably distinguishable classes is larger.

In addition to InSAR observations with short temporal baselines some studies have also utilised InSAR combinations with longer temporal baselines such as 35 days, which is the repeat period for most of the ERS-1 and ERS-2 missions and was for the Envisat-mission until the orbit-change in October 2010. Unfortunately for land-cover classification the 35-day repeat period is far from ideal as most natural land covers suffer severe or complete decorrelation with such a long temporal baseline. InSAR pairs with very long temporal baselines up to hundreds of days or even years have been successfully utilised for the detection and monitoring of urban areas through the detection of *persistent scatterers* (*Paper C; Paper E*; Grey and Luckman 2003; Grey et al. 2003; Matikainen et al. 2006).

5.2.1.2. Interferometric Baseline

The length of the interferometric baseline affects coherence and classification of some land-cover classes through the introduction of baseline decorrelation. Common-band filtering can be used to compensate for the baseline-decorrelation for surface-like targets (see sections 3.2.1.3 and 3.4.2.3), but for targets with a scattering layer of significant thickness (for example forest or urban areas) some loss of coherence with increasing interferometric baseline is inevitable. An example of this effect is that the both the mean InSAR coherence and class separability for the urban class clearly decrease with increasing baseline length, making classification more difficult (Grey and Luckman 2003). During the ERS Tandem mission the baselines were tightly controlled so that InSAR baselines were kept relatively short during the whole mission. Therefore, with ERS-1/2 Tandem datasets baseline decorrelation is less of a problem.

5.2.1.3. Availability of InSAR Observations

The quality of the classification results depends on the number of available InSAR-observations. In general the more observations are available, the better the classification results will be, especially if the observations cover the whole year so that seasonal differences between land-cover class signatures can be exploited. Castel et al. studied how the number of ERS-

1/2 Tandem pairs used affected land-cover classification (Castel et al. 2000). With a single Tandem pair only a forest/non-forest classification was possible with an overall accuracy of 94%. With two Tandem pairs classification into five classes succeeded with a 75% overall accuracy, and the use of four Tandem pairs enabled classification into 9 classes with a 72% overall accuracy. In another study a forest/non-forest classification using one 3-day InSAR pair with a thresholding approach achieved a 91% overall accuracy (Wegmüller and Werner 1997). With the 14 ERS-1/2 Tandem pairs used in the research for this thesis, land-cover classification results with high to very high overall classification accuracies have been achieved, demonstrating the very high potential of multitemporal ERS-1/2 Tandem InSAR for land-cover classification (*Paper C; Paper E; Matikainen et al. 2006*).

5.2.2. Feature Selection/Extraction

After the InSAR observations have been made, the subsequent question is what feature-images should be selected/extracted from the multitemporal InSAR dataset. The chosen set of feature images forms the input to the following classification/segmentation step. It might be tempting to simply use all available images as inputs to the classifier, but in practise this kind of an approach is not desirable unless the total number of images is small. In fact, the classification accuracy can actually decrease if the dimensionality of the feature space gets too large (i.e. there are too many feature images), unless the number of available training samples is very large, which is rarely the case in the real world (Jain et al. 2000). In addition, the related processing-costs increase with the growing size of the feature-space. For these reasons it is desirable to keep the number of feature images as small as possible while choosing features that facilitate class-discrimination.

The term *feature-extraction* refers to deriving new features from the original feature set (Jain et al. 2000). In this context the original features are the InSAR observations, i.e. the SAR intensity images plus the coherence images created from their combinations. If the InSAR time-series is long, the dimensionality of the problem can be too high for using all the images, in which case it will be necessary to use a smaller set of features extracted from the time-series. Examples of such extracted features include *Principal Components* (PC), *maximum and minimum values*, *variability over the time-series* etc.

5.2.2.1. Post-Processing of the Image-Series

Usually the time-series of images are post-processed in order to reduce noise. Noise reduction methods based on spatial and temporal filtering are discussed in Section 4.2.

5.2.2.2. Features Derived from Single InSAR Observations

Some studies have used all the SAR intensity images in the SAR time-series as features (for example Dammert et al. 1999; Castel et al. 2000). Another approach has been to average the two intensity images in each ERS-1/2 Tandem pair to produce *Tandem intensity images*, which reduces both speckle noise and the dimensionality of the intensity-dataset (*Paper C; Paper E*; Dutra 1999; Matikainen et al. 2006). Some studies have used the ratio between two intensity images in order to highlight areas where the intensity has changed between the acquisitions (Rignot and Van Zyl 1993; Castel et al. 2000; Strozzi et al. 2000).

Various texture measures have also been used as features in land-cover classification in addition to InSAR coherence and backscattered intensity. Textural measures are computed for some small neighbourhood around each pixel, and they are a way of incorporating some contextual information into an otherwise pixel-based classification. In existing studies texture measures have usually been extracted from backscattered intensity images (Wegmüller and Werner 1997; Strozzi et al. 2000; Matikainen et al. 2006), but they have also been produced from coherence images and even from the DEM (Dutra 1999).

C-band backscattered intensity alone does not allow for the separation of very many land-cover classes, but parts of urban areas that have many artificial scatterers can be classified thanks to their high backscattered intensity and strong intensity texture. Another class that in theory could be detected from single intensity-images would be water surfaces in completely wind-free situations due to the very low backscatter, but in practise such situations are quite rare. Of course, if a large time-series is available, wind-free conditions are virtually certain to occur on some of the images, making the classification of water-bodies *opportunistic* by nature.

InSAR-coherence carries clearly more land-cover related information than backscattered intensity when the temporal baseline is short enough (*Paper C;* Srivastava et al. 2006). In general open areas exhibit high-, forests low-, and agricultural fields intermediate coherence values. Urban areas often maintain very high coherence even with long temporal baselines, unless the interferometric baseline is so long that volume scattering effects cause large amounts of decorrelation (see section 5.2.1.2).

5.2.2.3. Features Extracted from the Image-Series

The temporal dimension of an image-series contains information that is obviously not present in individual images. It is possible to tap into this temporal information by extracting features from the whole time-series, or parts of it. Such extracted features include *temporal averages, maximum & minimum values, temporal variability measures and Principal Components* (PC) derived with the *Principal Components Transformation* (PCT). Using extracted features instead of all the images in the time-series is an effective way of reducing the dimensionality of the classification-problem and thereby improving classification results.

Temporal average images are simply images that are averaged over the time-series for some period (for example the whole time-series, one year, the growing season etc.). Temporal averaging is a simple way to mitigate the effects of noise and changes caused by weather conditions or other causes (*Paper C;* Engdahl and Hyyppä 2000; Strozzi et al. 2000). The temporal average of Tandem coherence images generally exhibits low values for water, layover and forest, while agricultural fields show intermediate, and urban areas high values. On the other hand the temporal average of backscattered intensity and the texture of backscattered intensity is high for both urban and layover areas. Reliable classification between forest and agricultural land is not possible based on the temporal average of backscattered intensity alone, at least not at C-band. In general, the temporal average of Tandem coherence contains considerably more land-cover related information than the temporal average of backscattered intensity. If enough Tandem coherence images are used in the temporal average, classification into several classes (for example between agricultural/open and 1-2 forest classes) becomes possible based on the temporal average of coherence alone (*Paper C*).

Maximum and minimum values over the time-series or a part of it have been utilised as features in an InSAR land-cover classification study (see Wegmüller and Werner 1997). Also, the backscattered intensity ratio between winter and summer acquisitions has been found to be useful in detecting seasonal effects on some land-cover classes (Castel et al. 2000).

Temporal variability measures estimate the variability within the time-series. A common measure called the *Normalised Standard Deviation* is computed by dividing the standard deviation of the time-series by its temporal average (Bruzzone et al. 2004). The temporal variability of the backscatter is high over water areas due to the changing wind conditions, while the backscatter from forests generally has a low variability. In tropical forests the variability is so low that the forest is frequently used as a SAR calibration target. Agricultural fields have an intermediate level of temporal variability due to varying canopy cover during the growing season, ploughing, soil moisture differences etc.

5.2.2.4. Principal Components Transformation

Principal Components Transformation (PCT) is an *orthogonal linear transformation* that converts a multidimensional dataset onto a new coordinate system whose axes are defined by the variability in the input dataset in such a way that the greatest variance by any projection of the data comes to lie on the first coordinate (called the first Principal Component), the second greatest variance on the second coordinate (the second PC), and so on (Jolliffe 2005). The PCT transforms a set of correlated images (for example time-series of intensity or coherence images) into a new set of uncorrelated images so that most of the variability in the input dataset is contained in the first few PC-images, and the last PC-images contain mostly or only noise. These properties of the PCT make it a very useful tool in dimension-reduction and it has been successfully utilised

in land-cover classification of multitemporal InSAR-datasets (*Paper C; Paper E*; Dammert et al. 1999; Matikainen et al. 2006).

In order for the PCT to work well in dimension-reduction it is useful to *centre* the dataset by subtracting the temporal average image of the dataset from each image in the time-series before applying the PCT. Centring the datasets before applying the PCT is recommended as it enhances the detection of temporal changes in the time-series (*Paper C*).

5.2.3. Classification and Segmentation

Classification methods, both supervised and unsupervised, can be divided into *pixel-based* and *segment-based* methods. Pixel-based methods rely on the classification of single pixels based on their properties, and segment-based methods rely on first segmenting the data into *quasi-homogeneous* segments before classification of the segments based on their properties. In general pixel-based methods do not utilise information from the neighbouring pixels, except indirectly when using input images that incorporate some contextual information (for example texture measures). Segmentation can be used simply as a way of reducing noise in the dataset by grouping statistically similar nearby pixels together before using standard classification methods (see for example *Paper E*). Since the size and shape (for example the edge-smoothness) of the resulting segments can be controlled it is possible to create segments that resemble ones drawn by a human cartographer. Here the major benefit of segmentation is that these segments are created semi-automatically from the remotely sensed data itself. In more advanced segmentation-methods the segmentation/classification algorithm can increase classification accuracy by taking into account the classes of the neighbouring segments and thereby utilising the contextual info explicitly (see for example Matikainen et al. 2006).

5.2.3.1. Thresholding, Hierarchical Classification and Maximum Likelihood Classification

The simplest supervised classification method is called *thresholding*, in which land-cover classes are determined by setting suitable threshold-values on the input feature images, with different classes residing above and below the threshold. For example, urban areas can be detected (as areas with the highest coherence) simply by setting a suitably high threshold-value on coherence images with a long temporal baseline (Grey and Luckman 2003). Thresholding has also been utilised in other land-cover classification studies for the classification of all classes (Rignot and Van Zyl 1993; Wegmüller and Werner 1997; Strozzi et al. 2000), or for detecting the water-class by thresholding backscattered intensity ratios (*Paper C*; Engdahl and Hyyppä 2000; Matikainen et al. 2006). Several threshold-evaluations can be joined together into a *decision-tree* creating a *hierarchical classification system*.

Maximum Likelihood Classification (MLC) is a very popular supervised classification method that usually assumes that the input data is normally distributed, which is almost never true in practise. The training areas are used to teach the classifier what the means and covariances of the defined classes in the classified dataset are– the MLC can then assign every pixel/segment in the dataset into the class where it most likely belongs. MLC has been utilised in several land-cover classification studies with multitemporal InSAR data (see for example Dutra 1999; Castel et al. 2000; Strozzi et al. 2000).

5.2.3.2. Other Classification Methods

Neural networks have been successfully used in land-cover classification as well; many of these methods have the advantage that they do not assume that the input dataset is normally distributed. Dutra compared supervised land-cover classification methods on one ERS-1/2 Tandem pair and an additional ERS-2 image using MLC, *fuzzy ARTMAP and multilayer-perceptron* classifiers (Dutra 1999). The multilayer-perceptron was found to perform slightly better than either MLC or the fuzzy ARTMAP-classifier, but in general the differences between the classifiers were rather small. Good land-cover classification results using *Radial Basis Function* neural networks have been reported in Bruzzone et al. 2004.

The *ISODATA-algorithm* (also called the c-means algorithm) is a popular iterative unsupervised classifier that looks for "natural" clusters in the data (Tou and Gonzalez 1974). A drawback of the standard algorithm is that it assigns observations to the cluster/class with the nearest mean value, which signifies that the clusters are assumed to be spherical. ISODATA has been successfully used in land-cover classification of multitemporal InSAR data in *Paper C*.

5.2.3.3. Segmentation Methods

Fuzzy Clustering Segmentation (FCS) has been studied as a method for the automatic segmentation and classification of multitemporal InSAR data (Dammert et al. 1999; Strozzi et al. 2000). A drawback of FCS is that it is a computationally intensive method even though the results were not significantly better when compared against thresholding and MLC on the same dataset (Strozzi et al. 2000).

In *Paper E* the temporal average of Tandem coherence was segmented using a *multi-resolution segmentation* algorithm followed by classification with a *Nearest Neighbour* (NN) classifier. Segmentation of a low-noise single-channel dataset like the mean Tandem InSAR coherence is a straightforward procedure with any segmentation method.

When contextual information based on the classes of neighbouring segments is taken into account, the improvement on pixel-based classification is potentially large, especially for classes that are very heterogeneous like the urban-class. This was demonstrated in Matikainen et al. 2006, where a significant improvement on the overall classification

accuracy (from 90% to 97%) was achieved over an earlier study that used the same InSAR dataset but relied on pixel-based classification (*Paper C*).

5.2.4. Presentation of Paper C and Paper E

Papers *C* and *E* both deal with land-cover classification with multitemporal ERS-1/2 Tandem InSAR data. The InSAR dataset is identical in both cases and consists of 14 Tandem image pairs acquired over Helsinki and its surroundings in Southern Finland between the summers of 1995 and 1996. The InSAR dataset and its processing are described in section 4.5.2.

Paper C is a "pure" land-cover classification study while *Paper E* discusses combining segment-based land-cover classification with a subsequent boreal forest stem volume estimation step. For *Paper E* the land-cover classification content is described here, while the content related to stem volume retrieval issues is discussed in section 5.3.4.5.

5.2.4.1. Paper C

This paper deals with land-cover classification of multitemporal ERS-1/2 InSAR data on a 2500km^2 test site in the Helsinki metropolitan area in Finland. A novel two-stage hybrid classifier was developed and its performance in land-cover classification was assessed using high quality reference data gathered specifically for this study. The reference data consisted of high-resolution orthophotos, oblique aerial images, national base maps and stem volume data from the *National Forest Inventory* of Finland (NFI). These reference data sources were used to identify reference points for the eight reference land-cover classes (water, agricultural/open, dense forest, sparse forest, low residential, high residential, industrial buildings, dense urban).

After InSAR processing the dimensionality of the image dataset was large (28 intensity images, 14 Tandem coherence images, 2 coherence images with long temporal baselines), and reducing the dimensionality of the dataset was necessary before the land-cover classification step. First the two intensity images in each InSAR pair were averaged to Tandem intensity images in order to reduce the number of intensity images from 28 to 14. Principal Components Transformation (PCT) was then used to reduce data dimensionality further. PCT was applied separately to both the Tandem intensity and Tandem coherence images time-series. Two important pre-processing steps were performed on the time-series before running the PCT:

1. Centring the time-series by subtracting the temporal average image (mean over the time-series) from the time-series.
2. Water-masking.

The first pre-processing step reduces the correlations between the images fed to the PCT, and enhances the capability of the PCT to highlight

changes from the average value of the time-series, as otherwise the first PC would simply reproduce the temporal average image. The second pre-processing step was performed in order to enhance the ability of the PCT to highlight differences over land. The water-mask was constructed by thresholding the ratio of intensity images acquired in calm and windy conditions. Without water-masking the first PC of both intensity and Tandem coherence time-series would highlight the water areas as differing wind conditions cause very large differences in backscattered intensity, and open water and sea ice also have very different InSAR coherence. Water-masking is also the first classification step of the developed *hybrid classifier*, the remaining classes were classified using the ISODATA algorithm after the PCT. The first two PCs explained 50% of the total variation in the intensity time-series and 43% in the coherence time-series. After the PCT the following six images were chosen, on the basis of apparent land-cover related informational content, as input-features to the classification step:

1. Temporal average of the intensity time-series;
2. First PC of the intensity time-series;
3. Temporal average of the Tandem coherence time-series;
4. First PC of the Tandem coherence time-series;
5. Second PC of the Tandem coherence time-series;
6. Average of the two coherence images with long temporal baselines (36 and 246 days).

These images were inputs to the ISODATA algorithm that is an unsupervised technique searching for "natural" clusters in the data. The ISODATA classification could not satisfactorily differentiate between the "high residential", "low residential" and "industrial buildings" – classes as defined in the reference data. These classes were therefore combined into a "mixed urban" – class, which covers both residential and urban areas. This brought the number of distinguishable classes down to the following six: "water", "agricultural/open", "dense forest", "sparse forest", "mixed urban" and "dense urban". The accuracy of land-cover classification into these six classes was assessed by comparing the classification results against the reference data. The overall classification accuracy and average producer's accuracy were both found to be 90%, while the average user's accuracy was 83%. The classification result is illustrated in Figure 11.

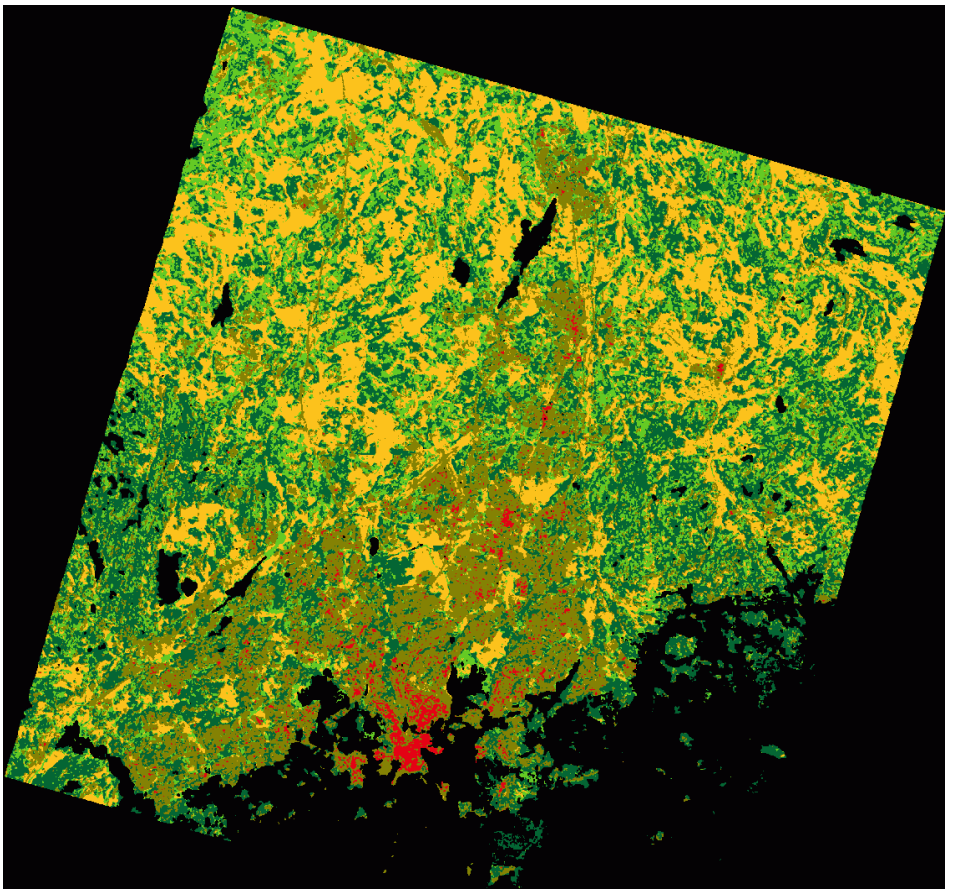

Figure 11. Classification results over the Helsinki metropolitan area. Classes: Black – Water; Yellow – Agricultural/Open; Dark Green – Dense Forest; Light Green – Sparse Forest; Bronze – Mixed Urban; Red – Dense Urban.

After running the ISODATA-classification it is instructive to examine how the pixel values of the formed classes are distributed in the six input feature-images to gain understanding of class differences. Figure 12 shows the distributions of the pixel values for the five ISODATA-classified classes. The figure demonstrates that it was possible to extract complementary information, in the land-cover classification sense, from the InSAR coherence and SAR intensity time-series. It is also clear that multitemporal InSAR coherence allows the discrimination of many more classes than multitemporal SAR intensity does. For example, the temporal average of intensity only allows for a reliable discrimination between “dense urban” and the three non-urban classes, and the first PC of intensity only reliably discriminates between “agricultural/open” and the rest of the classes. All other discriminations between classes were made possible by the use of coherence information.

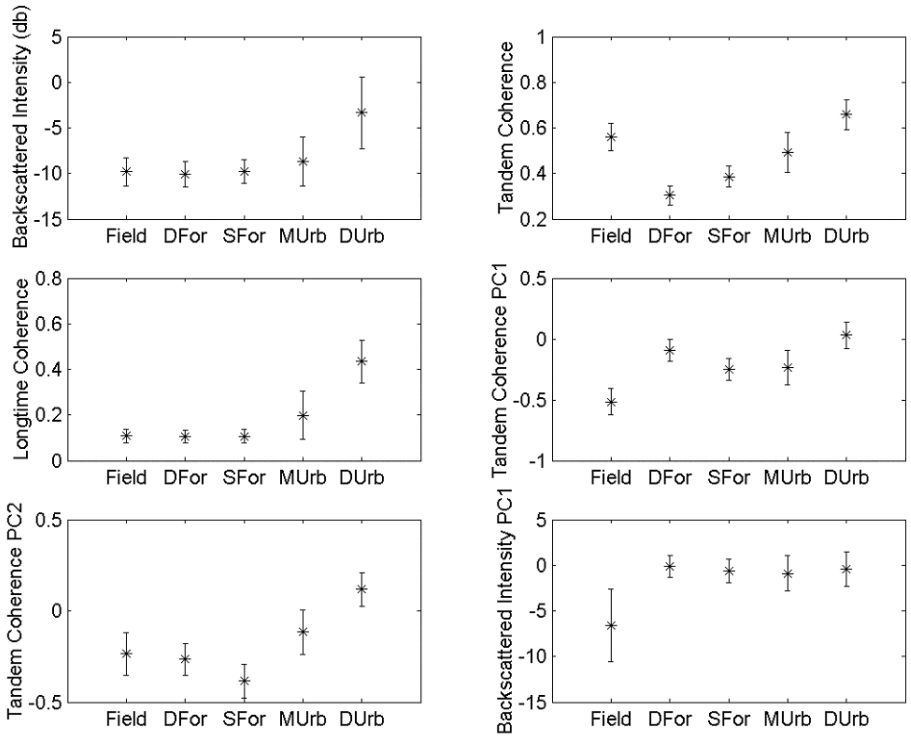

Figure 12. Distributions of the pixel values for different classes in the dataset fed to ISODATA. +/- 1 standard deviation is indicated with an error bar.

The classification performance (number of discriminated classes & classification accuracy) is markedly higher than in several previous studies utilizing ERS-1/2 Tandem InSAR data for land-cover classification (see for example Dammert et al. 1999; Dutra 1999; Castel et al. 2000; Strozzi et al. 2000; Weydahl 2001). The possible reasons to explain the better results in this study are, in no particular order:

- Use of a large multitemporal InSAR dataset of 14 Tandem pairs
- The high-accuracy orthorectification of the SAR data
- The high-quality reference data gathered specifically for the study
- The use of the two-stage hybrid classifier that classified the "water"-class separately from the classes on land
- The pre-processing steps performed before applying the PCT
    - Centring the data by subtracting the temporal average
    - Water-masking

This study suggests that multitemporal ERS-1/2 Tandem InSAR data has a very high potential for land-cover classification and that InSAR coherence carries clearly more land-cover related information than the backscattered intensity.

5.2.4.2. Paper E (Land-cover classification content)

Note: This paper deals with segmentation-based land-cover classification that is followed by boreal forest stem-volume retrieval. This section deals with the land-cover aspects of the Paper while stem volume retrieval is discussed in section 5.3.4.5.3.

In this study a novel segment-based method was developed for the combined land-cover classification and boreal forest stem-volume estimation based on multitemporal ERS-1/2 Tandem InSAR data. The study was conducted on a 366km^2 area in Southern Finland covering the Tuusula boreal forest test site. The reference data consisted of high-resolution orthophotos, oblique aerial images, national base maps and stem volume data from the National Forest Inventory (NFI) of Finland.

The combined land-cover classification and stem volume estimation method developed in this study has three steps:

1. Segmentation of the study area into quasi-homogenous segments based on the temporal average of InSAR coherence.
2. Classification of the segments into forest and other land-cover classes based on the multitemporal InSAR signatures of the segments.
3. Estimation of forest stem volume for all forest segments (*this step is presented in section 5.3.4.5.3*).

In Step 1 the temporal average of ERS-1/2 Tandem coherence was segmented into quasi-homogenous segments. Choosing the mean Tandem coherence image as the basis of segmentation is a natural choice in the sense that it was evidently sensitive to vegetation density. Segmentation of a low-noise single-channel dataset like the mean Tandem InSAR coherence is a straightforward procedure. In this study segmentation was performed with the commercial software package *eCognition* that employs a multi-resolution segmentation algorithm in which the resulting segment size, homogeneity and boundary smoothness can be controlled by the user (Baatz and Schäpe 2000). A total of 4806 segments with an average size of 7.6 hectares were created on the 366km^2 test area.

In Step 2 the created segments were classified into four land-cover classes (“forest”, “water”, “agricultural/open” and “urban”) with eCognition. In the supervised classification step a human operator chose a few training segments for each of the classes, and eCognition performed a *Nearest-Neighbour* (NN) classification of all the segments based on the mean segment value of the following input-features:

1. Temporal average of the intensity time-series;
2. First PC of the intensity time-series;
3. Temporal average of the Tandem coherence time-series;

4. First PC of the Tandem coherence time-series;
5. Second PC of the Tandem coherence time-series;
6. Average of the two coherence images with long temporal baselines (36 and 246 days).

Of the total number of 4806 segments, 4176 were classified into the forest class. Figure 13 displays the combined land-cover and stem volume estimation map. The accuracy of the land-cover classification was not assessed in this study, but using the same InSAR dataset an overall classification accuracy of 90% into six land-cover classes was achieved with an unsupervised pixel-based approach (*Paper C*), and with a segmentation-based supervised classification approach the overall classification accuracy rose to 97% (Matikainen et al. 2006). If only forest/non-forest classification of the segments is desired (sufficient for stem volume retrieval purposes), simply using the mean Tandem coherence for segment classification should be sufficient as forest segments exhibit markedly lower Tandem coherence than urban or agricultural/open segments.

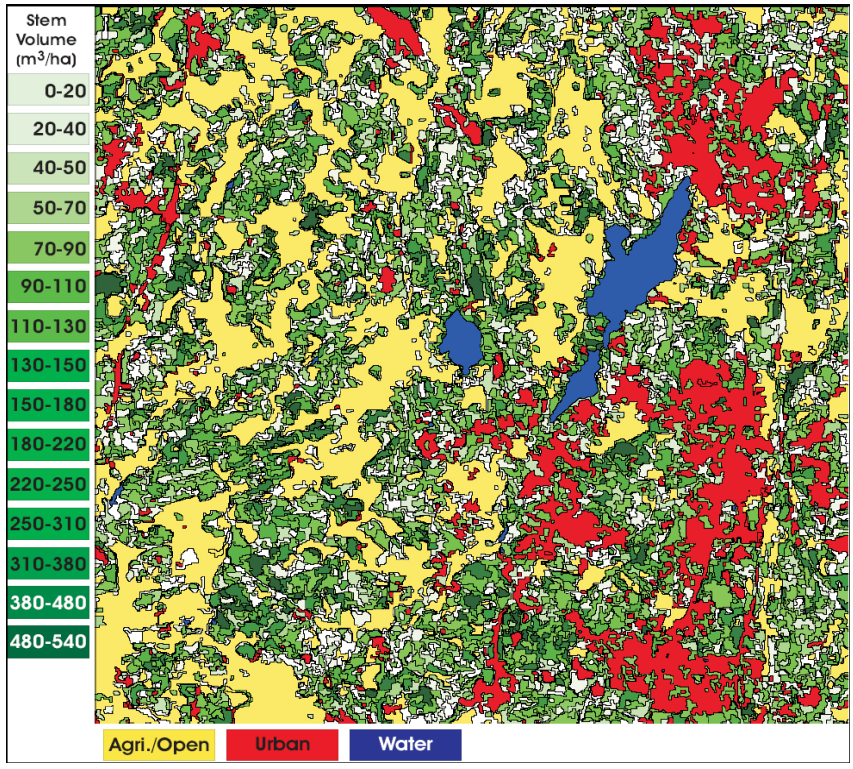

Figure 13. Combined land-cover classification and stem volume map. Shades of green indicate stem volume of forest segments, other colours indicate non-forest land-cover classes (see legend).

5.2.5. Discussion

The studies into land-cover classification with C-band repeat-pass InSAR data clearly demonstrate that short temporal baseline interferometric coherence carries information about the land-cover that is complementary to the information contained in the intensity images. The studies also strongly suggest that ERS-1/2 Tandem coherence carries greatly more land-cover related information than intensity does – this is evident already with single InSAR observations and becomes even clearer when the temporal averages of intensity and coherence are compared, or when the information-content in the coherence and intensity time-series is assessed (*Paper C*). Shorter temporal baselines – at least down to the 24 hours in the ERS-1/2 Tandem datasets – usually enable better discrimination between a larger number of land-cover classes.

The progress in land-cover classification using multitemporal InSAR data has been hindered by the lack of available data with suitably short temporal baselines. As is usually the case with multitemporal datasets, the availability of a longer time-series makes higher classification accuracies possible. Dammert et al. studied land-cover classification using an unsupervised segmentation method on three Tandem pairs and achieved overall classification accuracies between 65% and 75% (depending on the number of classes), and a 92.6% accuracy in simple land/water classification. According to the authors these numbers should be taken as lower limits to the true classification accuracy due to problems with the registration of the reference land-map (Dammert et al. 1999). More Tandem pairs were available for Strozzi et al. who studied land-cover classification on two test sites in Switzerland (with 8 and 5 Tandem observations) and Finland (with 6 Tandem observations) (Strozzi et al. 2000). The overall accuracy on forest/non-forest classification varied between 78% and 89% depending on site characteristics, input images used, and the classification method used. Land-cover classification accuracy into four classes (forest, field, urban, water) achieved an overall accuracy of around 75%. Engdahl and Hyyppä studied land cover classification using a ERS-1/2 Tandem dataset consisting of 14 pairs covering a full year, and achieved an overall classification accuracy of 90% into six classes (water, fields, dense forest, sparse forest, mixed urban, dense urban) using a novel two-stage hybrid classifier (see *Paper C* and the discussion in section 5.2.4.1). Matikainen et al. studied land-cover classification on the very same Tandem dataset with an emphasis on mapping built-up areas (Matikainen et al. 2006). They used an advanced classification method based on multi-resolution segmentation utilising contextual information about the classes of the neighbouring segments. A very high overall classification accuracy of 97% was achieved in a land-cover classification into seven classes (open area, sparse forest, dense forest, low rise residential, high-rise residential, dense urban and industrial area) further demonstrating the very high potential of multitemporal ERS-1/2 Tandem InSAR data in land-cover classification.

In the future the launch of the ESA Sentinel-1 (S-1) constellation will make a large impact on land-cover classification using multitemporal InSAR data. It is expected that the 12-day and especially 6-day InSAR coherence images produced by the S-1 system will prove to be highly useful for the classification of vegetated land-cover classes.

5.3. Multitemporal InSAR in Vegetation Mapping

As discussed in section 5.2, multitemporal repeat-pass InSAR data is very suitable for mapping the location of vegetated areas through land-cover classification of the InSAR time-series. In this chapter we delve further into vegetation mapping by looking into the retrieval of specific *vegetation parameters* from multitemporal InSAR data. The specific parameters addressed in this thesis are the retrieval of *agricultural crop height* and *boreal forest stem volume*.

So far the progress in vegetation parameter retrieval from multitemporal InSAR data has been seriously hampered by the lack of available data with suitably short temporal baselines. Vegetated areas lose coherence rather rapidly via temporal decorrelation (see section 4.4.2), the amount of which depends on the wavelength used, temporal baseline, vegetation type and the environmental conditions. At C-band nearly complete loss of coherence can take place already in a few days, while in favourable conditions some degree of coherence can be retained even for a couple of weeks.

5.3.1. InSAR Observations in Vegetation Mapping

A repeat-pass InSAR observation consists of four observables: the backscattered intensities of the two images in the InSAR image pair, the corresponding InSAR coherence, and the corresponding interferometric phase (see section 4.1).

5.3.1.1. Intensity

As discussed in section 0, several target properties affect the backscattered intensity. The observed backscattered intensity from agricultural fields is strongly influenced by dielectric changes caused by changes in the liquid water content of the soil and canopy (Ulaby 1975; Saich and Borgeaud 2000). The same is true in boreal forests, and rather large changes in forest backscatter are observed with changes in soil and canopy water content. In general the water content is influenced by environmental conditions like rainfall, insolation, presence of snowpack, wind and freezing/thawing events etc. In agricultural monitoring the backscattered intensity is also heavily affected by farming practises that alter soil roughness - for instance tillaging the field. These weather- and soil-related effects complicate, and in

many cases even prevent the use of the backscattered intensity alone for reliable vegetation parameter retrieval.

5.3.1.2. Coherence

As discussed in section 4.4, the primary causes of coherence degradation are volume decorrelation and temporal decorrelation. InSAR coherence is extremely sensitive to changes in the configuration of scatterers, which is a direct cause of temporal decorrelation. Vegetation canopies can decorrelate in seconds due to the movement of scatterers in the canopy, the amount of which depends on the parameters of the vegetation canopy (height, stiffness of the canopy constituents) and prevailing environmental conditions (wind, rain, presence of snowpack etc.). An extreme case of temporal decorrelation takes place during the tillage of agricultural fields between the InSAR acquisitions, which causes complete decorrelation through the disturbance of practically all of the scatterers in the field. In addition to temporal decorrelation, InSAR coherence is decreased by volume decorrelation that is caused by the scatterers being at different heights in the canopy volume, and therefore contributing less coherently into the complex correlation in InSAR coherence (Treuhaft et al. 1996; Treuhaft and Siqueira 2000). Volume scattering is practically negligible for agricultural crops at C-band at the usual baseline lengths for ERS- and Envisat missions, but it can play a role in forests (see equation (38) in section 4.4.1), depending on the baseline.

5.3.1.3. Phase

Since the top of the forest canopy is at different height than the forest floor, the InSAR imaging geometry causes the scattering contributions from these two targets to have different InSAR phases, provided that the InSAR baseline is nonzero. This opens up the possibility of detecting forest height directly in locations where an abrupt transition from a forest stand to open land takes place (Hagberg et al. 1995). However, later research has demonstrated that this method for tree height determination using multitemporal InSAR is in practise too unreliable due to phase noise and atmospheric artefacts (Santoro et al. 2005). Single-pass InSAR suffers neither from temporal decorrelation nor atmospheric artefacts, which makes it better suited for the retrieval of canopy heights. DEMs produced by the single-pass SRTM have been shown to contain a significant signal related to forest canopy-height, which can be exploited for canopy-height mapping (Kellndorfer et al. 2004; Walker et al. 2007).

5.3.1.4. InSAR Complementarities

When both intensity and coherence are considered together it is possible to infer things about vegetated surfaces that cannot be deduced by considering intensity or coherence alone. For example, a *coherent intensity-change* (high coherence despite a change in intensity) implies that a dielectric change has taken place while the scatterer configuration remained unchanged. These kinds of effects have been observed on melting snow

packs (see *Paper B*). On the other hand, stable intensity with a loss of coherence implies that the scatterer configuration has changed, while the dielectric properties have stayed roughly the same. This can happen on agricultural fields for example due to ploughing, which destroys coherence completely and is therefore easily detectable on Tandem coherence images.

5.3.2. Vegetation Modelling

Microwave backscatter from vegetation is affected by the structure of the observed vegetation canopy, its dielectric properties (water content), and the roughness, moisture, and internal structure of the underlying soil. *Forward models* predict the radar observations given the properties of the vegetation canopy and the underlying soil. Models that simulate both the intensity and phase of the radar return are called *coherent models*, while *incoherent models* are used when incoherent modelling of the backscattered intensity alone is sufficient.

Vegetation canopies can have very complex structures from a scattering point-of-view and the models used vary from simple ones like the *Water Cloud Model* (see section 5.3.2.3) to ones that take the complex geometry of the scattering elements in the canopy into account. Unless purely empirical/statistical approaches like *regression* are used, the parameters of interest are in most cases derived from the sensor observables through an *inversion* of an appropriate forward model of the scene (Lopez-Sanchez and Ballester-Berman 2009). Therefore, the forward model must be both *robust* and *simple* enough to guarantee a successful inversion. Due to the rather small number of observables available via SAR observations the number of free parameters in the model must be kept small as well; otherwise the inversion-problem becomes underdetermined and simplifying assumptions or *a priori* - information are required in order to get unambiguous inversion results.

5.3.2.1. Early Models

The early vegetation models were very simple and consisted for instance of a reflective ground-layer and a vegetation canopy modelled as a homogeneous dielectric slab (Bush and Ulaby 1976), or as a "water-cloud" consisting of randomly positioned water droplets (Attema and Ulaby 1978). Some more complex models describe the canopy as a collection of simple dielectric scattering elements. An example of such a model is the *Michigan Microwave Canopy Scattering Model* (MIMICS) that models the canopy as a collection of trees consisting of cylinders and disks, the ground as a rough surface, and the scattering is simulated by solving the radiative transfer equation (Ulaby et al. 1990). When MIMICS is used in forests the canopy is usually divided into a crown layer, a trunk layer and an underlying rough ground layer. MIMICS can simulate 1st and higher-order scattering terms and deal with both open and closed canopies.

5.3.2.2. Coherent Models for InSAR and Pol-InSAR

In coherent models the radar return is modelled as a coherent sum of returns from the individual scatterers (see for example Rodriguez and Martin 1992; Treuhaft et al. 1996; Bamler and Hartl 1998). These forward models describe the interferometric observations (phase, coherence, backscattered intensity) given parameters that describe the vegetation and the underlying surface. In simpler coherent models the vegetation is described as a single homogeneous random layer (for example in Treuhaft et al. 1996.) while in more complex models the vegetation-layer can be described in a more complicated way, for example as a collection of dielectric cylinders and elliptical disks (see for example Marliani et al. 2002). InSAR is more sensitive to the location and distribution of scatterers while *Polarimetric SAR* (POLSAR) is more sensitive to scatterer orientation (Treuhaft and Siqueira 2000). These two modes of SAR observations are exploited simultaneously in *Polarimetric SAR-Interferometry* (Pol-InSAR) (Cloude and Papathanassiou 1998; Treuhaft and Cloude 1999; Papathanassiou and Cloude 2001). Special models have been developed for Pol-InSAR applications; for example the so-called *Random Volume over Ground* (RVoG) models treat the vegetation-layer as consisting of randomly positioned randomly oriented scatterers (Papathanassiou and Cloude 2001). The RVoG-models are well adapted to the randomness of vegetation in most forest covers, but in many agricultural crops the morphology of the plants is dominated by the vertical stems, a situation which is better covered by *Oriented Volume over Ground* (OVoG) – models (see for example Lopez-Sanchez and Ballester-Berman 2009). These types of models can also be combined into a two-layered vegetation model where an RVoG-layer is set on top of an OVoG-layer describing the stem/stalks.

5.3.2.3. Water-Cloud Models

The so-called *Water Cloud Models* (WCM) are simple models based on radiative transfer modelling that treat the vegetation as a "water-cloud" consisting of randomly positioned identical water droplets forming a *statistically homogeneous* canopy (Attema and Ulaby 1978). The individual droplets both backscatter and attenuate the incident radar wave, and the total contribution from vegetation is computed as an *incoherent sum* of the individual returns. In other words the simplest WCM:s are incoherent. At C-band only single scattering is usually considered, i.e. direct returns from inside the canopy, and direct returns from the ground that are being attenuated by the canopy. The input parameters of the WCM are plant height, plant moisture content and soil moisture content. The model provides an estimate of the relative soil and vegetation contributions to the observed radar backscatter, as well as an estimate for the attenuation taking place in the vegetation layer.

The so-called *Interferometric Water Cloud Model* (IWCM) is a coherent extension of the WCM for the modelling of forest InSAR coherence (Askne et al. 1997; Santoro et al. 2002; Askne et al. 2003; Askne and Santoro 2005). In this model the forest coherence depends on the coherence of the

forest floor, temporal coherence of the vegetation and volume scattering effects caused by the InSAR geometry (baseline length).

5.3.2.4. The HUT Model

The *Helsinki University of Technology* (HUT) semi-empirical backscattering-coherence model is a simple incoherent WCM based on 1st order radiative transfer modelling. The model has two layers - the ground layer and the forest canopy layer - and it ignores higher-order scattering terms like the trunk-ground interaction. The HUT model consists of two parts - a semi-empirical boreal forest backscattering model that can distinguish between the radar returns from the ground layer and from the forest canopy. The second part of the model is an empirical coherence model in which the boreal forest coherence is modelled to depend linearly on the coherences of the ground layer and the forest canopy, and the total amount of backscatter coming from each.

The backscattering-part of the HUT model was developed based on empirical measurements of boreal forest backscatter conducted with the airborne *ranging scatterometer* HUTSCAT that allows one to distinguish what part of the total backscatter is coming from the forest canopy and what is being returned from the ground layer (Pulliainen et al. 1994; Pulliainen et al. 1996; Koskinen et al. 1999; Pulliainen et al. 1999). The HUT model takes into account the effects of vegetation water content, top-soil moisture and the effective surface roughness, and it models the radar backscatter as a function of forest stem volume. The forest backscatter is modelled as a sum of two contributions, one from the forest canopy and one from the ground layer that is attenuated by the canopy:

$$\begin{aligned} \sigma^0_{forest} &= \sigma^0_{canopy} + t^2 \sigma^0_{ground} \\ &\equiv \sigma^0_{canopy} + \sigma^0_{floor} \end{aligned} \tag{40}$$

where t^2 is the two-way canopy transmissivity (see Figure 14).

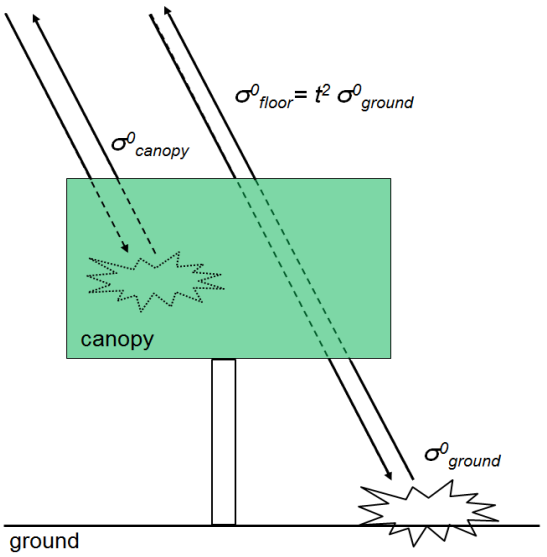

Figure 14. HUT backscattering model for forest. The forest backscatter is modelled as consisting of the sum of direct canopy backscatter and direct ground backscatter that has been attenuated by the canopy.

The canopy backscattering and the canopy transmissivity depend on stem volume, incidence angle and the effective volumetric water content of the canopy. The ground backscatter depends on volumetric soil moisture, temperature and the soil type. Trunk-ground interactions have been ignored as negligible, which is justified at C-band by the attenuation in the canopy, as well as by the roughness of typical forest floor that reduces specular reflections from the ground-layer (Pulliainen et al. 1994; Pulliainen et al. 1999). All these effects are captured into two empirical parameters in the following fashion:

$$\begin{aligned}\sigma^0_{forest} &= 0.131 \cdot a \cos\theta \left[1 - e^{-5.12\cdot 10^{-3}\frac{aV}{\cos\theta}}\right] + b \cdot e^{-5.12\cdot 10^{-3}\frac{aV}{\cos\theta}} \\ &\equiv \sigma^0_{canopy} + \sigma^0_{floor}\end{aligned} \tag{41}$$

where V is stem volume, θ is the incidence angle and a and b are empirical parameters that are related to the *volumetric vegetation water content* and the *backscattering-coefficient of the ground*, respectively (see *Paper B* for details). The values of these empirical parameters are determined by fitting the HUT intensity-model (40) into training data consisting of training forest stands with known stem volumes and backscattering coefficients.

The sensitivity of radar backscatter to forest stem volume at C- and X-bands is not very high and the correlation between stem volume and forest backscatter varies from positive to negative depending on soil and canopy

moisture (Pulliainen et al. 1994). In fact, the effects of soil moisture variation and stem volume on total forest backscatter are of the same magnitude, both typically less than 2dB at C-band. Even though the fluctuations of stand-wise observations are high, the average level of backscatter for different stem volume classes is well described by this model (Pulliainen et al. 1996). The effect of forest backscatter fluctuations can be mitigated by aggregating the observations to larger forest stand size – on 20 ha stands the retrieval accuracy is already quite good (Pulliainen et al. 1999).

In the coherence-part of the HUT model InSAR coherence is modelled to depend linearly on the amount of scattering coming from the canopy, which is a good approximation at least when baselines are rather short (Koskinen et al. 2001):

$$\begin{aligned} \left|\bar{\gamma}_{forest}\right| &= \left|\bar{\gamma}_{ground}\right| + \left(\left|\bar{\gamma}_{canopy}\right| - \left|\bar{\gamma}_{ground}\right|\right) \cdot \frac{\sigma^0_{canopy}}{\sigma^0_{forest}} \\ &\equiv a_0 + a_1 \cdot \left(\frac{\sigma^0_{canopy}}{\sigma^0_{forest}}\right) \end{aligned} \tag{42}$$

where a_0 and a_1 are empirical parameters corresponding to the *coherence level of open areas* (stem volume ~zero) and the *Interferometric Coherence-Contrast* (ICC) between open areas and very dense forests (see *Paper D*). The values of these empirical parameters are determined by fitting the model (42) into training data, i.e. the known coherences of and stem volumes of training forest stands. The empirical coherence model is then inverted through a three-step minimisation procedure described in *Paper B*. At the end of the inversion-process stem volume can be retrieved for any forested pixel/segment in the dataset. Despite its simplicity the HUT model has demonstrated good stem volume retrieval performance on multitemporal ERS-1/2 Tandem datasets (*Paper B, Paper E*).

5.3.3. Crop-Height Retrieval over Agricultural Land

5.3.3.1. InSAR Retrieval Techniques

As discussed earlier, numerous factors influence backscattered intensity from vegetation. In the case of agricultural crops the situation is made more complex by the usually very strong ground/soil component, especially with steep incidence angles like the 23° used by the ERS-satellites. In general relating backscattered intensity to crop height is very difficult or impossible due to these complicated effects.

Interferometric coherence is sensitive to the vegetation type and height, and as discussed earlier, it is less sensitive to factors like soil & vegetation moisture, soil roughness etc. Volume decorrelation over agricultural crops at C-band can be considered to be almost negligible, unless the

interferometric baselines get very long (see section 4.4.1). On the other hand the temporal decorrelation (see section 4.4.2) tends to be high on agricultural fields due to the rather rapid temporal changes taking place. Causes of these changes include: crop growth, crop movement, soil roughness changes due to wind/rain, dielectric changes due to canopy water content or soil moisture changes. Ploughing generally destroys coherence due to the disturbance of practically all the scatterers in a field.

If suitable Pol-InSAR data is available, crop heights can be retrieved via inversion of RVoG or OVoG models (see preceding section), provided that the interferometric baseline is suitably long for the used wavelength (Lopez-Sanchez and Ballester-Berman 2009). For the Pol-InSAR techniques to work the amount of temporal decorrelation needs to be very small and therefore in practise single-pass data is needed.

With repeat-pass InSAR data it is possible to exploit the information-content in the coherence, provided that the temporal baseline is short enough so that the coherence-signal caused by differing vegetation-heights is not lost due to temporal decorrelation. From a purely empirical standpoint one can assume that higher/denser crops lead to lower coherence values quicker as the coherence of the moving & growing vegetation canopy is bound to be lower than the coherence of the relatively stable soil. The simplest methods relating InSAR coherence to agricultural crop height are based on regression.

5.3.3.2. Presentation of Paper A

In this paper, the relationship between ERS-1/2 Tandem interferometric coherence and the crop heights of sugar beet, potato and winter wheat were investigated. The study was conducted on the well-known Flevoland test-site in the Netherlands. The processing-steps performed on the SAR data are described in section 4.5.1.

The data used in this study consisted of four ERS-1/2 Tandem pairs acquired during the early growing season of 1996, and in situ crop height measurements of sugar beet, potato and winter wheat from the same period of the 1993 growing season. The lack of contemporary observations on InSAR coherence and crop heights is a drawback of the study, but the similarity of the 1993 and 1996 early growing seasons can be argued based on the similarity of the backscattered intensity signatures of all the studied crops during these two years. Both the crop InSAR coherences and heights were found to develop approximately linearly during the early growing season with coherences declining as the crop heights increase. Figure 15 illustrates how the Tandem coherence and crop height developed for potato. Linear fits to the Tandem coherence and crop height data are also shown. Similar line fits were performed for the sugar beet and potato datasets. These line fits made it possible to derive linear relationships between Tandem InSAR coherence and crop height that are illustrated in Figure 16.

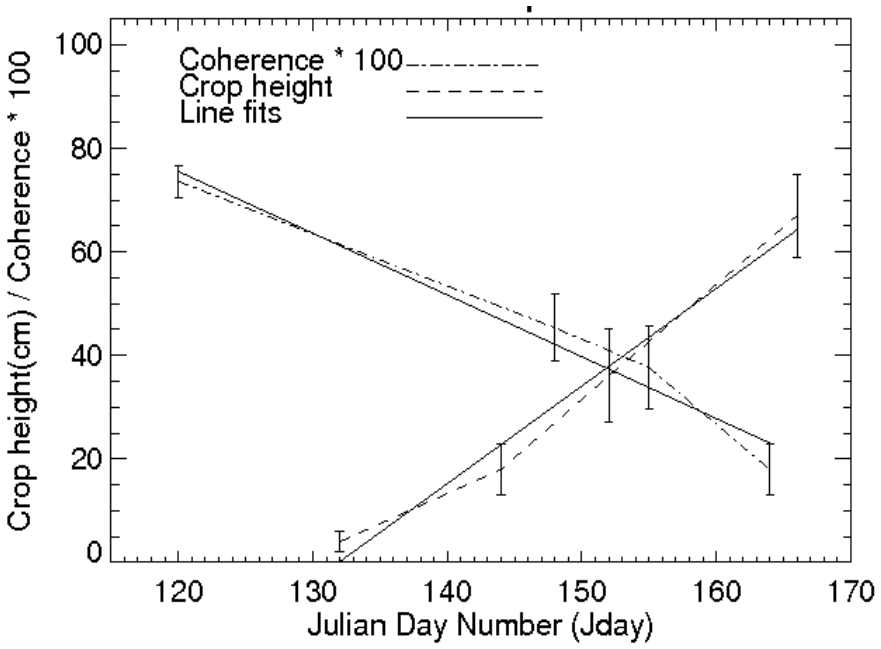

Figure 15. Line fits to Tandem coherence and crop height data for potato. The error-bars represent +/- one standard deviation on crop height and coherence observations.

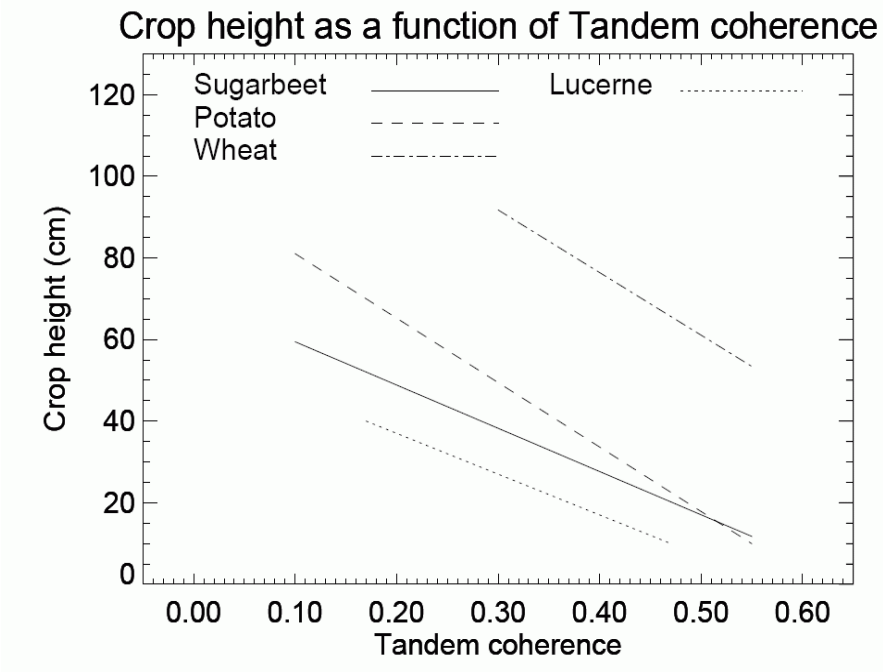

Figure 16. Derived linear relationships between ERS-1/2 Tandem InSAR coherence and agricultural crop heights during the early growing season. The lengths of the lines indicate the applicability-range of the linear relationships for each crop.

The derived relationships between crop height and Tandem InSAR coherence are:

Sugar beet:	$h(cm) = 70 - 110 * \gamma$
Potato:	$h(cm) = 100 - 160 * \gamma$
Winter wheat:	$h(cm) = 140 - 150 * \gamma$

These linear relationships behave as expected, for example the denser root crops sugar beet and potato are clearly separated from the cereal crop winter wheat. This is in line with the hypothesis that InSAR coherence declines as the crop height/density increases because then a greater part of the radar backscatter is coming from the vegetation canopy that decorrelates more rapidly than the underlying soil. This paper gives a strong indication that ERS-1/2 Tandem coherence can be exploited for crop height retrieval for some agricultural crops.

5.3.3.3. Discussion

The role of crop height measurements in agricultural monitoring is rather limited, but it can be used as an indirect measure of other features like crop biomass, phenological stage and the detection of possible problems with crop condition like lodging caused by wind and rain. The relationship between agricultural crop height and crop biomass is not as straightforward as it is in forests, where quite general allometric relationships can be used. Nevertheless, for most crop species the height and biomass are directly related to crop phenological stage during the first period of the plants growth, until maturity is reached. (Lopez-Sanchez and Ballester-Berman 2009).

Due to the scarcity of C-band InSAR data with short enough temporal baselines, only a handful of studies into agricultural monitoring with InSAR exist. Wegmüller and Werner studied agricultural crops using ERS-1 data from the 3-day repeat period and discovered that with the considered temporal baselines (6 - 21 days) low coherence is observed for crops such as corn, sugar beet, potatoes and sometimes even grass (Wegmüller and Werner 1997). They postulated that for these relatively dense canopies the scattering is dominated by the vegetation, and that coherence is decreasing with the increasing relative importance of vegetation scattering. On the other hand coherences of 0.84-0.91 were observed over an almost bare field with a 15-day repeat-cycle. Also, a strong correlation was found between the InSAR coherence and the soil cover fraction for rape seed. The authors conclude that similar relationships can be expected for other crop parameters such as the crop height and biomass, because all those parameters are closely related if only a single crop type and a specific cultivation practise are considered.

In *Paper A* it was discovered that both the heights of the studied crops (sugar beet, potato and winter wheat) and their ERS-1/2 Tandem coherence develop approximately linearly during the early growing season (Engdahl et al. 2001). The most likely explanation for the decrease of coherence with

increasing crop height was that as the crop grows, it screens the ground more effectively, and a greater part of the incident radar energy is backscattered from vegetation that decorrelates more rapidly than the underlying soil.

Blaes and Defourny studied the retrieval of crop parameters (canopy cover percentage and crop height) using ERS-1/2 Tandem data over a test site in Belgium (Blaes and Defourny 2003). Regression analysis was used to derive relationships between Tandem coherence and crop height for winter wheat, potato and sugar beet. For wheat and potato high R^2-values (0.92 and 0.82) were achieved with linear regression. For sugar beet linear regression yielded an intermediate R^2-value (0.62) and better results were achieved by using a power-function in the regression (R^2=0.79). This study demonstrated that Tandem coherence is highly sensitive to both crop height and canopy cover percentage, while soil moisture had only a slight influence on the coherence level. The authors conclude that ERS-1/2 Tandem coherence images have a great potential for agricultural applications and that a single source of data, i.e. a few ERS-1/2 Tandem pairs, could provide relevant crop monitoring information for at least four diverse crops.

The value of ERS-1/2 Tandem InSAR data in crop height retrieval has been demonstrated. An interesting future line of study would be applying the HUT-model (see section 5.3.2.4) into crop biomass or height retrieval. Further studies would also be needed to determine how environmental conditions affect crop height retrieval and what the optimal conditions are. It is unfortunate that there are currently no plans for Spaceborne C-band SAR systems capable of acquiring short temporal baseline InSAR data. The future ESA Sentinel-1 constellation will provide 6-day temporal baseline data, which unfortunately will probably suffer from too much temporal decorrelation for reliable crop height detection, unless the weather-conditions are exceptionally suitable. In any case, the coherence information from the Sentinel-1 constellation will definitely be beneficial for the classification of agricultural crops through the detection of bare or almost bare fields, even if crop height retrieval will turn out to be too unreliable for operational use.

5.3.4. Stem-Volume Retrieval in Boreal Forests

5.3.4.1. The Northern Boreal Forest Zone

The Northern Boreal Forest Zone (NBFZ) covers vast swaths of the Eurasian and North American continents and is one of the largest biomes on Earth. Boreal forests contain large amounts of plant biomass and the carbon cycling through the boreal forest biomes is highly significant in the global *carbon cycle*. Boreal forests are estimated to contain 30-50% of the global forest carbon, a range which demonstrates that the current estimates have large uncertainties (Dixon et al. 1994; Houghton et al. 2001). Therefore, accurate and timely information about the NBFZ forest biomass and its changes with time are vital also from a *carbon accounting* and climate research perspective.

Mapping and surveying the NBFZ is very challenging as major problems are caused by its size, remoteness and challenging weather conditions prevalent over large parts of the year. Due to these issues, mapping total NBFZ forest parameters like forest area and stem volume (related to biomass) using ground-based methods, or airborne surveys, is prohibitively expensive. This leaves satellite remote sensing as the only viable option for mapping and surveying the whole NBFZ. Existing optical satellites are not well suited for monitoring forest biomass and forest regeneration/degradation as the signal related to biomass can saturate at a rather low biomass levels. Additionally, the latitude-range of the NBFZ (~50N – 70N) causes additional problems for optical remote sensing as frequent cloud-cover and poor lighting conditions during winter make much of the optical imagery unusable.

5.3.4.2. Forest Inventories and Related Concepts

Forest inventories are usually ground-based surveys that measure many parameters of the assessed forest. The outcome of a forest inventory is usually information about forest parameters, like *stem volume*, per *tree species*, per measured *forest stand*.

5.3.4.2.1. Forest Stands, Stand Boundaries

A basic forest mapping and description unit is the *forest stand*, which can be defined as a relatively homogenous patch of forest in terms of tree composition and forest structure. Remote sensing based forest inventories are usually not very accurate at the pixel-level; that is, at the spatial scale from a few metres to a few tens of metres, depending on the instrument, and the use of larger stand-sizes that aggregate many pixels generally leads to higher accuracies (Hyyppä and Hyyppä 2001). In the boreal forests of Finland the size of the forest stands varies typically from 0.5 ha to tens of hectares, whereas in Michigan, for example, even the smallest homogeneous forest stand**s** are usually larger than 10 ha (Dobson et al. 1995; Hyyppä and Hyyppä 2001). On larger stands several instrument pixels fall within the stand, and the accuracy of remote sensing based forest

inventories can be increased by dealing with stand averages instead of the values of individual pixels.

Presently, forest *stand boundaries* are usually defined based on *aerial photographs*, while forest attributes are collected in a field survey on the ground. Ground surveys are obviously expensive, but for large areas the effort and cost involved in just determining the stand boundaries from aerial images may be prohibitive. Therefore, it is desirable to be able to derive applicable stand boundaries from the remotely sensed data itself using methods like segmentation (see section 5.2.3.3). In *Paper E* the boreal forest stand boundaries were derived by segmenting the temporal average of InSAR coherence and the performance in stem volume retrieval was found to be of comparable quality to retrieval using traditionally derived stand boundaries.

5.3.4.2.2. Forest Stem Volume and Biomass Estimation

Forest *stem volume* is one of the key characteristics in forest inventories. It is an essential characteristic in forest and climatological research as it is directly related to the level of the total forest biomass. In boreal forests, the *above-ground dry biomass* measured in tons/ha is approximately 0.6 times the stem volume measured in m^3/ha (i.e. 100 m^3/ha stem volume corresponds to 60 tons/ha above-ground dry biomass) (Häme et al. 1992). Stem volume itself is defined as the volume of wood in the main stem of a tree and it is commonly measured in cubic metres (m^3) or in cubic metres per hectare (m^3/ha) when the density of forest stands is being discussed. Another closely related concept is the forest *Growing Stock Volume* (GSV), which is defined in Russian forest inventory standards as "*the stem volume for all trees with at least 6 cm diameter at breast heights (1.3 m)*" (Eriksson et al. 2003). In practise stem volume and GSV can be used interchangeably and their exact definition depends on local forest inventory practises.

5.3.4.2.3. Use of Training Data

Most stem volume retrieval methods based on remote sensing require a set of *training stands* with known boundaries and stem volumes. These values are then used to determine the regression/model parameters that enable stem volume retrieval for forest stands with unknown stem volumes. High quality training data makes stem volume retrieval more accurate, but unfortunately such data is not available for large parts of the NBFZ due to the prohibitive costs related to gathering such datasets. Therefore, methods that do not require training are needed if stem volume retrieval over the whole NBFZ is desired. Several stem volume retrieval methods that don't require forest inventory data have been presented, for example Wagner et al. 2003 and Tansey et al. 2004 used histogram analysis of SAR intensity images to determine forest stem volume classes, while Santoro et al. 2011 used optical satellite products to determine the location of "open" and "dense forest" areas in order to train their model. Askne and Santoro 2009 demonstrated an automated method that identifies dense and sparse areas

from ERS-1/2 Tandem coherence images for model training. These kinds of *training data free* approaches open the door for large scale stem volume mapping of the whole NBFZ.

5.3.4.3. Use of SAR Intensity Images

SAR is inherently more suitable than optical data for measuring forest biomass in the sense that SAR uses microwaves that are, thanks to their wavelength, able to penetrate inside the canopy. The backscattered intensity can be used to retrieve forest biomass, but the problem is that the signal saturates rather early (depending on the wavelength) and thus prevents mapping forests with high stem volumes. According to Imhoff the intensity saturation limit at C-, L- and P-bands are at 20 tons/ha (33 m^3/ha), 40 tons/ha (66 m^3/ha) and 100 tons/ha (167 m^3/ha), respectively, in broadleaf evergreen and non-boreal coniferous forests (Imhoff 1995). Higher saturation limits of 64 m^3/ha at L-band and 143 m^3/ha at P-band have been reported in boreal forests (Fransson 1999). In general cross-polarised (HV) backscatter is best suited for stem volume retrievals and P-band HV-polarised backscatter showed no signs of saturation at least until ~600 m^3/ha (Rauste et al. 1994). The shorter wavelengths at X- and C-bands are more sensitive to changes in soil and canopy soil moisture, and the correlation between stem volume and boreal forest backscatter varies from positive to negative depending on moisture conditions (Pulliainen et al. 1994). This is why the longer wavelengths at L- and P-bands are more attractive to stem volume retrieval as with them the correlation between stem volume and radar backscatter is always positive in boreal forests. A candidate satellite-mission called BIOMASS has been proposed to ESA in the 7th Earth Explorer Core Mission call. If selected, BIOMASS will use a P-band SAR to measure the biomass of all the Earth's forests, including dense tropical forests at 50m spatial resolution (Scipal et al. 2010).

Despite the many results demonstrating signal saturation at short wavelengths, these results are correct on average and at the pixel-level, or with small forest stands. Better results have been achieved by picking the "best" SAR images (i.e. the ones with most favourable environmental conditions) from large stacks of data and aggregating the results into larger pixels. Recently it has been demonstrated that using such *hypertemporal* observations at C-band and aggregating the results into pixel sizes from 1 km to tens of kilometres, it is possible to retrieve boreal forest stem volume at least up to 300 m^3/ha (500 tons/ha) without signs of signal saturation (Santoro et al. 2011).

5.3.4.4. Multitemporal InSAR in Stem Volume Retrieval

As discussed in the previous section, C-band SAR backscattered intensity has only a limited use in stem volume retrieval at the pixel-level or at small stand-sizes, even though a hypertemporal approach has enabled good stem volume retrieval performance at pixel sizes of 1km and larger. Already the early repeat-pass InSAR studies noted that InSAR coherence was sensitive to forest density and that forest coherence was quite consistently lower than

the coherence over agricultural and open land (see section 5.1). Further studies confirmed that especially in sparse boreal forests, InSAR appeared to be a promising data source (Askne et al. 1997; Koskinen et al. 2001). Even though C-band InSAR coherence was found to be more sensitive to boreal forest stem volume than C-band intensity, it quickly became evident that environmental conditions have a very strong influence on coherence and its sensitivity to biomass can drop practically to zero at worst. Even though environmental effects have a large effect on coherence, two ERS-1/2 Tandem coherence images acquired even months apart were found to be on average clearly more correlated with one another than intensity images acquired only one day apart (Askne and Santoro 2005). Despite the strong environmental effects, InSAR has achieved relatively good stem volume retrieval (*Paper B*; *Paper E;* Koskinen et al. 2001; Santoro et al. 2002; Askne et al. 2003; Askne and Santoro 2005; 2007 and section 5.3.4.4.4).

Stem volume retrieval from multitemporal InSAR data is based on modelling the coherence as a function of stem volume and other parameters, and inverting the model in order to retrieve stem volumes. Modelling of vegetation canopies is discussed in section 5.3.2 and the complexity of possible models varies from relatively simple to very complex. Studies have shown that relatively simple empirical and semi-empirical models based on Water-Cloud Models (WCM) (see section 5.3.2.3) describe the average behaviour of interferometric coherence as a function of forest stem volume. Askne et al. presented the Interferometric Water-Cloud Model (IWCM), which is an extension of the basic WCM to describe the coherence of forest stands taking into account the effects caused by non-zero baseline lengths (Askne et al. 1997). The HUT-model for boreal forests (see section 5.3.2.4) is a simplified version of the IWCM, which reduces to the HUT-model if the baseline-length is set to zero (*Paper B*). In Fransson et al. 2001 and Koskinen et al. 2001 the Tandem coherence was found to depend on stem volume in a linear fashion, at least on the best InSAR pairs. In *Paper B* the relation between stem volume and coherence was found to be better explained by an exponential function, even though in the HUT-model the coherence is modelled to depend linearly on the fraction of canopy backscatter of the total forest backscatter (see section 5.3.2.4 and Koskinen et al. 2001). This implies that when stem volume increases, the fraction of canopy backscatter increases in an exponential fashion. In addition to semi-empirical (model-based) approaches, also purely empirical approaches (regression) have been used for example in Wagner et al. 2003, Fransson et al. 2001 and Hyyppä et al. 2000.

If more than one InSAR pair is available, a multitemporal approach to stem volume retrieval can be utilised for increased retrieval accuracy (*Paper B*; Santoro et al. 2002). In *Paper B* the best stem volume retrieval accuracy was reached when using just the two best pairs out of a set of 14 InSAR pairs. This demonstrates how stem volume retrieval with multitemporal InSAR is *opportunistic*, and that picking the very best pairs produces better results than combining a number of quite good pairs in the retrieval. In practical terms this means that in order to achieve the best results, one needs to wait for suitable environmental conditions, and that

relying on only a few of InSAR pairs does not necessarily guarantee a satisfactory outcome.

5.3.4.4.1. Effects of Environmental Conditions on Stem Volume Retrieval

In the HUT-model and in IWCM-models for boreal forest in general, the observed boreal forest coherence depends on the coherences of the canopy-layer and that of the ground-layer, and what is the fraction of the observed backscatter that is modelled to return from the ground, and from the canopy (see section 5.3.2.4). This ability to assess the backscatter and coherence of the ground-layer and the canopy-layer separately can increase our understanding of the effects of environmental conditions on observed forest coherence, i.e. the coherence of the forest areas as seen by the radar.

As discussed in section 5.3.4.3, environmental conditions can lower the correlation between InSAR coherence and stem volume to practically zero, making the InSAR pair unusable for stem volume retrieval using any coherence-based method (see *Paper B*). Broadly speaking environmental conditions can cause coherence-loss through temporal decorrelation (see section 4.4.2) in two ways:

1. By causing dielectric changes (see section 4.3.3), which can influence the relative amounts of backscatter returning from the ground-layer or from the canopy-layer. This can be caused by anything that changes the total soil and canopy liquid water content. Known causes for moisture changes include precipitation, freezing/thawing of snow, temperature and temperature changes, insolation and wind.
2. By causing movement of the scatterers within the scene. This can be caused for example by wind and precipitation.

Dielectric Changes

Dielectric changes (see section 4.3.3) in boreal forests are in practise caused by changes in the amount of liquid water within the forest, which can be caused by multiple weather-related effects. Dielectric changes can cause temporal decorrelation over boreal forests by altering the relative amounts of backscatter coming from the canopy- and the ground-layers, which usually have unequal coherence levels. In addition, the dielectric changes can happen in an heterogeneous way at the pixel and sub-pixel level, directly causing decorrelation of the coherence signal. For example, changes in the ground-layer soil-moisture distribution within a resolution-cell are considered to be a major factor causing temporal decorrelation (Askne et al. 2003).

In practical terms the amount of liquid water and backscattered intensity are positively correlated. An increase in backscatter causes a decrease in transmissivity, so a wetter forest canopy-layer exhibits both increased backscatter and reduced transmissivity. If the whole forest (canopy- & ground-layer) gets wetter, the fraction of backscatter from the canopy-layer increases, and at the same time the reduced canopy

transmissivity attenuates the backscatter coming from the ground-layer. On the other hand if the ground-layer is wet (relatively speaking), and the canopy-layer is dry, the fraction of ground-layer backscatter increases due to the increased backscatter from the ground and the increased transmittance and reduced backscatter of the canopy.

Liquid water can be present in vegetation either inside the plants themselves (in tree-trunks, branches, needles etc.) or outside them as liquid water or wet snow covering the vegetation. Typically, the interferometric images obtained under snow-covered conditions show very high coherence values (Koskinen et al. 2001, Santoro et al. 2002, *Paper B*). According to experiments the trees themselves start freezing at temperatures around -5°C to -7°C (Koskinen et al. 2001), which decreases their liquid water content and should therefore decrease canopy backscatter and increase transmissivity (Askne et al. 2003). In temperatures that were well over freezing the dielectric constant of *sitka spruce* needles has been reported to have a diurnal variation due to a changing water content (Drezet and Quegan 2006). Frozen winter conditions are most stable in the dielectric sense and therefore most conducive to high coherence values. A freezing/thawing event can be expected to change the dielectric properties of the forest, and low overall boreal forest coherence has indeed been observed with such a freezing event (*Paper B*). Rapidly melting wet snow has been associated with very low coherence values and a slight positive correlation between stem volume and forest coherence – the postulated reason for this was a rather large (on average 6cm) inhomogeneous drop in snow-thickness, which can be assumed to change the dielectric properties and relative positions of the scatterers in an inhomogeneous way (*Paper B*).

Rainfall before the image acquisition can obviously affect the amount of free water in the canopy and in the ground layer (soil + undergrowth). Heavy rain between the Tandem observations has been observed to reduce boreal forest coherence to a low level (*Paper B*). The development of soil moisture levels after rainfall is a complex issue, but in general one can assume that the canopy, being more exposed to the drying influences of the wind and the sun, will usually dry somewhat quicker than the ground-layer. Soil moisture levels are easier to predict than canopy water content due to the slower dynamics of soil moisture (Drezet and Quegan 2006).

Movement of Scatterers

Movement of the scatterers is a major cause of temporal decorrelation in boreal forests. As discussed in section 4.4.2, with ERS-1/2 C-band data just a few centimetres of RMS movement will completely decorrelate the signal. Since wind is continuously moving the tree-branches, this type of decorrelation happens in a matter of seconds. Since the signal from the canopy is not completely decorrelated at C-band, except in high wind conditions, this shows that part of the backscattered signal must come from more stable-enough parts of the canopy, i.e. for example from some of the thicker and more stable branches. Observations have shown that in general low wind speeds at the time of the SAR acquisitions are conducive to

relatively high forest coherence, and high wind speeds to low coherence (*Paper B*; Askne et al. 1997; Drezet and Quegan 2006). On hilly terrain the angle between the wind-vector and the normal vector of the terrain has been found to affect forest coherence (Castel et al. 2000). Even though stem volume retrieval works better when the overall forest coherence is high, there is evidence that light winds are preferable to still conditions as they increase the *Interferometric Coherence-Contrast* (ICC) between open areas and dense forest (Askne and Santoro 2007). In addition to wind, heavy rain can also be responsible for decorrelation during SAR acquisitions by causing scatterer movement. The presence of snow-cover on the trees during winter may have a damping effect on wind-induced movements in the canopy, which may contribute to the relatively high canopy coherences observed during winters.

5.3.4.4.2. Conditions Favourable to Stem Volume Retrieval

As discussed above, non-controllable environmental conditions have a large impact on C-band InSAR coherence of the forest. The interaction between environmental conditions and the dielectric properties and the positions of the scatterers observed by the C-band SAR are complex and so far attempts to predict forest coherence levels based on available environmental data have not been successful (Drezet and Quegan 2006). However, some environmental conditions are conductive to higher boreal forest coherence levels, and lead to better stem volume retrieval performances. Favourable and unfavourable conditions at C-band can be summarised as follows:

- Stable weather conditions between acquisitions are favourable, and a change in weather is unfavourable.
- Stable temperatures are favourable. A change from freezing to melting conditions or vice-versa is especially unfavourable.
- The presence of dry snow-cover is favourable, unless the snowpack is experiencing melting (wet snow), or a freezing/melting-event takes place between the image acquisitions.
- Strong winds at the time of image acquisitions are unfavourable. Moderate winds are preferred for better open/dense-forest contrast.
- Precipitation (rain or snow) between image acquisitions is unfavourable.

The absolute best conditions for stem volume retrieval are stable winter conditions with temperatures at least a few degrees below freezing, with dry snow cover and moderate winds. In these conditions the difference between the coherences of dense forest and open land are the highest, leading to high stem volume retrieval performance. The second best stem volume retrieval conditions are non-rainy snow-free periods.

5.3.4.4.3. Interferometric Coherence-Contrast and Image Pair Selection

As discussed in the previous section, environmental conditions have a large influence on stem volume retrieval, and the suitability of a random Tandem

pair is rather hard to predict. Therefore, the suitability of a particular InSAR pair for stem volume retrieval can only be assessed afterwards by looking at the acquired data. As one might expect, stem volume retrieval performs well when the coherence of the open areas is high and the coherence of dense forest is low (*Paper B*; Fransson et al. 2001; Askne et al. 2003). On these kinds of coherence images the *Interferometric Coherence-Contrast* (ICC) over boreal forests, defined as the difference in coherence between very sparse and dense forests, is the highest.

In *Paper D* four different boreal forest coherence-based measures (including the ICC) were studied as indicators of stem volume retrieval performance, and the ICC was found to perform the best. The ICC had a strong positive linear correlation with stem volume retrieval performance, and more importantly, it could deal with pairs with anomalous coherence values (due to environmental conditions) in a robust way. The ICC could be used as an indicator for InSAR pair quality in operational stem volume retrieval.

5.3.4.4.4. Stem Volume Retrieval Performance in Existing Studies

A large number of studies have confirmed the high potential of ERS-1/2 Tandem InSAR data for boreal forest stem volume retrieval. Also it has been amply demonstrated that the seasonal and environmental conditions have a major effect on the stem volume retrieval performance. The availability of multitemporal InSAR observations generally increases stem volume retrieval performance as it is more likely that at least some of the InSAR pairs have been acquired in suitable conditions.

Castel et al. studied stem volume retrieval in coniferous plantation forests in Southern France using four ERS-1/2 Tandem pairs, and achieved R^2-values of up to 0.55 when using linear regression (Castel et al. 2000). No saturation was detected in the retrievals up to at least 250m^2/ha and the accuracy of the retrieval was found to stay constant over the stem volume range. Fransson et al. analysed stem volume retrieval on five ERS-1/2 Tandem pairs using regression on a test site in Central Sweden, and achieved performance up to R^2=0.87 when using the best InSAR pair (Fransson et al. 2001). Koskinen et al. studied the seasonal behaviour of boreal forest coherence using nine ERS-1/2 Tandem on two test sites in Southern Finland. Stem volume retrievals through inversion of the HUT-model (see section 5.3.2.4) yielded R^2-values of up to 0.57 with no apparent signs of saturation at higher stem volumes. (Koskinen et al. 2001). Santoro et al. used the IWCM (see section 5.3.2.3) and a multitemporal approach for stem volume retrieval on a test site in Central Sweden (Santoro et al. 2002). The achieved R^2-values of up to 0.94 can be considered to be extremely high and have yet to be replicated on other test sites. This level of performance can be partly explained by the availability of very high quality ground truth data, the forest stand characteristics (managed forest, very homogeneous stands) and adjusting the R^2-values for the estimated errors in the ground truth data itself. In *Paper B*, as explained earlier in this chapter, a multitemporal approach was used in conjunction with the HUT-

model achieving R^2-values up to 0.79 when using the two best Tandem pairs (Pulliainen et al. 2003). In *Paper E*, the same ERS-1/2 Tandem dataset was used, but the forest stand boundaries were derived from the InSAR data itself via segmentation (Engdahl et al. 2008). The achieved stem volume retrieval performance was R^2=0.79 on all stands and R^2=0.87 on stands larger than 1.5 ha, which is comparable to the retrieval performance in Pulliainen et al. 2003, which shows that segmentation of the InSAR dataset is a viable method for forest stand boundary definition. Askne et al. have been studying multitemporal ERS-1/2 Tandem InSAR for stem volume retrieval in a number of studies through the years (Askne et al. 2003; Askne and Santoro 2005; 2007; 2009). These studies have shown that rather high accuracies can be expected with the multitemporal approach on stands that are larger than 2 ha, and that the retrieval accuracy is better on more homogeneous stands. Also, when IWCM and the HUT-model are compared on the same datasets, there are indications that the IWCM performs better than the simpler HUT-model at higher baseline lengths (Askne and Santoro 2005). There is a possibility that stand boundaries derived from the InSAR dataset itself via segmentation might produce more homogeneous stands, and therefore more accurate stem volume retrieval accuracy as a whole, than using stand boundaries from possibly out-dated ground based forest inventories. In their 2009 study Askne and Santoro describe a method for stem volume retrieval that does not require training data, but only information about the maximum forest stem volume in the study area (Askne and Santoro 2009).

5.3.4.5. Presentation of Paper B, Paper D and Paper E

All three papers are based on studying the same multitemporal ERS-1/2 Tandem InSAR dataset of the Helsinki metropolitan area in Finland. The InSAR dataset and its processing are described in section 4.5.2.

Paper B and *Paper D* deal with "pure" boreal forest stem volume estimation while *Paper E* is a "mixed" paper in the sense that it deals with combining segment-based land-cover classification with a subsequent boreal forest stem volume estimation step. The land-cover classification step of *Paper E* is described in section 5.2.4.2 and the boreal forest stem volume estimation step in section 5.3.4.5.3.

5.3.4.5.1. Paper B

This paper investigated stem volume retrieval on boreal forest stands using multitemporal ERS-1/2 Tandem InSAR data on a test-site in Tuusula, Southern Finland. Stem volume estimation was based on inverting the backscattering-coherence model for HUT boreal forests.

The SAR data used in this study consisted of 14 ERS-1/2 Tandem InSAR pairs covering the time-period from the summer of 1995 to the summer of 1996, and in situ measurements of stem volume were available for 210 boreal forest stands. Weather data on temperature, precipitation, wind speed and snow depth were used to assess environmental effects on boreal forest coherence. Backscattered intensity and InSAR coherence were

estimated over the forest stands and temporal filtering was used to reduce noise of both the intensity and coherence image sets.

Boreal forest stem volumes were estimated by inverting the HUT model (see section 5.3.2.4) using constrained statistical inversion that retrieves the maximum likelihood estimate for stem volume given the multitemporal set of InSAR observations. In the inversion process the HUT backscatter model was first fitted into the observed intensities on the training forest stands for every interferometric pair, and in the second step the HUT coherence model was fitted into the observed coherences on the training stands for every interferometric pair. In the last step of the inversion process the maximum likelihood estimate of stem volume for any forest region was retrieved by minimising the difference between observed and modelled coherence over the whole set of InSAR observations.

The feasibility of the HUT boreal forest backscattering-coherence model was assessed by analysing how well the model explains the behaviour of stand-wise ERS-1/2 Tandem InSAR coherence under different seasons and varying weather conditions. Figure 17 shows the results of fitting the HUT model to the training data on the 14 InSAR pairs. The figure clearly indicates that the response of coherence to increase in stem volume is nonlinear, and that the behaviour of coherence varies considerably from one InSAR-observation to the next. Differences in environmental conditions are the cause of this variation.

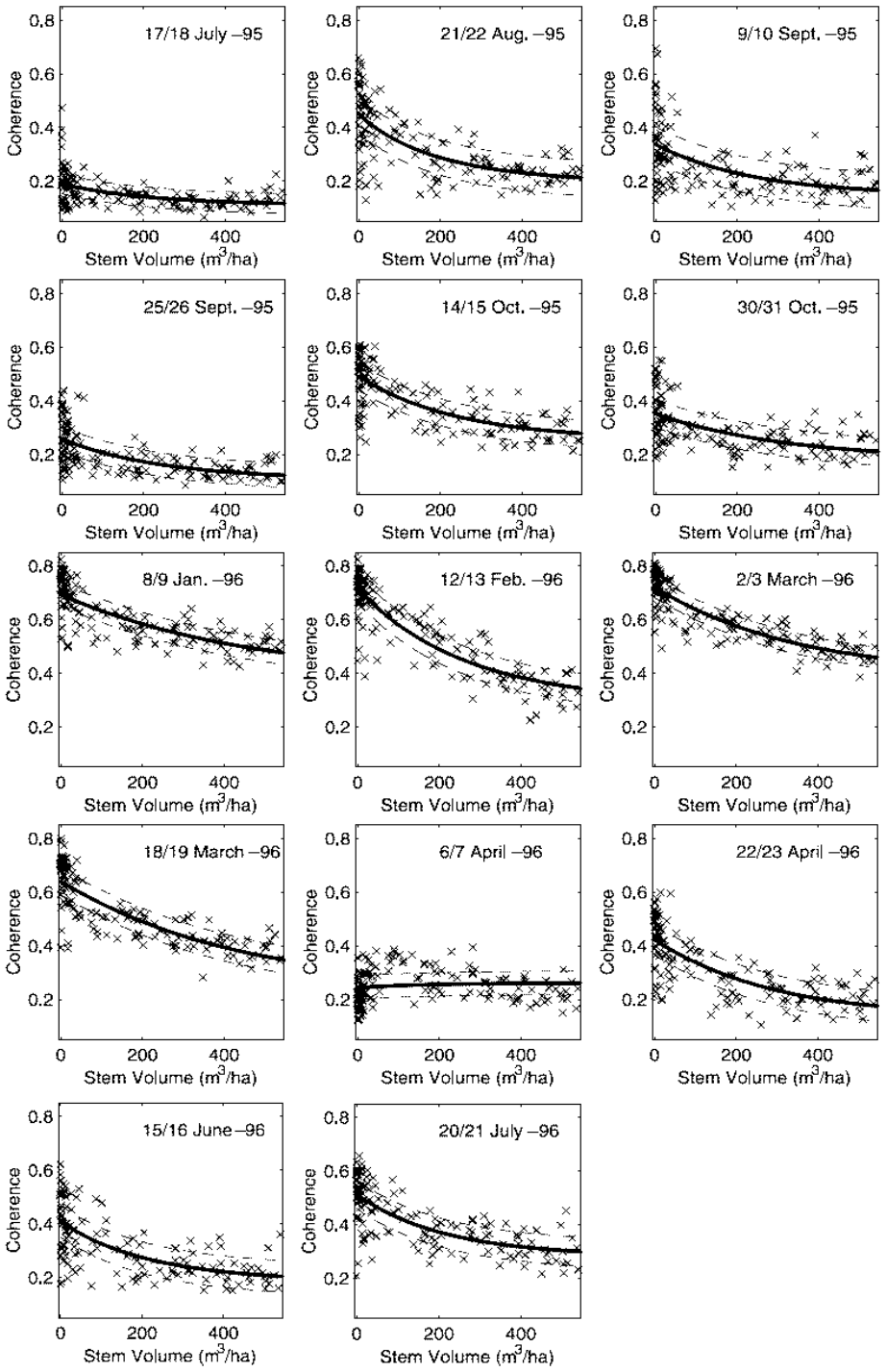

Figure 17. Fitting of the HUT backscattering-coherence into the stand-wise coherence observations on the 14 InSAR pairs.

Best stem volume retrieval performance was achieved by using the two most suitable InSAR pairs (acquired in most favourable weather conditions), and the stem volume retrieval accuracy (R^2 = 0.79, RMSE% = 48%) was found to be comparable to that achievable using optical satellite images. Generally the most suitable InSAR pairs for stem volume retrieval are those with the highest dynamic in forest coherence, i.e. the difference in coherence between open areas and dense forest stands, which is also called the ICC. Figure 18 plots the correlation coefficient between the intensity images (computed over forest stands) in an interferometric pair against the ICC. The figure shows that wintertime InSAR pairs acquired during dry snow conditions produce the strongest coherence response from stem volume, and that non-rainy snow-free conditions the second strongest. Precipitation, freezing or rapid snow melt between the acquisitions, as well as strong wind coinciding with one or both image acquisitions decrease the coherence response to stem volume, and reduce the utility of that InSAR pair for stem volume retrieval purposes.

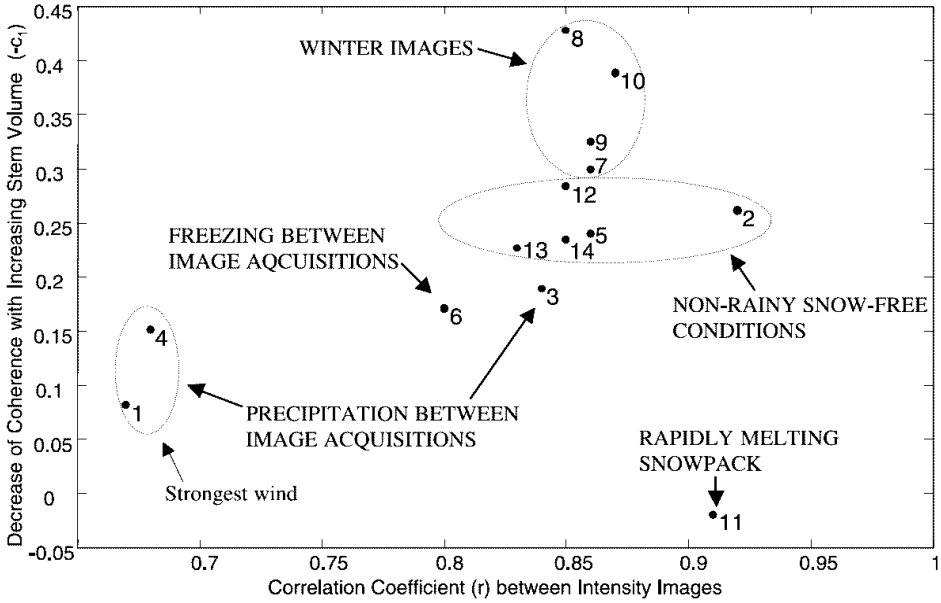

Figure 18. Effects of weather and seasonal conditions on InSAR coherence and stand-wise correlation of the intensity images in an InSAR pair. X-axis displays the correlation between the intensity images in an InSAR pair (computed over boreal forest stands) and y-axis the difference in coherence between open areas and dense boreal forest.

5.3.4.5.2. Paper D

This paper investigates four measures for assessing the suitability of an InSAR pair for stem volume retrieval. The study was conducted using multitemporal ERS-1/2 Tandem InSAR data on a boreal forest test-site in Tuusula, Southern Finland. The suitability of InSAR pairs for stem volume retrieval was assessed by performing stem volume estimation by inverting the HUT boreal forest backscattering-coherence model (see section 5.3.2.4).

The SAR data used in this study consisted of 14 ERS-1/2 Tandem InSAR pairs covering the time-period from summer of 1995 to summer of 1996, and ground-based measurements of stem volume for 134 boreal forest stands. Weather data on snow conditions was used in the analysis. Nine of the 14 Tandem pairs were acquired in snow-free conditions, four pairs in conditions with dry snow, and one pair when the snow pack was wet and melting.

InSAR–based boreal forest stem volume retrieval performance is strongly affected by weather conditions around the time of the SAR image acquisitions. Since weather conditions cannot be controlled, the suitability of a particular InSAR pair for stem volume retrieval can only be assessed afterwards. Therefore, suitability measures that could be used to pick the best InSAR pairs for stem volume retrieval purposes are desired. In this study, the following four coherence-based suitability measures were compared:

1. *Interferometric Coherence-Contrast (ICC),* which is defined as the difference in InSAR coherence between low (in this case defined to be < 5m^3/ha) and high stem volume stands (in this case defined to be > 350 m^3/ha);
2. A*verage InSAR coherence over boreal forests*;
3. *Average coherence of low stem-volume stands* (in this case defined to be < 5m^3/ha);
4. *Average coherence of high stem-volume stands* (in this case defined to be > 350m^3/ha);

The suitability of each Tandem pair for stem volume retrieval was measured by calculating the R^2–value between InSAR-estimated stem volume and the ground truth. The relationship between the suitability measure and the R^2–value are plotted for both the average boreal forest coherence, and the ICC, in Figure 19 and Figure 20 as examples. Snow-free cases, dry-snow cases and wet-snow cases are indicated with circles, stars and crosses, respectively. Note that in the wet-snow case the difference in coherence between low- and high-volume stand is practically zero, which makes InSAR-based stem volume retrieval impossible. All the four suitability measures are directly proportional to stem volume retrieval performance and the R^2-values between the suitability measures and stem volume retrieval performance are 0.84 for the ICC, 0.72 for the average forest coherence, 0.85 for the low stem volume stands and 0.51 for the high stem volume stands.

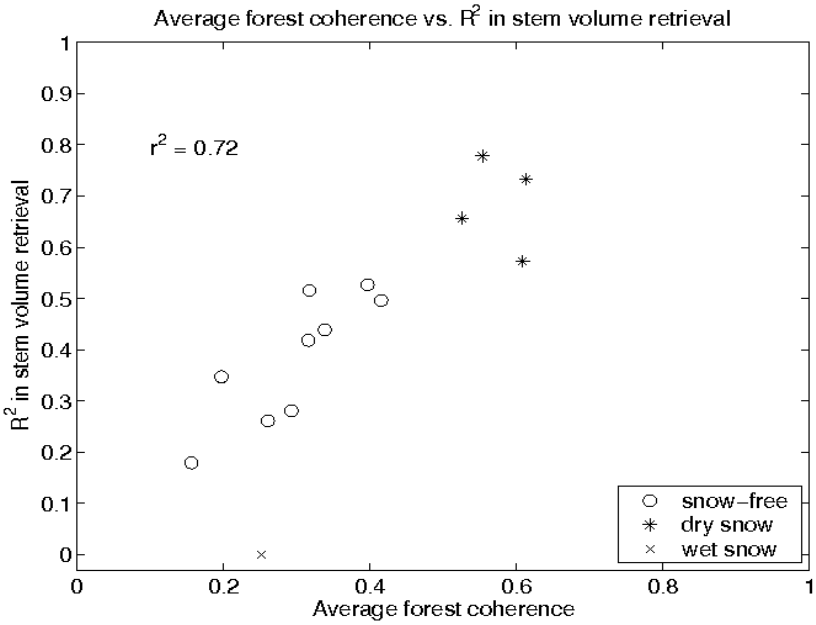

Figure 19. R2–values in stem volume retrieval as a function of the average forest coherence (=all forest stands) for the 14 Tandem pairs.

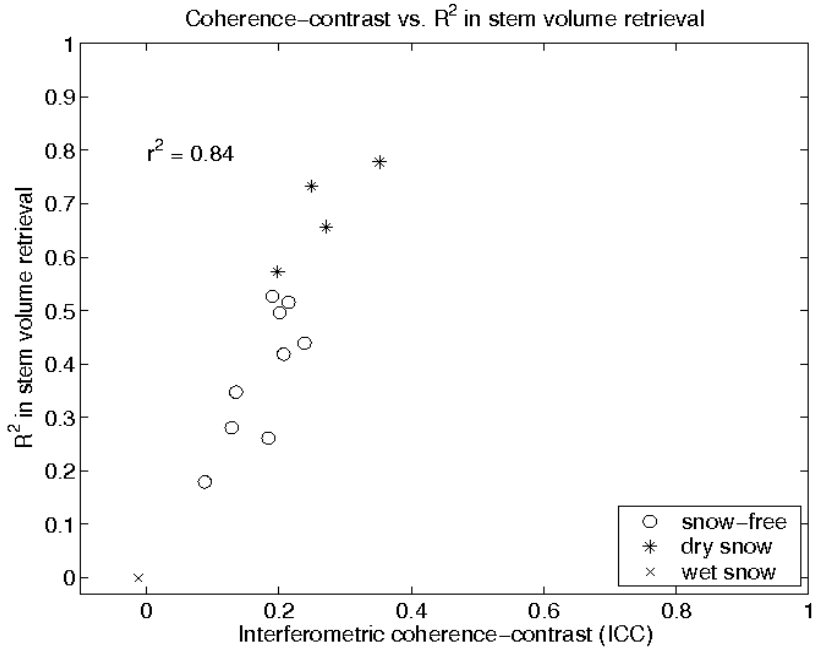

Figure 20. R2–values in stem volume retrieval as a function of the ICC for the 14 Tandem pairs.

In Figure 19 the correlation between average forest coherence and stem volume retrieval performance is quite high, but the wet-snow case stands out as a clear outlier. The wet-snow case is also an outlier when using the coherence of only high- or low-stem volume stands as a suitability measure (see Paper D for all of the plots). It is evident that these simple measures based on one coherence reading cannot deal with cases when weather conditions have rendered difference in coherence for sparse and dense forests close to zero. On the other hand, the ICC (see Figure 20) is a direct measure of the difference in coherence between the low- and high stem volume stands, so it can always recognise such situations. As the ICC is also strongly correlated with stem volume retrieval performance ($R^2 = 0.84$), it can be concluded that it is the most robust of the studied four coherence-based measures.

5.3.4.5.3. Paper E (Boreal forest stem volume estimation content)

Note: This paper deals with segmentation-based land-cover classification that is followed by boreal forest stem-volume retrieval. This section deals with the stem volume retrieval aspects of the Paper while land-cover classification is discussed in section 5.2.4.2.

In this paper a novel segment-based method is developed for the combined land-cover classification and boreal forest stem-volume estimation using multitemporal ERS-1/2 Tandem InSAR data. Stem volume estimates over forest segments were derived by inverting the HUT backscattering-coherence model for boreal forests and the results were compared against ground-based reference data and estimates produced by the satellite-based operational National Forest Inventory (NFI) of Finland. The study was conducted on a 366km^2 area in Southern Finland that covers the Tuusula boreal forest test site. The reference data consisted of high-resolution orthophotos, oblique aerial images, national base maps and stem volume data from the National Forest Inventory of Finland (NFI).

The combined land-cover classification and stem volume estimation method developed in this study has three steps:

1. Segmentation of the study area into quasi-homogenous segments based on the temporal average of InSAR coherence *(this step is presented in section 5.2.4.2*).
2. Classification of the segments into forest and other land-cover classes based on the multitemporal InSAR signatures of the segments (*this step is presented in section 5.2.4.2*).
3. Estimation of forest stem volume for all forest segments by inversion of the HUT backscattering-coherence model for boreal forests.

After the forest segments were created in steps 1 and 2, stem volumes of the forest segments were estimated by inverting the HUT backscattering-coherence model for boreal forests (see section 5.3.2.4). A forward selection

rule was used to pick the best InSAR pair combinations for stem volume retrieval. Best results were obtained using two InSAR pairs acquired during wintertime in dry snow conditions; these two pair also scored the 1st and 3rd highest values of the ICC-measure introduced in *Paper D*. Figure 13 in section 5.2.4.2 displays the combined land-cover and stem volume estimation map over the study area. In the figure stem volume estimates have been divided into 15 discrete stem volume classes for presentation, even though the used method provides continuous stem volume estimates.

In stem volume retrieval assessment the InSAR-based stem volume estimates were compared against ground-based measurements on the 210 forests stands in the reference data, and against the NFI-estimates on the 4176 InSAR-generated forest segments. The comparison between InSAR-based stem volume and the ground truth is plotted in Figure 21. For the 134 stands larger than 1.5 ha the performance (r^2=0.76, RMSE%=54%) is close to the results reported in *Paper B*. The results for segments smaller than 1.5 ha are quite poor, which is not surprising considering the resolution of the InSAR coherence images. (Figure 22)compares the InSAR-results against the estimates obtained from the operational NFI. It is clear that on this test site NFI underestimates stem volumes compared with InSAR and its estimates saturate at around 200 m^3/ha. Finally (Figure 23) shows the comparison between NFI and the ground-truth, which shows that NFI indeed saturates at around 200 m^3/ha on this site.

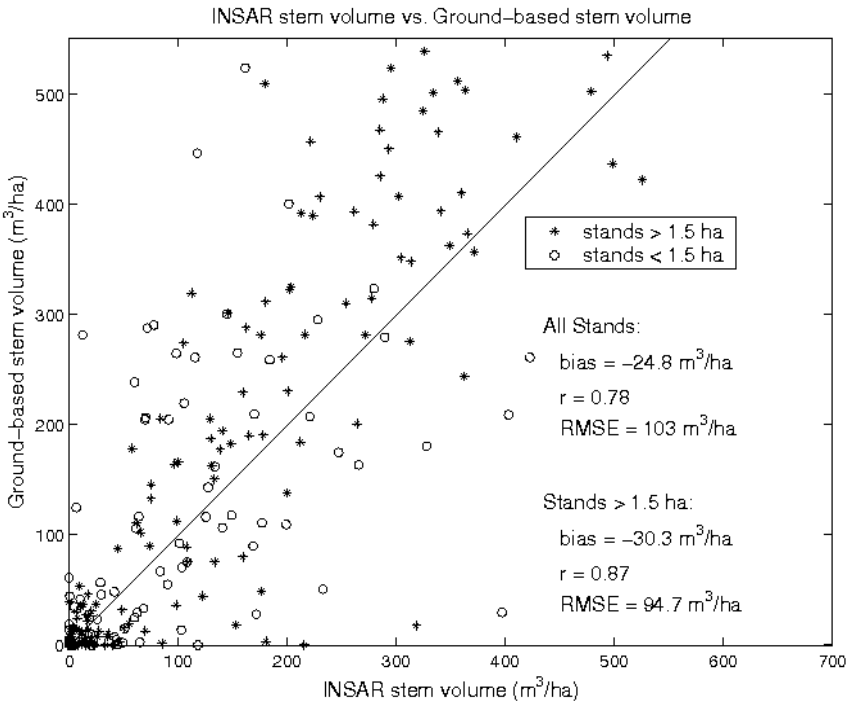

Figure 21. Comparison between InSAR-estimates on stem volume and ground truth on 210 forest stands.

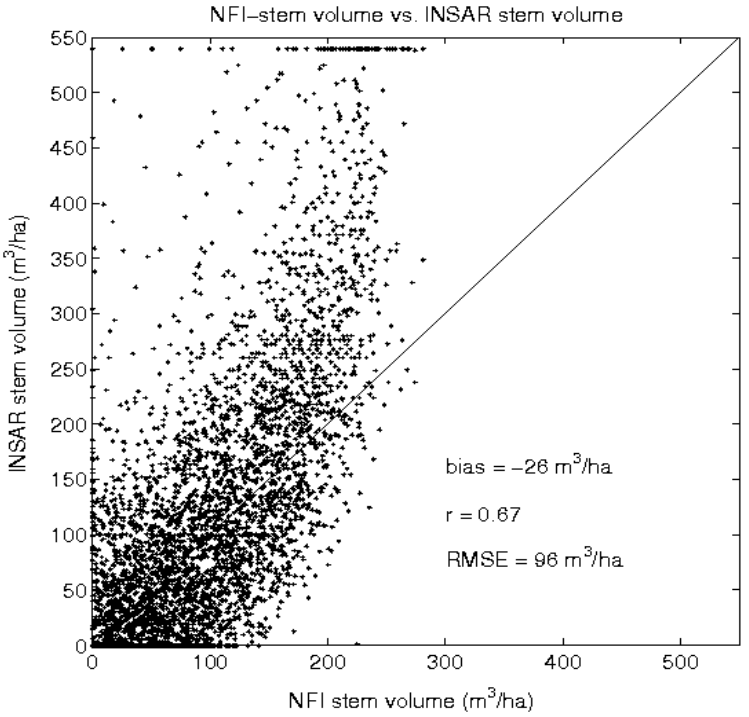

Figure 22. Comparison between the InSAR- and NFI-estimates on stem volume on 4176 InSAR-generated forest segments.

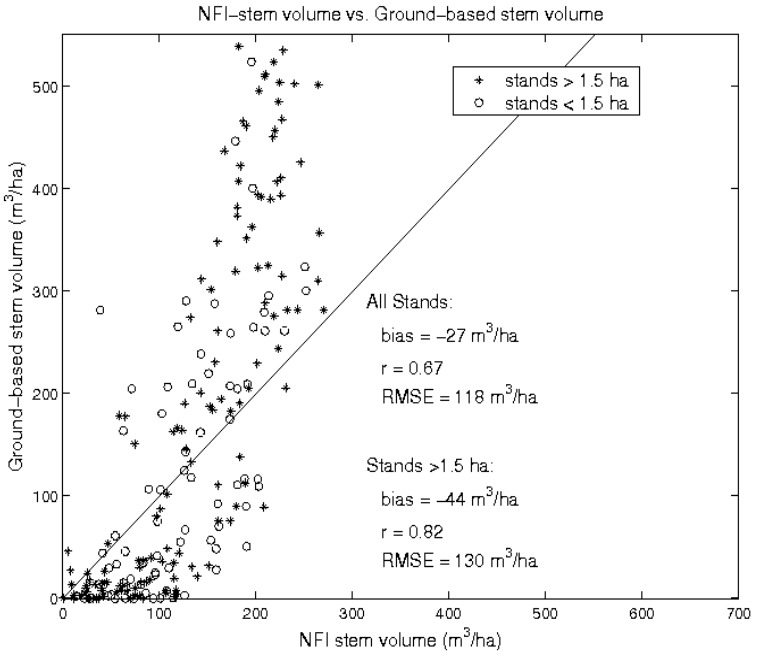

Figure 23. Comparison between the NFI-estimates on stem volume and the ground truth on 210 forest stands.

The main advantage of the presented segmentation-based method is that apart from the forest stand information used for training, it is not necessary to have information about the forest structure, but applicable forest stand boundaries are derived from the remotely sensed data itself. The stem-volume retrieval accuracy of the presented method is comparable with the accuracy achieved using the same method with stand boundaries taken from the forest inventory, as was done in *Paper B*, where an accuracy of r^2=0.79 and RMSE%=48% was achieved. The estimates produced by the operational NFI were compared against both the InSAR-estimates and ground-based reference data; both comparisons show that on this site InSAR-based stem volume retrieval performs better than the NFI which saturates at about 200 m^3/ha.

This study demonstrates that it is possible to derive usable forest stand boundaries from InSAR-data using segmentation, and that the stem volume retrieval performance with the derived stand boundaries is comparable to performance achieved with stands derived with traditional field surveying methods.

5.3.4.6. Discussion

In *Paper B* it was demonstrated that the HUT-model for boreal forests (see section 5.3.2.4) can, despite its simplicity, describe the stand-wise ERS-1/2 Tandem InSAR coherence of boreal forest stands quite well, at least when the interferometric baselines were relatively short. The more complex IWCM-model performs slightly better at longer baselines (see section 5.3.2.3 and Askne and Santoro 2005). Correlations of up to R^2 = 0.79 between the reference data and the inverted HUT model have been achieved in the most favourable environmental conditions (*Paper B*). These results are comparable to the best stem volume retrieval results from optical sensors. Compared with optical sensors SAR imaging has the advantage of not being compromised by cloud coverage, which is a common problem in optical remote sensing of boreal forests.

Environmental conditions have a large effect on boreal forest stem volume retrieval performance using ERS-1/2 Tandem InSAR data (see *Paper B* and section 5.3.4.4.1). Nevertheless, good retrieval performance is possible in favourable conditions (stable frozen winter conditions with dry snow cover, or non-rainy snow-free conditions with moderate winds). As environmental conditions are by and large uncontrollable, the repeat-pass InSAR based stem volume retrieval is by nature an *opportunistic* measurement, i.e. dependent on suitable environmental conditions. In practise this means that if only a few InSAR pairs over an area are available, satisfactory stem volume retrieval performance cannot be guaranteed. On the other hand, good stem volume retrieval conditions are virtually guaranteed if the user can wait and keep observing the area of interest. Even though it is possible to predict the suitability of an InSAR acquisition for stem volume retrieval to some degree by looking at the prevailing environmental conditions, the real suitability of as InSAR pair can only be

determined by looking at the data itself. As determined in *Paper D*, a very good way of assessing the suitability of an InSAR pair is to estimate the Interferometric Coherence Contrast (ICC), which is defined as the difference in coherence between dense forests and open areas. The ICC has a strong linear positive correlation with stem volume retrieval performance and it can identify pairs that are most suitable for retrieval (see *Paper D* and section 5.3.4.4.3).

In the standard approach to stand-wise stem volume retrieval the forest stand boundary information is coming from an external source, usually a *Geographic Information System* (GIS) database that is based on ground-based forest inventories (see section 5.3.4.2.1) and information about forest ownership etc. In *Paper E* the stand boundaries were derived from the InSAR dataset itself by segmenting the temporal average of the InSAR coherence, and the stem volume retrieval that followed resulted in retrieval accuracy comparable to the results achieved in *Paper B*, where external stand boundary information was used. This confirms that having access to external stand boundary databases is not mandatory, which is a major bonus when mapping boreal forest stem volumes over large and remote areas. It should be noted here that the forest stand boundaries derived from InSAR dataset are useful for stem volume retrieval and for remote sensing scientists, while foresters will most probably not find them useful for their forest management purposes.

Even if stand boundary information can be derived from the InSAR data, the stem volume retrieval method used in *Papers B, D and E* still requires external information for training the HUT model in the form of training forest stands with known stem volumes (see section 5.3.4.2.3). Moreover, since environmental conditions are spatially variable, the spacing of training data sites should be small enough to capture major differences in weather conditions etc. Such training data network is simply not available in very remote areas, and when available the training data is not sufficiently recent or of good enough quality. This problem could be solved by developing training-data free stem volume retrieval methods like the one presented in Askne and Santoro 2009, where “open” and “dense forest” areas and their coherence are determined from the coherence images themselves. Another related training-data free method (for C-band intensity data) is presented in Santoro et al. 2011, where the open and dense forest areas are located by using a global optical vegetation product called the *MODIS Vegetation Continuous Fields*. The combination of multitemporal InSAR with segmentation and training-data free methods could make it a viable method for stem volume mapping of very large areas, for example the whole NBFZ.

When the research reported in *Papers B, D and E* is reviewed together with the relevant scientific literature, it becomes clear that multitemporal ERS-1/2 Tandem InSAR data has a very high potential for stem volume retrieval in boreal forests. Even though environmental effects like weather and snow-cover have a large impact on the usability of a single InSAR pair, the opportunistic nature of the method guarantees that if enough data is available, the retrieval is virtually certain to succeed. This makes the

method suitable for operational stem volume retrieval over large areas, provided that the training-data free methods discussed above are developed further. In the future the ESA Sentinel-1 constellation should prove very valuable for stem volume retrieval over boreal forests despite the longer repeat period. The observation strategy of Sentinel-1 makes it perfectly suitable for opportunistic hypertemporal forest remote sensing because a steady stream of image acquisitions will be guaranteed for years to come. Even though six days is a lot longer than the 1-day temporal baseline of ERS-1/2 Tandem data, with enough acquisitions favourable conditions for stem volume retrieval will happen sooner or later. How long a wait is needed for successful stem volume retrieval is a topic for a future study with real data, but depending on the S-1 acquisition strategy yearly stem-volume mapping might become possible. The performance of stem volume retrieval with Sentinel-1 data will certainly be lower than with ERS-1/2 Tandem data, but the lower accuracy can most likely be mitigated by gathering additional good InSAR pairs and by aggregating the results to a lower resolution via segmentation.

6. Conclusions and Outlook

This work is an empirical study into the potential of multitemporal ERS-1/2 Tandem InSAR data in land-cover and vegetation mapping, and the main research question posed is:

> *What is the real potential and information content of ERS-1/2 Tandem InSAR time-series for land-cover and vegetation mapping?*

This main question gives rise to the following sub-questions:

a) *What is the contribution of the Tandem coherence time-series in land-cover classification compared with intensity-only time-series?*
b) *Can the Tandem InSAR coherence be related to the heights of agricultural crops?*
c) *How well does the Tandem time-series suit stem-volume retrieval in Boreal forest and how do weather conditions and seasonality affect the results?*
d) *How can the most suitable Tandem-observations for stem-volume retrieval be picked from a time-series of InSAR observations?*

This work confirms the high potential of multitemporal ERS-1/2 Tandem InSAR for both land-cover and vegetation mapping, even though only on a single test-site. The potential depends somewhat on the application (land-cover classification, crop height retrieval or stem volume retrieval in boreal forests), but still in all of these cases the C-band multitemporal InSAR data appears to be superior to multitemporal intensity-only data. The potential of multitemporal ERS-1/2 Tandem InSAR data can be briefly summarised application by application (more detailed information can be found in the respective discussions in sections 5.2.5 and 5.3.4.6):

- Land-cover classification: very high potential. Multitemporal ERS-1/2 Tandem InSAR data is clearly superior to multitemporal intensity-only data and allows the discrimination of a significantly larger number of classes (*Paper C*). Moreover, coherence and intensity carry complementary information and ERS-1/2 Tandem coherence carries greatly more land-cover related information than C-band intensity, which *answers the sub-question "a" above.*

- Crop-height retrieval: moderate to high potential. ERS-1/2 Tandem InSAR coherence appears to be related to crop heights approximately linearly (*Paper A*), *which answers the sub-question "b" above.* Further

studies would be needed to determine how environmental conditions affect crop height retrieval performance, what are the optimal conditions for retrieval and which crops can be mapped for crop height and under which SAR acquisition conditions.

- Stem-volume retrieval in boreal forests: high to very high potential. Multi-temporal ERS-1/2 Tandem InSAR data is very well suited to stem volume retrieval in boreal forests, even though environmental conditions have a large influence on stem volume retrieval accuracy (*Paper B*). *This answers the sub-question "c" above.* In the most suitable environmental conditions (see section 5.3.4.4.2) the stem volume retrieval accuracy is as good as, or better, than the accuracy attainable by optical remote sensing methods, with the added benefits that SAR can provide, like the possibility to image through clouds and in darkness. Measuring the Interferometric Coherence-Contrast (ICC), which is the difference in coherence between open areas and dense forests (see section 5.3.4.4.3), is a good way of picking good InSAR pairs from a time-series (*Paper D*), *which answers the sub-question "d" above.* It was discovered in *Paper E* that deriving forest stand boundaries from the multitemporal InSAR dataset itself did not degrade the retrieval performance*, partially answering the sub-question "e" above.* The derivation of the stand boundaries via segmentation is likely to increase stem volume retrieval performance on areas where stand boundary information derived via traditional forest inventories are not available.

Outlook

In the outlook-section one is allowed to speculate what an operational system for the combined land-cover and vegetation mapping based on multitemporal InSAR data could look like. As discussed, environmental conditions have a large influence on ERS-1/2 Tandem InSAR observations (both intensity and coherence). This is especially relevant for stem-volume retrieval in boreal forests, where suitable conditions are essential for good stem volume retrieval performance, and the best results are achieved by using a few of the very best InSAR pairs (*Paper B*). As environmental conditions are by and large uncontrollable, repeat-pass InSAR-based stem volume retrieval is by nature an *opportunistic* measurement, i.e. dependent on suitable environmental conditions. In land-cover classification the situation is somewhat different in the sense that the are no "bad" conditions as such, unless the conditions result in scenes/features that are totally uncorrelated with land-cover. If certain land-cover classes respond differently to changing environmental conditions, this difference can be exploited in the multitemporal InSAR classification and it can potentially lead to increased class-separability. For crop height retrieval the issue of environmental conditions is an open question as this issue has not been studied enough on ERS-1/2 Tandem InSAR data, but the studies performed so far indicate that ERS-1/2 Tandem InSAR data could be suitable for crop

height retrieval over some agricultural crops (*Paper A*). Nevertheless, one can assume that certain conditions are more suitable for crop height retrieval than others.

For an operational system having access to a long series of InSAR observations the opportunistic nature of vegetation parameter retrieval is not really a problem. If the user can wait and keep observing the area of interest, good conditions for vegetation parameter retrieval are a virtual certainty sooner or later, provided that the used repeat-period allows for sufficient coherence and least every once in a while. A combined land-cover classification and stem-volume estimation system is demonstrated in *Paper E*, where a segmentation-step is followed by a land-cover classification step, and then a stem-volume retrieval step. This kind of a staged approach could form the basis of an operational system in the following fashion:

1. Segmentation of the study area into quasi-homogeneous segments based on features of the multitemporal InSAR signatures of the image pixels. The selected features should contain relevant information about land-cover. After this step the dataset consists of segments instead of pixels and the corresponding InSAR signatures are less noisy than in the pixel-based case.

2. Land-cover classification of the segments created in Step 1. High land-cover classification accuracy can be expected based on *Paper C*. At this stage it is possible to re-segment the vegetated segments based on an InSAR feature that is most suitable for them, for example using the temporal average of InSAR coherence for the forest classes, as was done in *Paper E*. After this step all of the segments in the dataset have been classified into land-cover classes.

3. Vegetation parameter retrieval (stem volume retrieval, crop height retrieval etc. as appropriate) for the segments classified as "vegetated". The type of vegetation parameter retrieval depends on the sub-class of the vegetated segment ("boreal forest", "agricultural land" etc.). Parameter retrievals in general can be performed by using those InSAR observations that are most favourable for the retrieval at hand. In boreal forests this would involve using only the InSAR observations with the highest Interferometric Coherence-Contrast (ICC) values (see *Paper D* for details). For boreal forest segments stem volume retrieval can be performed using methods described in *Paper B* and *Paper E*. After this step the segments belonging to certain vegetated land-cover classes (for example the "boreal forest"-class) contain extra information derived via vegetation parameter retrieval.

In Step 3 above the stem volume retrieval method described in *Paper B* requires training data in the form of training forest stands with known stem volumes. Moreover, since environmental conditions are spatially variable, the density of training data sites should be high enough to capture major

differences in weather conditions etc. Such training data network is simply not available in very remote areas, and when available the training data is often neither sufficiently recent nor of good enough quality. This problem could be solved by using a *training-data free* stem volume retrieval method like the one presented in Askne and Santoro 2009, where "open" and "dense forest" areas and their respective coherences are determined from the coherence images themselves. If training-data free methods were developed further, C-band multitemporal InSAR techniques could make wall-to-wall continent-wide land-cover mapping and boreal forest stem volume estimation possible, for example with the future Sentinel-1 constellation.

Research and development into the exploitation of C-band multitemporal InSAR datasets has been seriously hindered by the lack of new datasets in the recent years. Basically, after the ERS-1/2 Tandem missions (1-day temporal baseline) or the ERS-1 & ERS-2 Ice Phases (3-day temporal baseline), all available spaceborne C-band InSAR data has been acquired with a much longer temporal baseline. With Envisat ASAR the temporal baseline was 35 days while RadarSat 1 & 2 provided data with a 24-day temporal baseline. With such long temporal baselines natural vegetated targets unfortunately decorrelate almost completely due to temporal decorrelation. This is why in recent years most developments in InSAR for the retrieval of biogeophysical parameter have occurred over non-vegetated targets/areas that can retain coherence for long periods, like *Persistent Scatterers* (PS), arid regions and land ice (mainly ice sheets).

The ESA C-band Sentinel-1 (S-1) constellation with a 12-day repeat orbit makes 6-day temporal baseline InSAR observations possible when both satellites are in operation. The S-1 constellation will be a game-changer in the sense that regular 12-day InSAR observations become possible over most of the world, with regular 6-day InSAR observations over selected areas. With S-1 data multitemporal InSAR will yet again become a viable technique over natural and vegetated targets. Since S-1 will provide a regular and continuous observation scenario and data-flow, it is perfectly suitable for the techniques discussed in this dissertation, for example opportunistic imaging (waiting for the most suitable conditions) and the use of techniques like temporal averaging to reduce noise. Already the 12-day repeat InSAR observations with one satellite can be expected to make a large improvement in land-cover classification, and the use of 6-day coherence will make further improvements possible. Even though 12-day coherence images can be quite noisy and exhibit low coherence over vegetated targets like forests, one should bear in mind that one can make 30 such InSAR observations in a single year. Temporal averaging and other methods (see section 5.2.2.3) can be used to extract valuable information from the S-1 time-series. Over boreal forests the 12-day InSAR coherence will probably be too low to allow for stem volume retrieval, but observations acquired in the most stable environmental conditions will probably still be useful land-cover classification. It can be speculated that utilizing coherence information from the best S-1 6-day InSAR pairs might be able to provide better stem volume retrieval performance than C-band intensity-

only data, but further studies with actual data are needed to assess this. C-band intensity-only data has been shown to provide useful stem volume retrieval results at 1km – 10km pixel sizes (see section 5.3.4.6 and Santoro et al. 2011). In crop height retrieval even the 6-day repeat InSAR data will probably suffer from too high temporal decorrelation for reliable crop height retrieval, but this is another issue that should be studied further once S-1 data becomes available.

Recommendations for Future Studies

In order to assess and further develop the potential of multitemporal InSAR for land-cover and vegetation mapping, several new lines of study ought to be considered. As discussed above, the future Sentinel-1 constellation offers promise for land-cover and vegetation mapping. It is recommended that the following issues are studied using actual Sentinel-1 data:

- InSAR coherence-statistics over a wide range of land cover classes for 6- and 12-day repeat data. These statistics are needed in order to understand where "opportunistic" InSAR-observations will be feasible.
- InSAR-based land-cover and crop classification with 6- and 12-day repeat data, including classification synergy with optical datasets (from the Sentinel-2 constellation for example). Forest/non-forest classification as well as sparse/dense forest classification should be a key area of study.
- InSAR-based forest stem volume retrieval using 6-day repeat data. The study areas should cover at least boreal and temperate forests and savannas in order to assess where the method will or will not work. In addition, training-data free segmentation-based retrieval methods should be developed.

Bibliography

*Askne, J. and M. Santoro (2005), "Multitemporal repeat pass SAR interferometry of boreal forests." IEEE Transactions on Geoscience and Remote Sensing **43**(6): 1219-1228.*

*Askne, J. and M. Santoro (2007), "Selection of forest stands for stem volume retrieval from stable ERS Tandem InSAR observations." IEEE Geoscience and Remote Sensing Letters **4**(1): 46-50.*

*Askne, J. and M. Santoro (2009), "Automatic model-based estimation of boreal forest stem volume from repeat pass C-band InSAR coherence." IEEE Transactions on Geoscience and Remote Sensing **47**(2): 513-516.*

*Askne, J., M. Santoro, G. Smith and J. E. S. Fransson (2003), "Multitemporal repeat-pass SAR interferometry of boreal forests." IEEE Transactions on Geoscience and Remote Sensing **41**(7): 1540-1550.*

*Askne, J. I. H., P. B. G. Dammert, L. M. H. Ulander and G. Smith (1997), "C-band repeat-pass interferometric SAR observations of the forest." IEEE Transactions on Geoscience and Remote Sensing **35**(1): 25-35.*

*Attema, E. P. W. and F. T. Ulaby (1978), "Vegetation modeled as a water cloud." Radio Science **13**(2): 357-364.*

*Baatz, M. and A. Schäpe (2000), "Multiresolution segmentation: an optimization approach for high quality multi-scale image segmentation." Angewandte geographische informationsverarbeitung **12**(12): 12-23.*

*Bamler, R. and P. Hartl (1998), "Synthetic aperture radar interferometry." Inverse Problems **14**(4): R1-R54.*

*Blaes, X. and P. Defourny (2003), "Retrieving crop parameters based on Tandem ERS 1/2 interferometric coherence images." Remote Sensing of Environment **88**(4): 374-385.*

*Bruzzone, L., M. Marconcini, U. Wegmuller and A. Wiesmann (2004), "An advanced system for the automatic classification of multitemporal SAR images." IEEE Transactions on Geoscience and Remote Sensing **42**(6): 1321-1334.*

*Bush, T. and F. Ulaby (1976), "Radar return from a continuous vegetation canopy." IEEE Transactions on Antennas and Propagation **24**(3): 269-276.*

*Castel, T., J.-M. Martinez, A. Beaudoin, U. Wegmuller and T. Strozzi (2000), "ERS InSAR data for remote sensing hilly forested areas." Remote Sensing of Environment **73**(1): 73-86.*

*Cloude, S. R. and K. P. Papathanassiou (1998), "Polarimetric SAR interferometry." IEEE Transactions on Geoscience and Remote Sensing **36**(5): 1551-1565.*

Colesanti, C., F. De Zan, A. Ferretti, C. Prati and F. Rocca (2003), "Generation of DEM with sub-metric vertical accuracy from 30'ERS-ENVISAT pairs." Proceedings of the FRINGE 2003 Workshop, Frascati, Italy: 1-5.

*Dammert, P. B. G., J. I. H. Askne and S. Kuhlmann (1999), "Unsupervised segmentation of multitemporal interferometric SAR images." IEEE Transactions on Geoscience and Remote Sensing **37**(5): 2259-2271.*

*Dixon, R. K., A. M. Solomon, S. Brown, R. A. Houghton, M. C. Trexier and J. Wisniewski (1994), "Carbon pools and flux of global forest ecosystems." Science **263**(5144): 185-190.*

*Dobson, M. C., F. T. Ulaby, L. E. Pierce, T. L. Sharik, K. M. Bergen, J. Kellndorfer, J. R. Kendra, E. Li, Y. C. Lin, A. Nashashibi, K. Sarabandi and P. Siqueira (1995), "Estimation of forest biophysical characteristics in Northern Michigan with SIR-C/X-SAR." IEEE Transactions on Geoscience and Remote Sensing **33**(4): 877-895.*

*Drezet, P. M. L. and S. Quegan (2006), "Environmental effects on the interferometric repeat-pass coherence of forests." IEEE Transactions on Geoscience and Remote Sensing **44**(4): 825-837.*

Duchossois, G., G. Kohlhammer and P. Martin (1996), "Completion of the ERS Tandem mission." Earth Observation Quarterly(52): 1.

*Dutra, L. V. (1999), "Feature extraction and selection for ERS-1/2 InSAR classification." International Journal of Remote Sensing **20**(5): 993-1016.*

*Engdahl, M. and J. Hyyppä (2000), "Temporal averaging of multitemporal ERS-1/2 Tandem InSAR data." IEEE 2000 International Geoscience and Remote Sensing Symposium (IGARSS'00), Hawaii (USA)**:** 2224-2226.*

*Engdahl, M. E., M. Borgeaud and M. Rast (2001), "The use of ERS-1/2 Tandem interferometric coherence in the estimation of agricultural crop heights." IEEE Transactions on Geoscience and Remote Sensing **39**(8): 1799-1806.*

*Engdahl, M. E. and J. M. Hyyppä (2003), "Land-cover classification using multitemporal ERS-1/2 InSAR data." IEEE Transactions on Geoscience and Remote Sensing **41**(7): 1620-1628.*

*Engdahl, M. E., J. Pulliainen and M. Hallikainen (2008), "Segment-based stem volume retrieval in boreal forests using multitemporal ERS-1/2 InSAR data." Canadian Journal of Remote Sensing **34**(1): 46-55.*

*Engdahl, M. E., J. T. Pulliainen and M. T. Hallikainen (2004), "Boreal forest coherence-based measures of interferometric pair suitability for operational stem volume retrieval." IEEE Geoscience and Remote Sensing Letters **1**(3): 228-231.*

Eriksson, L. E. B., M. Santoro, A. Wiesmann and C. C. Schmullius (2003), "Multitemporal JERS repeat-pass coherence for growing-stock volume

*estimation of Siberian forest." IEEE Transactions on Geoscience and Remote Sensing **41**(7): 1561-1570.*

Ferretti, A., A. Monti-Guarnieri, C. Prati and F. Rocca (2007), "InSAR principles : Guidelines for SAR Interferometry Processing and Interpretation (TM-19)." Noordwijk, The Netherlands, ESA Publications, ESTEC, Postbus 299, 2200 AG Noordwijk, The Netherlands.

*Fransson, J. E. S. (1999), "Estimation of stem volume in boreal forests using ERS-1 C- and JERS-1 L-band SAR data." International Journal of Remote Sensing **20**(1): 123-137.*

*Fransson, J. E. S., G. Smith, J. Askne and H. Olsson (2001), "Stem volume estimation in boreal forests using ERS-1/2 coherence and SPOT XS optical data." International Journal of Remote Sensing **22**(14): 2777-2791.*

*Gatelli, F., A. Monti-Guarnieri, F. Parizzi, P. Pasquali, C. Prati and F. Rocca (1994), "The wavenumber shift in SAR interferometry." IEEE Transactions on Geoscience and Remote Sensing **32**(4): 855-865.*

*Gens, R. and J. L. Van Genderen (1996), "Review article SAR interferometry—issues, techniques, applications." International Journal of Remote Sensing **17**(10): 1803-1835.*

*Graham, L. C. (1974), "Synthetic interferometer radar for topographic mapping." Proceedings of the IEEE **62**(6): 763-768.*

*Grey, W. and A. Luckman (2003), "Mapping urban extent using satellite radar interferometry." Photogrammetric Engineering and Remote Sensing **69**(9): 957-961.*

*Grey, W. M. F., A. J. Luckman and D. Holland (2003), "Mapping urban change in the UK using satellite radar interferometry." Remote Sensing of Environment **87**(1): 16-22.*

*Hagberg, J. O., L. M. H. Ulander and J. Askne (1995), "Repeat-pass SAR interferometry over forested terrain." IEEE Transactions on Geoscience and Remote Sensing **33**(2): 331-340.*

Häme, T., A. Salli and K. Lahti (1992), "Estimation of carbon storage in boreal forests using remote sensing data." The Finnish research programme on climate change, progress report: 250–252.

Henderson, F. M. and A. J. Lewis (1998), "Manual of Remote Sensing; Volume 2: Principles and Applications of Imaging Radar." John Wiley & Sons Inc.

*Houghton, R. A., K. T. Lawrence, J. L. Hackler and S. Brown (2001), "The spatial distribution of forest biomass in the Brazilian Amazon: a comparison of estimates." Global Change Biology **7**(7): 731-746.*

*Hyyppä, H. J. and J. M. Hyyppä (2001), "Effects of stand size on the accuracy of remote sensing-based forest inventory." IEEE Transactions on Geoscience and Remote Sensing **39**(12): 2613-2621.*

Hyyppä, J., H. Hyyppä, M. Inkinen, M. E. Engdahl, S. Linko and Y.-H. Zhu (2000), "Accuracy comparison of various remote sensing data sources

in the retrieval of forest stand attributes." Forest Ecology and Management **128**(1-2): 109-120.

Imhoff, M. L. (1995), "Radar backscatter and biomass saturation: ramifications for global biomass inventory." IEEE Transactions on Geoscience and Remote Sensing **33**(2): 511-518.

Jain, A. K., R. P. W. Duin and J. Mao (2000), "Statistical pattern recognition: A review." IEEE Transactions on pattern analysis and machine intelligence **22**(1): 4-37.

*Jolliffe, I. T. (2005), "*Principal Component Analysis." *John Wiley & Sons, Ltd.*

Joughin, I. R., D. P. Winebrenner and D. B. Percival (1994), "Probability density functions for multilook polarimetric signatures." IEEE Transactions on Geoscience and Remote Sensing **32**(3): 562-574.

Kellndorfer, J., W. Walker, L. Pierce, C. Dobson, J. A. Fites, C. Hunsaker, J. Vona and M. Clutter (2004), "Vegetation height estimation from shuttle radar topography mission and national elevation datasets." Remote Sensing of Environment **93**(3): 339-358.

Koskinen, J. T., J. T. Pulliainen, J. M. Hyyppä, M. E. Engdahl and M. T. Hallikainen (2001), "The seasonal behavior of interferometric coherence in boreal forest." IEEE Transactions on Geoscience and Remote Sensing **39**(4): 820-829.

Koskinen, J. T., J. T. Pulliainen, M. P. Mäkynen and M. T. Hallikainen (1999), "Seasonal comparison of HUTSCAT ranging scatterometer and ERS-1 SAR microwave signatures of boreal forest zone." IEEE Transactions on Geoscience and Remote Sensing **37**(4): 2068-2079.

*Lillesand, T. M., R. W. Kiefer and J. W. Chipman (2007), "*Remote Sensing and Image Interpretation." *John Wiley & Sons, Ltd. .*

Lopez-Sanchez, J. M. and J. D. Ballester-Berman (2009), "Potentials of polarimetric SAR interferometry for agriculture monitoring." Radio Science **44**(2).

Marliani, F., S. Paloscia, P. Pampaloni and J. A. Kong (2002), "Simulating coherent backscattering from crops during the growing cycle." IEEE Transactions on Geoscience and Remote Sensing **40**(1).

Massonnet, D. and K. L. Feigl (1998), "Radar interferometry and its application to changes in the Earth's surface." Reviews of Geophysics **36**(4): 441–500.

Matikainen, L., J. Hyyppä and M. E. Engdahl (2006), "Mapping built-up areas from multitemporal interferometric SAR images: A segment-based approach." Photogrammetric Engineering and Remote Sensing **72**(6): 701-714.

*Oliver, C. and S. Quegan (1998), "*Understanding Synthetic Aperture Radar Images." *Artech House Inc.*

Papathanassiou, K. P. and S. R. Cloude (2001), "Single-baseline polarimetric SAR interferometry." IEEE Transactions on Geoscience and Remote Sensing **39**(11): 2352-2363.

*Perissin, D., C. Prati, M. E. Engdahl and Y. L. Desnos (2006), "Validating the SAR Wavenumber Shift Principle With the ERS-Envisat PS Coherent Combination." IEEE Transactions on Geoscience and Remote Sensing **44**(9): 2343-2351.*

*Pulliainen, J., M. E. Engdahl and M. Hallikainen (2003), "Feasibility of multi-temporal interferometric SAR data for stand-level estimation of boreal forest stem volume." Remote Sensing of Environment **85**(4): 397-409.*

*Pulliainen, J. T., K. Heiska, J. Hyyppä and M. T. Hallikainen (1994), "Backscattering properties of boreal forests at the C- and X-bands." IEEE Transactions on Geoscience and Remote Sensing **32**(5): 1041-1050.*

*Pulliainen, J. T., L. Kurvonen and M. T. Hallikainen (1999), "Multitemporal behavior of L- and C-band SAR observations of boreal forests." IEEE Transactions on Geoscience and Remote Sensing **37**(2): 927-937.*

*Pulliainen, J. T., P. J. Mikkelä, M. T. Hallikainen and J. P. Ikonen (1996), "Seasonal dynamics of C-band backscatter of boreal forests with applications to biomass and soil moisture estimation." IEEE Transactions on Geoscience and Remote Sensing **34**(3): 758-770.*

*Quegan, S. and Y. Jiong Jiong (2001), "Filtering of multichannel SAR images." IEEE Transactions on Geoscience and Remote Sensing **39**(11): 2373-2379.*

*Quegan, S., T. Le Toan, J. J. Yu, F. Ribbes and N. Floury (2000), "Multitemporal ERS SAR analysis applied to forest mapping." IEEE Transactions on Geoscience and Remote Sensing **38**(2): 741-753.*

Raney, R. K., T. Freeman, R. W. Hawkins and R. Bamler (1994), "A plea for radar brightness." IEEE 1994 International Geoscience and Remote Sensing Symposium (IGARSS'94), Pasadena (USA).

*Rauste, Y., T. Hame, J. Pulliainen, K. Heiska and M. Hallikainen (1994), "Radar-based forest biomass estimation." International Journal of Remote Sensing **15**(14): 2797-2808.*

*Rignot, E. J. M. and J. J. Van Zyl (1993), "Change detection techniques for ERS-1 SAR data." IEEE Transactions on Geoscience and Remote Sensing **31**(4): 896-906.*

*Rodriguez, E. and J. M. Martin (1992), "Theory and design of interferometric synthetic aperture radars." IEE Proceedings F **139**(2): 147-159.*

S. Ward, S. S. (2008), "The Earth Observation Handbook - Climate Change Special Edition 2008 [ESA SP-115]." ESA Communication Production Office, ESTEC, Postbus 299, 2200 AG Noordwijk, The Netherlands.

*Saich, P. and M. Borgeaud (2000), "Interpreting ERS SAR signatures of agricultural crops in Flevoland, 1993–1996." IEEE Transactions on Geoscience and Remote Sensing **38**(2): 651.*

*Santoro, M., J. Askne and P. B. G. Dammert (2005), "Tree height influence on ERS interferometric phase in boreal forest." IEEE Transactions on Geoscience and Remote Sensing **43**(2): 207-217.*

*Santoro, M., J. Askne, G. Smith and J. E. S. Fransson (2002), "Stem volume retrieval in boreal forests from ERS-1/2 interferometry." Remote Sensing of Environment **81**(1): 19-35.*

*Santoro, M., J. I. H. Askne, U. Wegmuller and C. L. Werner (2007), "Observations, modeling, and applications of ERS-ENVISAT coherence over land surfaces." IEEE Transactions on Geoscience and Remote Sensing **45**(8): 2600-2611.*

*Santoro, M., C. Beer, O. Cartus, C. Schmullius, A. Shvidenko, I. McCallum, U. Wegmüller and A. Wiesmann (2011), "Retrieval of growing stock volume in boreal forest using hyper-temporal series of Envisat ASAR ScanSAR backscatter measurements." Remote Sensing of Environment **115**(2): 490-507.*

*Scipal, K., M. Arcioni, J. Chave, J. Dall, F. Fois, T. LeToan, C. Lin, K. Papathanassiou, S. Quegan, F. Rocca, S. Saatchi, H. Shugart, L. Ulander and M. Williams (2010), "The BIOMASS mission; An ESA Earth Explorer candidate to measure the BIOMASS of the Earth's forests." 2010 IEEE International Geoscience and Remote Sensing Symposium (IGARSS'10), , Hawaii (USA)**:** 52-55.*

*Srivastava, H. S., P. Patel and R. R. Navalgund (2006), "Application potentials of synthetic aperture radar interferometry for land-cover mapping and crop-height estimation." Current science **91**(6): 783.*

*Strozzi, T., P. B. G. Dammert, U. Wegmuller, J. M. Martinez, J. I. H. Askne, A. Beaudoin and N. T. Hallikainen (2000), "Landuse mapping with ERS SAR interferometry." IEEE Transactions on Geoscience and Remote Sensing **38**(2): 766-775.*

*Tansey, K. J., A. J. Luckman, L. Skinner, H. Balzter, T. Strozzi and W. Wagner (2004), "Classification of forest volume resources using ERS Tandem coherence and JERS backscatter data." International Journal of Remote Sensing **25**(4): 751-768.*

Tou, J. T. and R. C. Gonzalez (1974), "Pattern Recognition Principles." Addison-Wesley Publishing Co.

*Touzi, R. (2002), "A review of speckle filtering in the context of estimation theory." IEEE Transactions on Geoscience and Remote Sensing **40**(11): 2392-2404.*

*Touzi, R. and A. Lopes (1996), "Statistics of the Stokes parameters and of the complex coherence parameters in one-look and multilook speckle fields." IEEE Transactions on Geoscience and Remote Sensing **34**(2): 519-531.*

*Touzi, R., A. Lopes, J. Bruniquel and P. W. Vachon (1999), "Coherence estimation for SAR imagery." IEEE Transactions on Geoscience and Remote Sensing **37**(1): 135-149.*

*Treuhaft, R. N. and S. R. Cloude (1999), "The structure of oriented vegetation from polarimetric interferometry." IEEE Transactions on Geoscience and Remote Sensing **37**(5): 2620-2624.*

*Treuhaft, R. N., S. N. Madsen, M. Moghaddam and J. J. van Zyl (1996), "Vegetation characteristics and underlying topography from interferometric radar." Radio Science **31**(6): 1449-1485.*

*Treuhaft, R. N. and P. R. Siqueira (2000), "Vertical structure of vegetated land surfaces from interferometric and polarimetric radar." Radio Science **35**(1): 141-177.*

*Ulaby, F. (1975), "Radar response to vegetation." IEEE Transactions on Antennas and Propagation **23**(1): 36-45.*

Ulaby, F. T. and M. C. Dobson (1989), "Handbook of Radar Scattering Statistics for Terrain.", Artech House, 685 Canton Street, Norwood, MA 02062 (USA).

*Ulaby, F. T., K. Sarabandi, K. McDonald, M. Whitt and M. C. Dobson (1990), "Michigan microwave canopy scattering model." International Journal of Remote Sensing **11**(7): 1223-1253.*

*Wagner, W., A. Luckman, J. Vietmeier, K. Tansey, H. Balzter, C. Schmullius, M. Davidson, D. Gaveau, M. Gluck and T. Le Toan (2003), "Large-scale mapping of boreal forest in SIBERIA using ERS Tandem coherence and JERS backscatter data." Remote Sensing of Environment **85**(2): 125-144.*

*Walker, W. S., J. M. Kellndorfer, E. LaPoint, M. Hoppus and J. Westfall (2007), "An empirical InSAR-optical fusion approach to mapping vegetation canopy height." Remote Sensing of Environment **109**(4): 482-499.*

*Wegmüller, U. and C. Werner (1997), "Retrieval of vegetation parameters with SAR interferometry." IEEE Transactions onGeoscience and Remote Sensing **35**(1): 18-24.*

*Wegmüller, U. and C. L. Werner (1995), "SAR interferometric signatures of forest." IEEE Transactions on Geoscience and Remote Sensing **33**(5): 1153-1161.*

*Weydahl, D. J. (2001), "Analysis of ERS SAR coherence images over vegetated areas and urban features." International Journal of Remote Sensing **22**(14): 2811-2830.*

*Zebker, H. A. and J. Villasenor (1992), "Decorrelation in interferometric radar echoes." IEEE Transactions on Geoscience and Remote Sensing **30**(5): 950-959.*

Aalto-DD 178/2013

ISBN 978-952-60-5415-5
ISBN 978-952-60-5416-2 (pdf)
ISSN-L 1799-4934
ISSN 1799-4934
ISSN 1799-4942 (pdf)

Aalto University
School of Electrical Engineering
Department of Radio Science and Engineering
www.aalto.fi

BUSINESS + ECONOMY

ART + DESIGN + ARCHITECTURE

SCIENCE + TECHNOLOGY

CROSSOVER

DOCTORAL DISSERTATIONS